Construction and performance of a neutrino detector for neutrino-nucleus interaction cross-section measurements (ニュートリノ-原子核反応断面積測定のためのニュートリノ検出器の構成と性能)

Riku Tamura
Department of Physics, University of Tokyo

January 30, 2018

Abstract

In order to reduce the systematic errors due to cross section in T2K neutrino oscillation measurement, we have been conducting WAGASCI experiment at J-PARC. Its main goals are measurements of cross-section ratio of water to hydrocarbon and cross section of water and hydrocarbon with large acceptance.

The performance of eighty four 32-channel arrayed MPPCs and 1,400 single-channel MPPCs corresponding to 4,088 channels in total are characterized. Gain, breakdown voltage, crosstalk probability, and relative photo detection efficiency are measured for all the channels. The readout electronics based on SPIROC2D has been developed. This experiment is first application of SPIROC2D. It is confirmed that SPIROC2D has sufficient performance for operation and readout of an arrayed MPPC. Also, operation of all 1280 channels is tested and we succeed to readout MPPC signal of all channels.

We started the construction of the detector in October 2016 and finished it in August 2017. The number of dead channels is three and the other 1,277 channels work stably. Because muon range detectors are under construction or transportation, we started experiment with other existing alternative modules. The installation of the detectors finished in August 2017 and we started the detector operation with temporary setup in the beginning of September. The performance of the detector is tested with cosmic ray, and it is confirmed that the detector works stably. The reconstruction algorithm has been developed and we succeed to observe cosmic ray. It is confirmed the detector has sufficient performance for observation of charged particles.

The neutrino beam measurement started on October 15th, 2017. The data has been collected with the neutrino beam from October 15th, 2017, to October 22nd, 2017, and with the anti-neutrino beam from October 22nd, 2017, to December 22nd, 2017. The data acquisition went on stably and we succeed to accumulate 2.0×10^{19} POT in neutrino mode and 3.6×10^{20} POT in anti-neutrino mode. The stability of detector during the neutrino data taking is confirmed using the dark noise and cosmic ray. The event rate of the wall background is confirmed to be stable. The event selection method is established and we succeed to observe neutrino candidates.

Contents

Chapter 1

Introduction

Neutrino is one of the neutral elementary particles with spin 1/2, and interacts only through the weak interaction. After the discovery of the neutrino, the strenuous effort of scientists makes the mystery of neutrino clear, but there still remain many questions in neutrino, such as the CP violation in leptonic sector, the mass of neutrinos, the existence of sterile neutrino, a majorana neutrino and so on. As an introduction of this thesis, the theory of neutrino oscillation and the interaction between neutrino and nucleus, that plays an important role for precise measurements of neutrino oscillation parameters, are explained. Then current status of neutrino oscillation experiments mainly related to the T2K experiment and the T2K experiment itself are introduced.

1.1 Neutrino oscillation

Neutrino is one of the neutral elementary particles with spin 1/2, and interacts only though the weak interaction. There are three types of neutrinos : electro neutrino(ν_e), mu neutrino(ν_μ), tau neutrino(ν_τ) and their anti-particles.

The standard model of elementary particle physics, which has demonstrated huge successes in providing experimental predictions at present, assumed the masses of neutrinos were exactly zero and lepton flavor was conserved. However, the discovery of neutrino oscillation in the atmospheric neutrino by Super-Kamiokande[1] changed the situation because the existence of neutrino oscillation requires the massive neutrino.

The neutrino flavor eigenstates, $|\nu_\alpha\rangle$ $(\alpha = e, \mu, \tau)$, are described as the superpositions of the neutrino mass eigenstates, $|\nu_i\rangle$ $(\alpha = 1, 2, 3)$. The mixing of flavor eigenstates and mass eigenstates is given by an unitary matrix called the Pontecorvo-Maki-Nakagawa-Sakata(PMNS) matrix[2], U:

$$|\nu_\alpha\rangle = \sum_i U_{\alpha i} |\nu_i\rangle \tag{1.1}$$

The PMNS matrix is given as follows:

$$U = \begin{pmatrix} 1 & 0 & 0 \\ 0 & c_{23} & s_{23} \\ 0 & -s_{23} & c_{23} \end{pmatrix} \begin{pmatrix} c_{13} & 0 & s_{13}e^{-i\delta_{CP}} \\ 0 & 1 & 0 \\ -s_{13}e^{i\delta_{CP}} & 0 & c_{13} \end{pmatrix} \begin{pmatrix} c_{12} & s_{12} & 0 \\ -s_{12} & c_{12} & 0 \\ 0 & 0 & 1 \end{pmatrix}, \tag{1.2}$$

where $c_{ij} = cos\theta_{ij}$, $s_{ij} = sin\theta_{ij}$. θ_{ij} is mixing angle and δ_{CP} is the CP-violation phase. The probability of the neutrino oscillation from ν_α to ν_β after traveling distance L with the energy E is given as follows:

$$P(\nu_\alpha \to \nu_\beta) = \delta_{\alpha\beta} \quad - \quad 4\sum_{i>j} Re(U^*_{\alpha i}U_{\beta i}U_{\alpha j}U^*_{\beta j}) \sin^2\left(\frac{\Delta m^2_{ij}L}{4E}\right)$$

$$- \quad 2\sum_{i>j} Im(U^*_{\alpha i}U_{\beta i}U_{\alpha j}U^*_{\beta j})\sin\left(\frac{\Delta m^2_{ij}L}{2E}\right), \tag{1.3}$$

where $\Delta m^2_{ij} = m^2_i - m^2_j$. The existence of neutrino oscillation is the evidence of non-zero Δm^2_{ij} and mixing angle θ_{ij}. Especially, the equation for electron neutrino appearance from muon neutrino $P(\nu_\mu \to \nu_e)$ is given as following:

$$P(\nu_\mu \to \nu_e) = P1 + P2 + P3 + P4 \tag{1.4}$$

$$\begin{aligned} P1 &= \sin^2(\theta_{23})\sin^2(2\theta_{13})\sin^2(\Delta m^2_{32}L/4E) \\ P2 &= \cos^2(\theta_{23})\sin^2(2\theta_{13})\sin^2(\Delta m^2_{21}L/4E) \\ P3 &= \mp J\sin^2(\Delta m^2_{32}L/4E)\sin(\Delta m^2_{21}L/4E) \\ P4 &= J\cot(\delta_{CP})\sin(\Delta m^2_{32}L/4E)\cos(\Delta m^2_{32}L/4E)\sin(\Delta m^2_{21}L/4E), \end{aligned}$$

where

$$J = \cos(\theta_{13})\sin(2\theta_{12})\sin(2\theta_{13})\sin(2\theta_{23})\sin(\delta_{CP}) \tag{1.5}$$

and the sign in P3 is negative for neutrino and positive for anti-neutrino. CP violation term can be measured comparing electron neutrino appearance probabilities between neutrino and anti-neutrino as following:

$$\begin{aligned} P(\nu_\mu \to \nu_e) - P(\bar{\nu}_\mu \to \bar{\nu}_e) &= -2\sin(\delta_{CP})\cos(\theta_{13})\sin(2\theta_{12})\sin(2\theta_{13})\sin(2\theta_{23}) \times \\ &\quad \sin^2(\Delta m^2_{32}L/4E)\sin(\Delta m^2_{21}L/4E) \end{aligned} \tag{1.6}$$

The measurement of CP violation phase is one of the most important measurements for long-baseline accelerator experiment.

1.2 Neutrino-Nucleus Interaction

Comprehension of neutrino-nucleus interaction is essential for neutrino oscillation analysis as the reconstruction of initial neutrino energy and the selection of the signal event and the background event are based on neutrino-nucleus interaction. Neutrino-nucleus interaction mainly consists of two parts. First is the interaction of a neutrino with a nucleon through charged current (CC) mediated by $W^\pm$ boson or through neutral current (NC) mediated by Z boson producing secondary particles. Second is the interaction of secondary particles with the nucleons in nucleus.

Figure 1.1 shows the cross section in sub-GeV range. Charged current interaction is classified into several types[3].

- CC quasi-elastic
  Charged current quasi elastic scattering(CCQE) is the dominant neutrino interaction for neutrino energy less than about 1GeV. CCQE is the process, $\nu_l + n \to l + p(\bar{\nu}_l + p \to l + n)$, where $l = e, \mu, \tau$ and a single charged lepton and a nucleon are produced in the elastic interaction of a neutrino (anti-neutrino) with a nucleon in the target material. This process is two-body scattering and the neutrino energy can be reconstructed from the kinematics of both of the outgoing charged lepton and the nucleon. Also neutrino energy can be reconstructed from the outgoing charged lepton kinematics alone when the direction of initial neutrino is known.

- CC1π
  CC1π is the second dominant neutrino interaction for neutrino energy less than about 1GeV.

CC1π is the process, $\nu_l + N \rightarrow l + N' + \pi$, where an inelastic scattering produces a nucleon excited state, mainly Δ, and such a baryonic resonance quickly decays to a nucleon and single-pion. This process is three-body scattering and the energy of scattered particles is likely to be lower than that produced in the CCQE process. If the pion or a nucleon fail to be reconstructed, this process can be main background.

- CC DIS
  CC DIS is the dominant interaction for high energy neutrino. CC DIS is the process,$\nu_l + N \rightarrow l + N' + hadrons$, where the process can approximate the scattering of a neutrino with a quark. The cross section is small for neutrino energy less than about 1GeV.

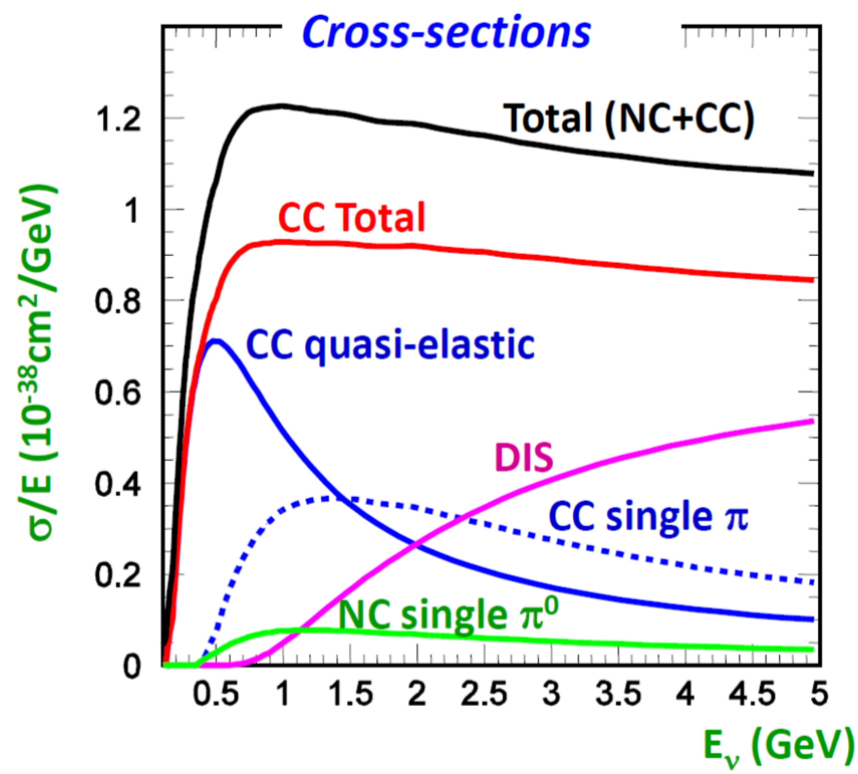

Figure 1.1: The cross section of neutrino interaction in sub-GeV range[4].

The neutrino-nucleus interaction also depends on the kind of the target nucleus because the binding energy of the nucleon in nucleus affects the kinematics of secondary particles and initial nucleon kinematics. It is highly dependent on the nucleon kinematics model and the relativistic fermi gas mode(RFG), which is the assumption that all nucleons are in a potential and all states are filled up to a Fermi-level and has a high momentum tail, is the principal model of current leading long-baseline experiment, T2K[5].

The interaction of secondary particles with nucleons in nucleus depends on the kind of nucleus and secondary particle kinematics. The outgoing charged lepton is almost not affected. However secondary hadrons such as pion and nucleon are strongly affected and there is a possibility that hadrons are trapped in nucleus and the kinematic is affected.

Current neutrino experiments use the nucleus which has multi nucleons such as carbon and oxygen as the target nucleus and neutrino-nucleus interaction plays an important role in the neutrino oscillation analysis. Hence, the cross-section measurement is important for precise neutrino oscillation measurements.

1.3 Current status of neutrino oscillation measurement

Current status of neutrino oscillation parameter is shown in Table 1.1[6]. The result is obtained by analyzing the solar neutrino data, long baseline accelerator experiment data, reactor neutrino data and atmospheric neutrino data.

Table 1.1: The best-fit values and and 3σ allowed ranges of the 3-neutrino oscillation parameters, derived from a global fit of the current neutrino oscillation data(from[7]). For the CP violation phase δ the best fit value and the 1σ allowed range is given. The values (values in brackets) correspond to $m_1 < m_2 < m_3$ ($m_3 < m_1 < m_2$).

Parameter	best-fit	3σ range
$\Delta m^2_{21}[10^{-5}\mathrm{eV}^2]$	7.50	7.03-8.09
$\Delta m^2_{31(32)}[10^{-3}\mathrm{eV}^2]$	2.524(2.514)	2.407-2.643(2.399-2.635)
$\sin^2\theta_{12}$	0.306	0.271-0.345
$\sin^2\theta_{23}$	0.441(0.587)	0.385-0.635(0.393-0.640)
$\sin^2\theta_{13}$	0.02166(0.02179)	0.01934-0.02392(0.01953-0.02408)
δ/π	1.45(1.53)	1.12-1.73(1.28-1.76)

1.4 T2K experiment

T2K experiment is a long-baseline neutrino oscillation experiment. It has started in 2009[8]. The $\nu_\mu(\bar{\nu}_\mu)$ beam produced by the J-PARC in Tokai travels 295km through near detectors, ND280, and is detected by far detector, Super-Kamiokande in Kamioka as shown in Fig. 1.2. T2K's main goal is the high precision measurement of neutrino oscillation parameter θ_{23}, θ_{13}, and Δm_{23} through $\nu_\mu(\bar{\nu}_\mu)$ disappearance and $\nu_e(\bar{\nu}_e)$ appearance. T2K reported the first measurement of a non-zero θ_{13} mixing angle and the most precise measurement of θ_{23}. T2K also published first measurement of CP phase δ_{CP} and CP conservation hypothesis is excluded at 90% C.L.[5]. Cross-section measurements of various interaction channels are also published.

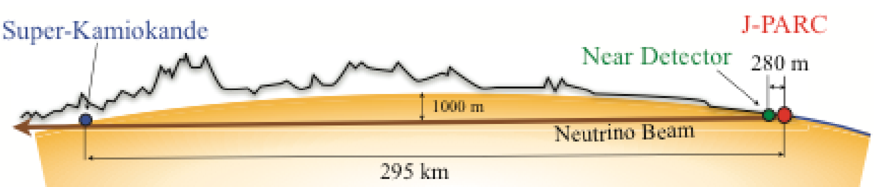

Figure 1.2: A overview of T2K experiment.

1.4.1 J-PARC neutrino beam

J-PARC proton accelerator consists of three accelerators[9], a linear accelerator(LINAC), a rapid-cycling synchrotron(RCS) and a main ring synchrotron(MR). The proton beam injected into the MR is accelerated up to 30GeV. The proton beam spill consists of eight bunches and extracted to T2K neutrino beam line. The extracted proton beam impinges on a graphite target to produce secondary pions, which are focused by magnetic horns. The produced pion enters the decay volume and decays mainly into a muon and a muon neutrino. The produced muon enters beam dump. The muon monitor is located just behind the beam dump and measures the profile of muon.

T2K adopts off-axis method to optimize neutrino energy spectrum to maximize the neutrino oscillation probability. The produced neutrino beam is aimed 2.5° away from the target to the far detector axis. This configuration produces a narrow energy band beam by the kinematics of pion decay. Figure 1.4 shows the oscillation probability at SK and the neutrino energy spectrum. The angle is set so that the spectrum has a peak at the first oscillation maximum, around 600MeV.

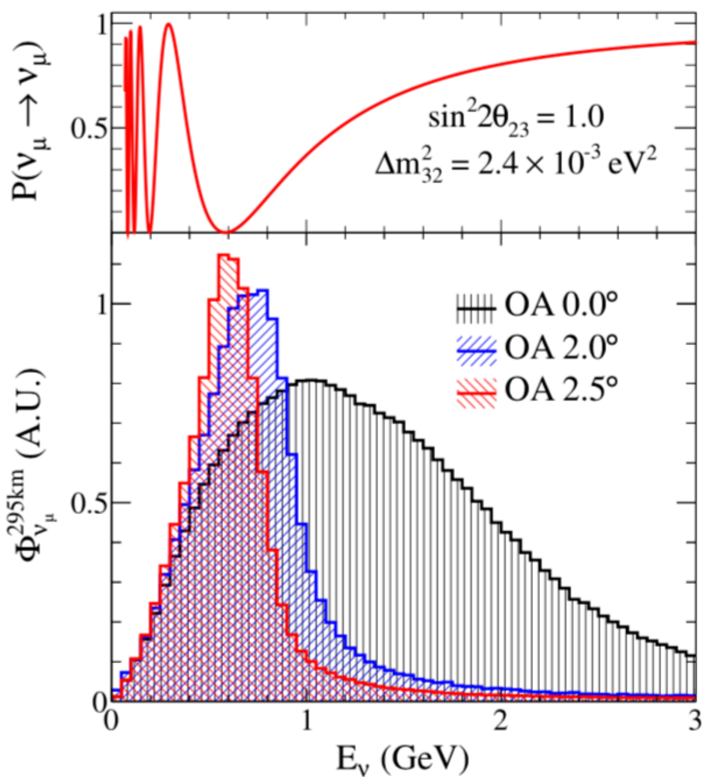

Figure 1.3: The oscillation probability (top) and neutrino energy spectrum(bottom)[10].

1.4.2 Near detectors

T2K adopts two near detectors, on-axis and off-axis detectors. Both on-axis and off-axis detectors are placed at 280m downstream from the neutrino beam target as shown in Fig. 1.4. Figure 1.5 shows the view of two T2K near detectors.

The on-axis near detector, INGRID, measures the direction, profile and event rate of neutrino beam. The center position of INGRID is set at the center of neutrino beam. The on-axis detector provides constraints on the beam direction with the precision better than 10cm, which corresponds 0.4 mrad precision at 280m downstream from neutrino beam target. INGRID consists of 14 identical modules arranged as a cross of two identical groups along the horizontal and vertical direction. A module is composed of a sandwich structure of 11 tracking planes and 9 iron plates.

The off-axis detector, ND280, measures the event rate of neutrino beam. The off-axis detector is placed on the same angle as SK and provides constraints on the neutrino beam flux and cross section. ND280 consists of the magnet and several detectors inside the magnet. The two fine-grain detectors(FGDs) consisting of tracking planes of scintillator bars are the active targets and are sandwiched by three time projection chambers(TPCs). ND280 measures the charged current interaction in FGDs. The acceptance is restricted to forward scattering because of its geometrical structure.

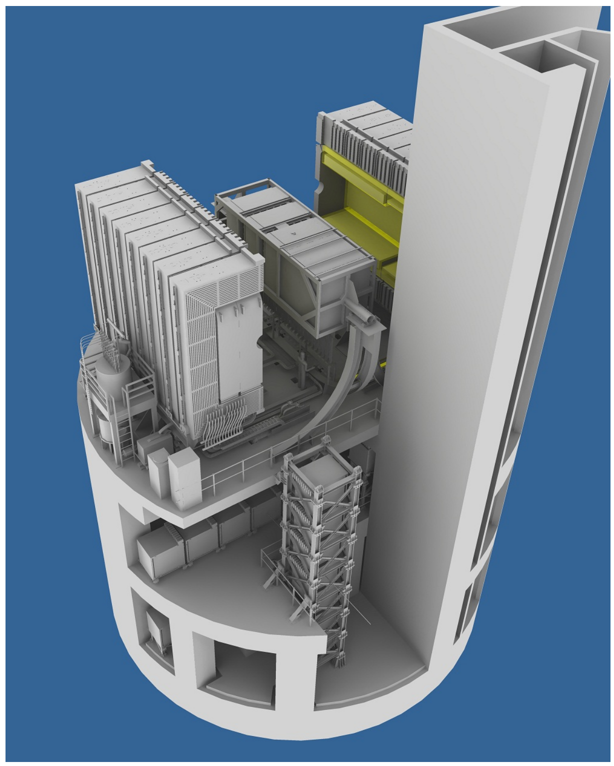

Figure 1.4: Schematic of T2K near detectors.

1.4.3 Far detector

The far detector, Super-Kamiokande[11], measures the energy and event rate of $\nu_e(\bar{\nu}_e)$ appearance and the $\nu_\mu(\bar{\nu}_\mu)$ disappearance by detecting Cherenkov light emitted by a charged lepton produced in neutrino interaction in water. SK consists of stainless tank, sized 39m diameter and 42m tall, and 5,000 tons pure water and a large number of photomultiplier tubes(PMTs) which cover inside inner tank as shown in Fig. 1.6. The acceptance is 4π.

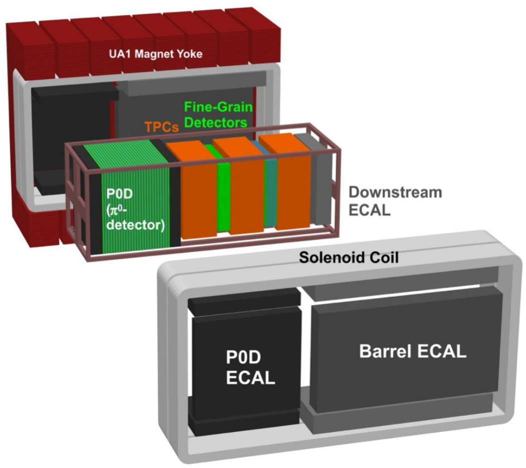

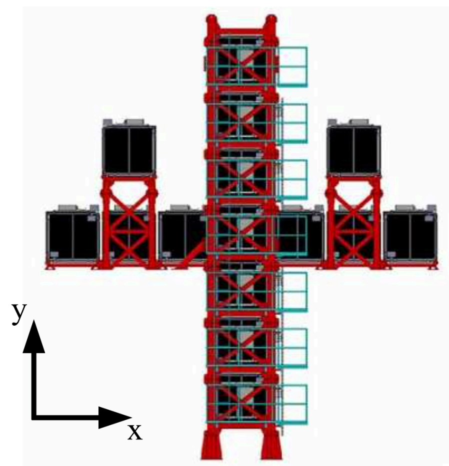

Figure 1.5: The view of near detectors, off-axis detector(ND280) (left) and on-axis detector(INGRID) (right).

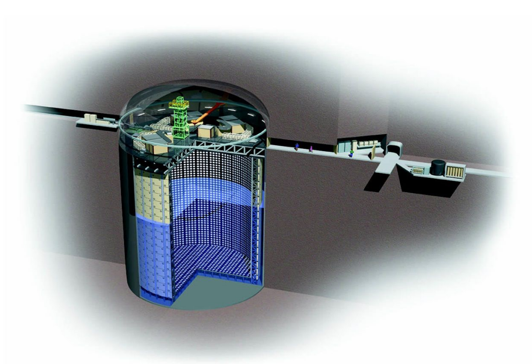
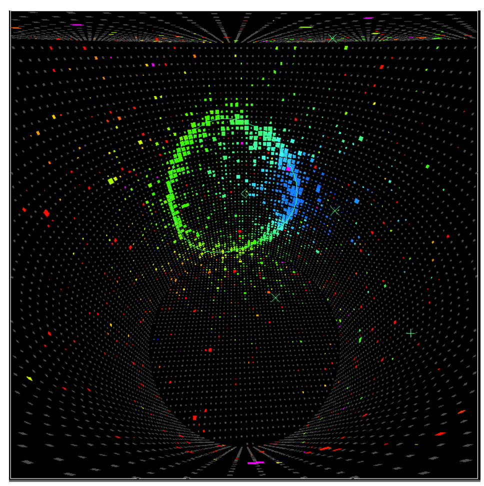

Figure 1.6: The view of far detectors, Super-Kamiokande (left) and Cherenkov ring image of electron event(right).

1.4.4 Current status of oscillation analysis

T2K experiment reports the four neutrino oscillation parameters, $|\Delta m^2_{32}|, \sin^2\theta_{23}, \sin^2\theta_{13}$ and δ_{CP}, through combined analysis of neutrino and anti-neutrino oscillations in appearance and disappearance as shown in Table.1.2[5]. The ν-mode analysis includes not only CCQE-like samples but also CC1π^+ samples.

Table 1.2: The best-fit result and and one σ allowed ranges of the four neutrino oscillation parameters, $|\Delta m^2_{32}|, \sin^2\theta_{23}, \sin^2\theta_{13}$ and δ_{CP} derived from T2K data fit with the reactor constraint including both neutrino mass ordering[5].

Parameter	best-fit	$\pm 1\sigma$ range
δ_{CP}/π	1.430	1.220-1.720
$\sin^2\theta_{13}$	0.0219	0.0208-0.0233
$\sin^2\theta_{23}$	0.534	0.490-0.580
$|\Delta m^2_{32}|[10^{-3}\mathrm{eV}^2]$	2.539	2.952-3.000 ($m_1 < m_2 < m_3$)
		2.424-2.664 ($m_3 < m_1 < m_2$)

The effect of 1σ variation of the systematic uncertainties on the predicted event rate of the ν and $\bar{\nu}$ mode samples is shown in Table 1.3. Except ν_e CC1π^+ channel, the uncertainty due to cross section is the largest component of systematic uncertainty. Final state interaction(FSI), secondary interaction(SI) and photo-nuclear(PN) effect is the largest in case of ν_e CC1π^+ channel. In order to reduce systematic uncertainty, the deeper comprehension of neutrino-nucleus interaction through cross-section measurement, especially on water, is important.

Table 1.3: The effect of 1σ variation of the systematic uncertainties on the predicted event rate of the ν and $\bar{\nu}$ mode samples.

	ν_e CCQE-like	ν_μ	ν_e CC1π^+	$\bar{\nu}_e$ CCQE-like	$\bar{\nu}_\mu$
Source of uncertainty	$\delta N/N$	$\delta N/N$	$\delta N/N$	$\delta N/N$	$\delta N/N$
Flux	3.7%	3.6%	3.6 %	3.8%	3.8%
(w/ ND280 constraint)					
Cross section	5.1%	4.0%	4.9 %	5.5%	4.2%
(w/ ND280 constraint)					
Flux+ cross section	4.2%	2.9%	5.0%	4.7%	3.5%
(w/ ND280 constraint)					
FSI+ SI + PN at cross section at SK	2.5%	1.5%	10.5%	3.0%	2.1%
SK detector	2.4%	3.9%	9.3%	2.5%	3.4%
All	5.5%	5.1%	14.8%	6.5%	5.3%
(w/ ND280 constraint)					

1.5 Current status of cross-section measurement

The charged-current cross section has been measured over many decades. Table 1.4 shows the list of beam properties, nuclear targets, and durations for modern accelerator-based neutrino experiments studying neutrino scattering[6]. Many experiments like SciBooNE, MiniBooNE, K2K and T2K measure CC cross-section measurements on hydrocarbon in the sub-GeV range, but there is a few measurements on water. K2K reports the measurement of ratio of ν_μCC1π cross section to ν_μCC-inclusive cross section[12]. T2K reports first measurements of CC1π cross section[13] in 2017 and that of CC0π cross section[14] in 2018. There is no measurement of CC-inclusive cross section on water in the sub-GeV range. Here, the measurements in T2K are described.

In the measurement of CC1π cross section on water in T2K, double differential cross section as a function of muon momentum and angle are measured. Flux-integrated total cross section are also measured. The cross section is evaluated in the restricted phase-space defined by $p_\mu > 200$ MeV/c, $p_\pi > 200$ MeV/c, $\cos(\theta_\mu) > 0.3$ and $\cos(\theta_\pi) > 0.3$ in order to increase signal efficiency, where $\theta_i (i = \mu, \pi)$ is defined as the angle of the scattering particle to off-axis beam direction. It reports flux-integrated CC1π cross section $\langle\sigma\rangle$=4.25±0.48(stat)±1.56(syst)×10^{-40} cm2/nucleon. There is 36% systematic uncertainty. The dominant systematic uncertainties are those related to cross-section model and flux parameters because of the low purity of the selected signal sample. It evaluates neutrino interaction model by comparing two event generators, NEUT[15] and GENIE[16]. They use essentially the same model for the neutrino interactions simulation, but they differ in the implementation and value of some of the parameters. There is large systematic uncertainty, but the results are in good agreement with the NEUT generator and a general suppression is seen compared to the GENIE generator. It indicates the neutrino-nucleus interaction model dependence of cross section.

In the measurement of CC0π cross section on water in T2K, double differential cross section as a function of muon momentum and angle and flux-integrated total cross section are measured. The phase space is not restricted, but the result has large uncertainty in the angular regions of $\cos(\theta_\mu) < 0.6$ due to the low statistics. In the paper, a comparison of CC0π double-differential cross section result on water to that on carbon[17] shows good agreement with the exception of a few low momentum in the high angle region. There is large uncertainty, but it also indicates the neutrino-nucleus interaction model dependence of cross section. It reports flux-integrated CC0π cross section $\langle\sigma\rangle$=9.5±1.0(stat)±0.9(syst)×10^{-39}cm^2/nucleon. The result is significantly higher than the NEUT(GENIE) prediction of 6.6(6.8) ×10^{-39}cm^2/nucleon primarily due to the disagreement between data and MC in the high-angle regions.

The phase space of both of measurements is restricted or enhanced to forward. It is due to the detector geometry. Figure 1.7 shows the selection efficiency as a function of the muon momentum and as a function of the muon angle for the measurement of CC-inclusive cross section on carbon in T2K[18]. The detector geometry is not same but similar as water target module of T2K near detector. The selection efficiency of water targets in high-angle region is worse than that of hydrocarbon module.

The results of both of above measurements on water are in good agreement with the MC prediction of CC-exclusive cross section in sub-GeV range in the low-angle ranges. However, they have a weakness of the measurement in high-angle region, where the disagreement between data and MC is large. Measurements of exclusive cross sections are complicated by the interaction of secondary particles with nucleus. For example, the pion from a CC single-pion interaction might be absorbed in the nucleus, so the observable final state is similar to that from a CCQE channel. The CC-inclusive channel is much less sensitive to these effects, since it only requires the detection of a charged lepton from the interaction. A precise measurement of CC-inclusive cross section with large phase space, combined with exclusive measurements, will help improve our understanding of neutrino interactions in sub-GeV region.

1.6 Topic of this thesis

In order to reduce systematic errors due to cross section in T2K experiment, we have been conducting a new experiment, named water grid and scintillator detector(WAGASCI) experiment for the measure-

Table 1.4: List of beam properties, nuclear targets, and durations for modern accelerator-based neutrino experiments studying neutrino scattering[6].

Experiment	beam	$\langle E_\nu \rangle$, $\langle E_{\bar{\nu}} \rangle$ [GeV]	targets
ArgoNeuT	$\nu, \bar{\nu}$	4.3, 3.6	Ar
ICARUS (at CNGS)	ν	20.0	Ar
K2K	ν	1.3	CH, H_2O
MicroBooNE	ν	0.8	Ar
MINERvA	$\nu, \bar{\nu}$	3.5(LE), 5.5(ME)	He, C, CH, H_2O, Fe, Pb
MiniBooNE	$\nu, \bar{\nu}$	0.8, 0.7	CH_2
MINOS	$\nu, \bar{\nu}$	3.5, 6.1	Fe
NOMAD	$\nu, \bar{\nu}$	23.4, 19.7	C-based
NOvA	$\nu, \bar{\nu}$	2.0, 2.0	CH_2
SciBooNE	$\nu, \bar{\nu}$	0.8, 0.7	CH
T2K	$\nu, \bar{\nu}$	0.6, 0.6	CF, H_2O, Fe

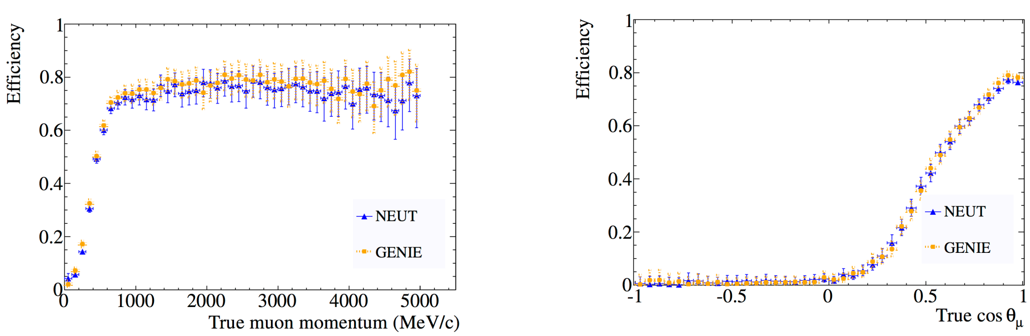

Figure 1.7: The event selection efficiency as a function of the muon momentum(left) and as a function of the muon angle(right) with its statistical error bars[18].

ment of the charged current neutrino cross section in water and hydro-carbon[19]. We will measure the differential cross section for the charged-current interaction on water and hydrocarbon. The detectors is designed to achieve it efficiently. Firstly, the water-hydrocarbon mass ratio of the target module is as high as 4:1 and the high purity measurement of the cross section on H_2O is possible. Secondary, the water target detector adopts three-dimensional grid structure to increase the efficiency of scattering particles to high angle. Figure **??** shows the reconstruction efficiency of water target module. The muon scattering in high angle can be reconstructed efficiently. Figure 1.9 shows the expected angle distribution of muon-like particle.

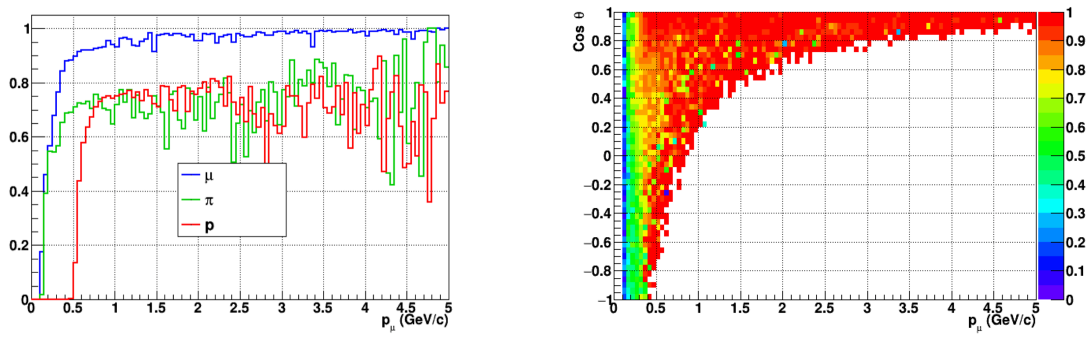

Figure 1.8: The reconstruction efficiency of water target module for secondary particles as a function of the momentum(left) and that for muon as functions of the momentum and angle(right).

Our first goal is to measure the flux-integrated CC-inclusive cross section on water with large phase space. In addition, we plan to measure the exclusive channels such as CC0π, CC1π, CCothers samples. It is expected to constrain the neutrino cross section with water and cross-section ratio between water and hydrocarbon.

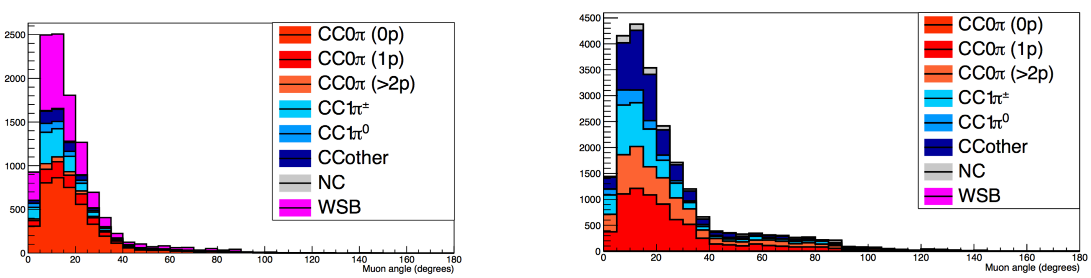

Figure 1.9: The reconstructed angles of the longest tracks in the selected events in the neutrino mode(left) and anti-neutrino mode(right).

In this thesis, the construction and performance of the water target detector, called Water Module, are described. Water Module consists of water and three-dimensional tracking planes composed of hydro-carbon scintillator bars and has 4π acceptance. The design is described in chapter 2. The characterization of MPPC, which is used for detection of scintillation light, is described in chapter 3. The detector adopts new electronics based on ASIC chips, SPIROC2D, and the development of electronics is also one of characteristics. It is described in chapter 4. We have constructed Water Module from October, 2016 and finished it in August, 2017. The construction and installation are described in chapter 5. The performance test with cosmic ray is described in chapter 6. The neutrino beam measurement started in October, 2017 and it is described in chapter 7.

Chapter 2

Design of WAGASCI detector

2.1 Motivation

WAGASCI experiment is proposed to measure the charged-current neutrino cross-section ratio between water and hydrocarbon with large phase space in order to reduce the uncertainties due to cross section in the T2K neutrino oscillation analysis. The goals of this experiment are:

1. to measure the charged current cross-section ratio of water to hydrocarbon with 3% uncertainty.

2. to measure the charged current cross section on water and hydrocarbon individually with large phase space.

2.2 Design of WAGASCI experiment

2.2.1 Original design

The WAGASCI experiment has been conducted in the T2K neutrino near detector hall at J-PARC. The detectors are located on the 1.5° off-axis from the neutrino beam center, where the neutrino energy spectrum is a similar to that of T2K, on the 2.5° off axis. Figure 2.1 shows the neutrino beam flux in terms of neutrino energy spectrums on 0.00°, 1.06°, 1.50°, 2.50°. Figure 2.2 shows the position of detectors.

The detectors of WAGASCI experiment are composed of several modules as shown in Fig. 2.3. The central module is an active target detector. It is composed of two modules which contain water and hydrocarbon targets. The side two modules are muon range detectors(MRDs). The downstream module is also MRD, but it is magnetized in order to identify the charge of particle. Both of side MRDs and downstream MRD consist of tracking planes and iron plates.

The size, mass and electronics of each module are different but the detection method is same. Each detector contains plastic scintillator bars. Charged particles passing scintillators generate scintillation light, which is collected by the wave length shifting fibers(WLSFs) and detected by multi-pixel photo counters(MPPCs) that are semiconductor detectors produced Hamamatsu Photonics.

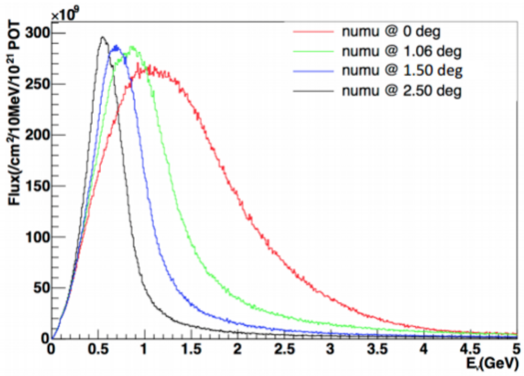

Figure 2.1: The neutrino beam flux in terms of neutrino energy spectrums on 0.00°, 1.06°, 1.50°, 2.50°. The mean energy on 1.50° and 2.50° is about 600MeV.

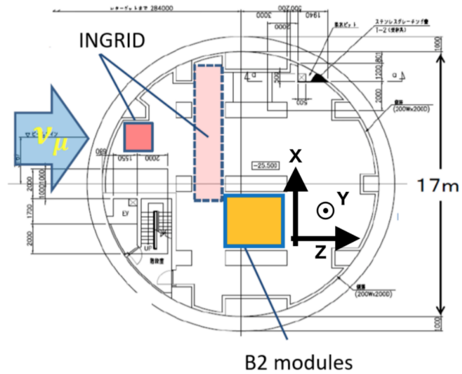

Figure 2.2: The position of the detectors installed. The area named B2 module is for WAGASCI.

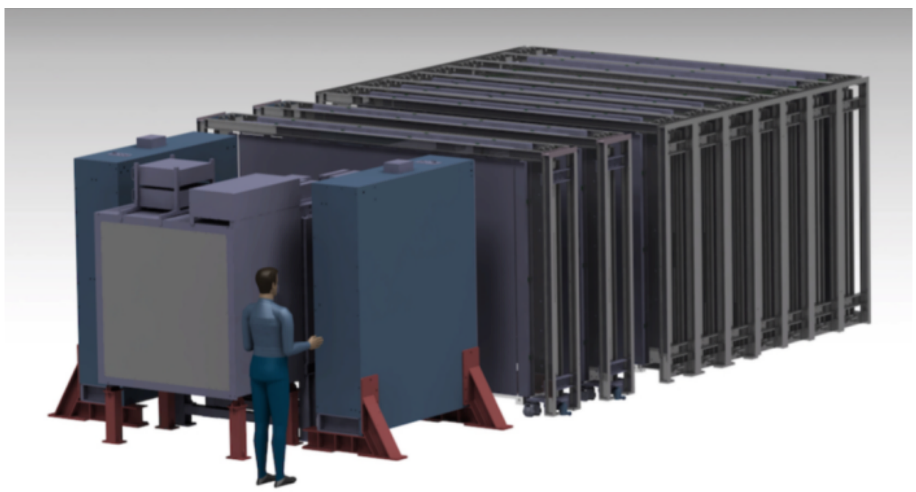

Figure 2.3: A schematic view of the design of WAGASCI experiment.

Table 2.1 shows the expected number of selected neutrino-candidate events in Water Module at 1.50° off-axis place with 5.0×10^{20} proton on targets in each of neutrino mode and anti-neutrino mode[19].

2.2.2 Current Setup

Because side MRDs are under construction and downstream MRD is under transportation, we have started detector performance test and neutrino beam measurement with central detectors and alternative downstream MRD on the 1.5° off-axis. The current temporary setup is shown in Fig. 2.4. Water Module, which is the main active target detector, is used as the central water target detector. Proton Module[20] is used as the central hydrocarbon target detector and INGRID module[21] is used as the downstream MRD. Water Module is mainly composed of plastic scintillator bars and water and Proton

Table 2.1: The expected number of the selected neutrino-candidate events in Water Module with 5.0×10^{20} proton on targets in each of neutrino mode and anti-neutrino mode. The vertex is required to be 50mm away from the edge of the detector and the longest track is required to penetrate more than one (five) iron plates in the side MRD (downstream MRD).

beam mode	CC on H_2O	NC on H_2O	Interaction on CH	wrong sign interaction
ν mode	4239	107	1087	(negligible)
$\bar{\nu}$ mode	1666	14	560	(561)

module is composed of scintillator bars, so neutrino cross-section ratio of water to hydrocarbon can be measured by comparing neutrino event rate of these two central active target detectors. INGRID module is composed of scintillator tracking planes and iron plates so it has strong stopping power for charged particles and has enough performance as downstream MRD. However, INGRID module is not magnetized unlike original downstream MRD. The absence of magnetic field makes charge identification impossible, so the contamination of background from opposite neutrino is not negligible especially in case of $\bar{\nu}_\mu$ beam measurement. Also the absence of side MRDs makes energy reconstruction for particles scattering to high angle difficult because such a particle is likely to go out from central detectors without depositing all kinetic energy in the modules. It makes measurable phase space restricted.

The neutrino beam measurement with this temporary setup has started in October 2017 and is planed to continue until 2018. The detector performance test for Water Module, which is the one of the main topic of this thesis, is done under this temporary setup.

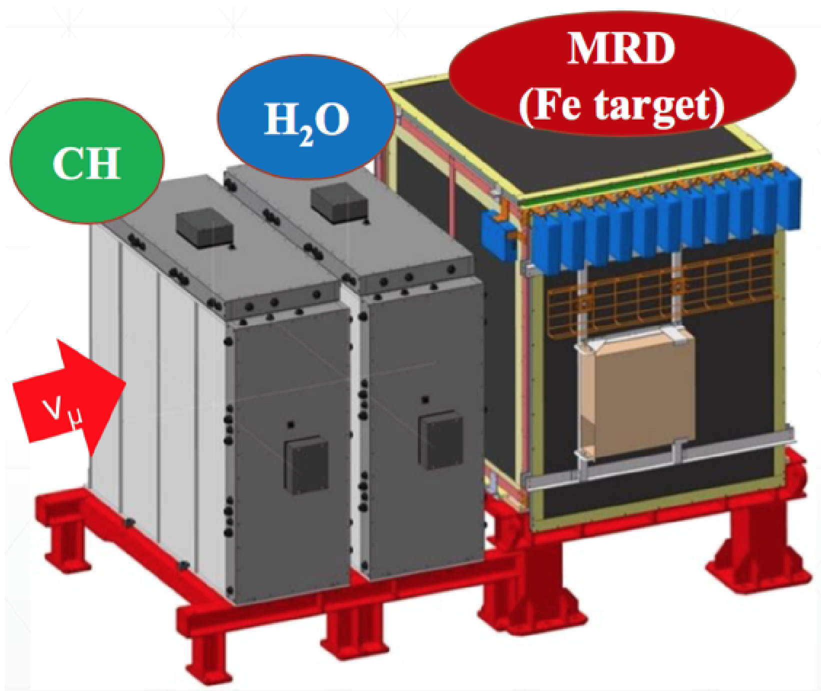

Figure 2.4: A schematic view of current setup.

INGRID module, which is used as the downstream detector, consists of sandwich structure of 11 tracking scintillator planes and 9 iron plates as shown in Fig. 2.5[21]. They are surrounded by 4 veto planes to reject charged particle incoming from outside the module. A iron plate is sized 1240×1240×65mm^3. A tracking scintillator plane is composed of 24 scintillator bars in the horizontal direction and 24 bars in the vertical direction. Iron plate is not placed between 10th and 11th tracking planes. Veto plane is composed of 22 scintillator bars. All scintillator bars are made of mainly polystyrene, surrounded by reflector including TiO_2. A scintillator bar of tracking plane is sized 50×1203×10mm^3 and that of veto plane is 50×1299×10mm^3 (top, right and side) and 50×1119×10mm^3 (bottom). The total number of channels of a module is 576.

Each scintillator bar has a hole whose diameter is about 3mm at the center of the scintillator bar to insert a wave length shifting fiber to collect scintillation light. The same wave length shifting fiber, Y-11(200M), as Water Module is used. The surface of the fiber is polished and one side of the fiber is attached to a MPPC, S10362-13-050C[22]. The fiber and MPPC are contained in a dark box. The MPPC signal is transported to the Trip-t front-end board(TFB) by a coaxial cable. A TFB is connected to 48 MPPCs. TFB is mounted outside the dark box.

The MPPC signal is split 1:10 and routed to two separate channels of the ASIC, high gain and low gain, to increase dynamic range. The limit of dynamic range is 500 p.e. in current operation. The charge is integrated and recorded together with hit timing. The bias voltage applied to the MPPCs is typically 70V and the threshold is set to 2.5 p.e. equivalent level.

The Trip-t chip integrates charge in integration windows, which are synchronized with the neutrino beam structure. Integrated charge is reseted after the integration window closed and it takes at least 50ns. The integrated charge is stored in 23-deep analogue memory. The stored charge is converted to digital signal with 10-bit ADC. The discriminator is routed to high gain and hit timing is measured in accuracy of 2.5ns.

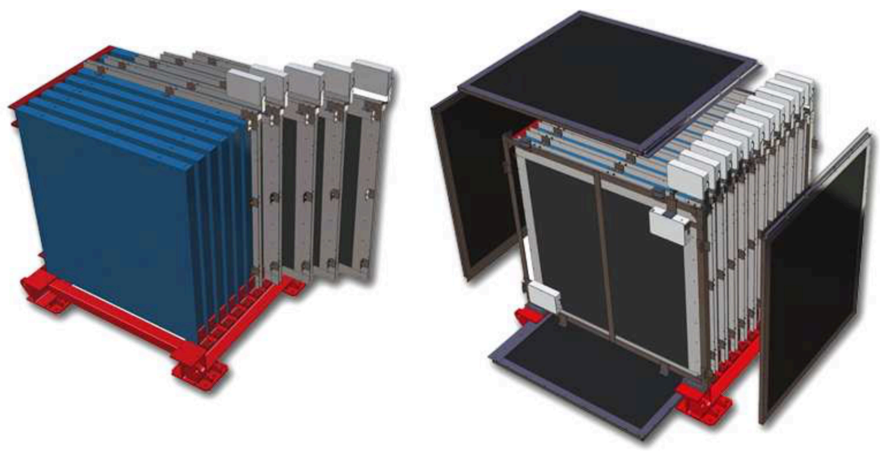

Figure 2.5: The schematic view of a INGRID module.

Proton Module, which is used as the active target detector of hydro-carbon, consists of 2 upstream tracking planes and 34 downstream tracking planes surrounded with 4 veto planes as shown in Fig. 2.6[20]. Two types of scintillator bars are used as the component of tracking planes. One is the same one as the scintillator bars of INGRID tracking planes. The size is 50×1203×10mm^3. Here, this scintillator bar is called as INGRID-type. The other is similarly made of mainly polystyrene and surrounded by reflector and is sized 25×1203×13mm^3. It is called as SciBar-type. An upstream tracking plane is composed of 24 INGRID-type scintillator bars. A downstream tracking plane is composed of 16 SciBar-type scintillator bars. It is composed of 16 INGRID-type bars and 16 SciBar-type bars, and the central part consists of SciBar-type and the outer part consists of INGRID-type. It is for maximizing the vertex resolution and mass in the central part of the detector where neutrino detection efficiency is highest. Each tracking plane is alternately placed in the two perpendicular directions to the beam direction. Veto plane is composed of 17 scintillator bars, which are sized $50\times1250\times10\text{mm}^3$. The total number of channels is 1204.

As INGRID-type scintillator bars, the SciBar-type scintillator bar has a hole whose diameter is about 1.8mm at the center of the scintillator bar to insert a wave length shifting fiber to collect scintillation light. The same wave length shifting fiber, Y-11(200M), as is used for Water Module. The surface is also polished and one side of the fiber is attached a MPPC, which is the same type as INGRID one. The same readout electronics as INGRID is used.

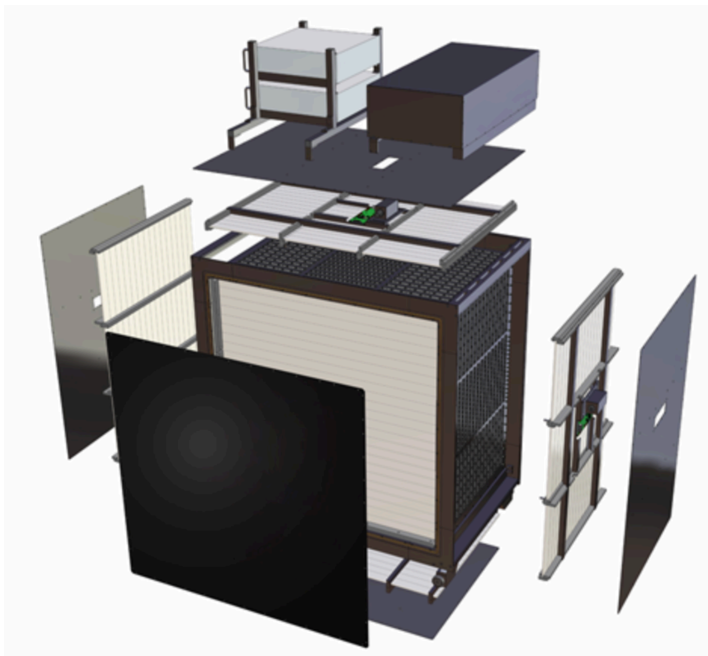

Figure 2.6: The schematic view of Proton Module.

2.3 Water Module

Water Module, which is one of the central active target detectors, is composed of stainless tank, 16 scintillator tracking planes and water. A schematic view of Water Module is shown in Fig. 2.7. The stainless tank is filled with 0.5 ton water and is sized as $460\times1250\times1250$ mm^3. 1280 scintillator bars form 16 scintillator tracking planes which are immersed in the water. Each tracking plane has 80 scintillator bars and 40 of them are placed perpendicularly to the beam direction and called parallel scintillator. The others are placed in parallel to the beam direction and called grid scintillator. The grid scintillators make a three-dimensional grid structure with $50\times50\times25$ mm^3 cells. Each tracking plane, consisting of 40 parallel scintillator and 40 grid scintillator, is alternately placed in the two perpendicular directions to the beams direction. It enables three-dimensional tracking reconstruction. Figure 2.8 is a schematic view of the all scintillators from X direction and Y direction where the definition of used coordinators is shown in Fig. 2.2. There are 1.5mm gaps between two neighboring planes to avoid air bubbles inside cells.

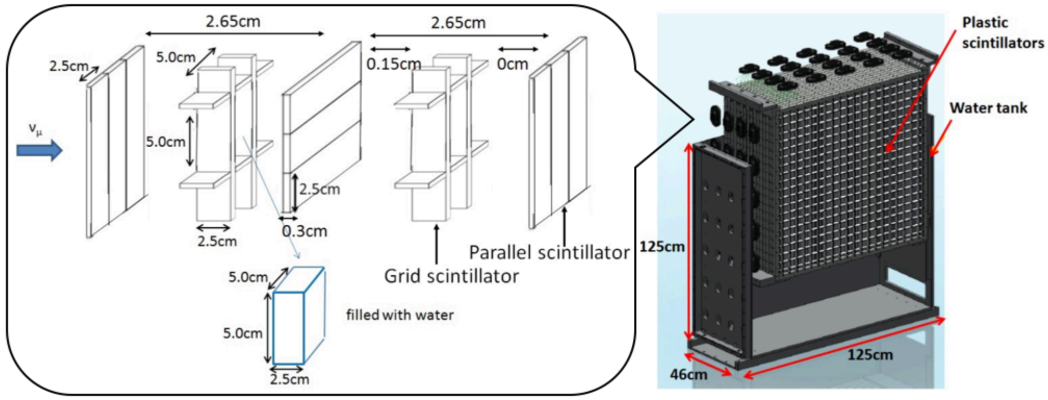

Figure 2.7: A schematic view of Water Module and that of tracking planes and filled water.

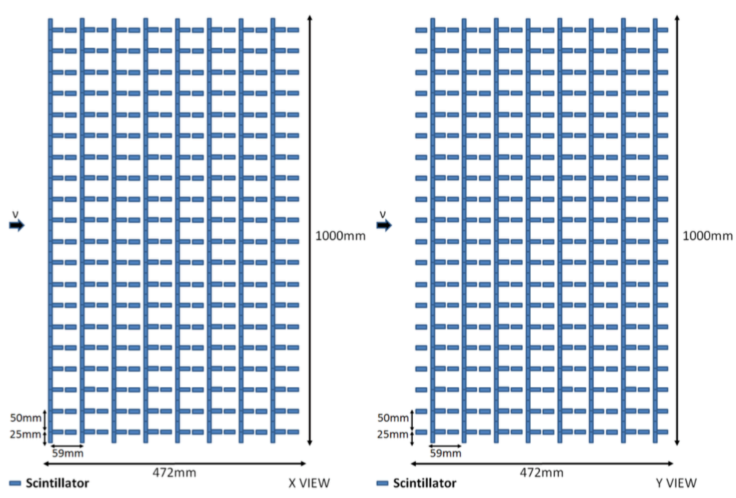

Figure 2.8: A schematic view of Water Module from X direction(left) and Y direction(right)

The geometry of plane and grid scintillators is shown in Fig. 2.9. The scintillator bars are mainly composed of polystyrene, surrounded by reflector including TiO_2, with dimensions of $24.5\times1020\times3$ mm^3. Both of plane and grid scintillators have groove sized $1.2\times1020.0\times1.2$ mm^3 on the surface to collect scintillation light by a wave length shifting fiber. A grid scintillator bar have a 50-mm-interval slit to form the grid structure. The wave length shifting fiber, Y-11(200)M, is produced by Kuraray company and the diameter is 1.0mm. The wave length shifting fiber is glued by optical cement and reflector is painted over optical cement to collect light more efficiently. Because crosstalk of light due to the reflection of scintillation light on the inner surface of each cell has been observed while the commissioning of prototype module, all the scintillator bars are painted black to suppress crosstalk as shown in Fig. 2.10. It is confirmed by measurements with cosmic rays that black painting on the surface of the scintillator bars suppresses the crosstalk so that no significant crosstalk effect is observed within uncertainty.

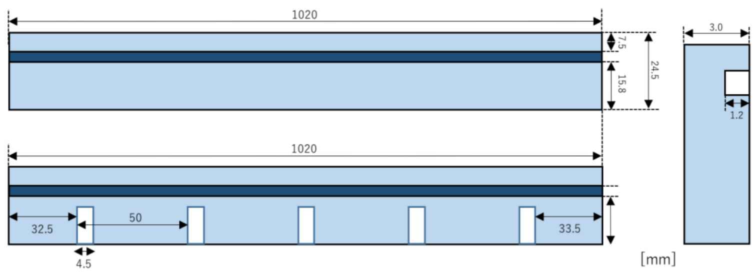

Figure 2.9: The geometry of parallel scintillator(left up), that of grid scintillator(left down) and cross section of both of them(right). The unit is mm.

Figure 2.10: The scintillators before machining(bottom) and after spraying with black(top).

A tracking plane consists of 40 grid scintillators placed to make a nesting structure and 40 parallel scintillators placed above them. Each scintillator bar is fixed to frame, which is made by ABS resin and has holes to lead wave length shifting fibers, with silicon adhesive bond. There are two types of tracking planes, X tracking plane and Y tracking plane, of which the direction of parallel scintillators is perpendicular. A sub-module consists of two X tracking planes and two tracking planes.A sub-module has 320 wave length shifting fibers and each 32 of them are bundled in a fiber cookie. A fiber cookie has 4×8 arrayed fiber holes, which is designed to fit the 32-channel arrayed MPPC, S13360(ES2). The wave length shifting fibers are fixed to fiber cookies by optical cement. The surface is polished by a diamond grinder.

The MPPC is a product of Hamamatsu Photonics, S13660(ES2), with suppressed noise rate of 60kHz per channel at 0.5 photo electron and crosstalk rate of 3% with typical operation voltage. It has 4×8 arrayed channels which have individual ground and signal lines. The diameter of sensitive area is 1.5mm and the pixel pitch is 50 μm. A channel has 716 pixels of APD in a round shape .

For readout and operation of a number of channels of MPPC, a SiPM Integrated Read-Out

Chip(SPIROC)[23] based electronics has been developed. SPIROC, which is developed by OMEGA group, is a 36-channel self-triggered front-end ASIC. It not only contains an analogue signal processing part such as amplification, shaping of waveform and discriminator, but also contains a digital signal processing part such as self-trigger and an analogue to digital converter for charge and time. Charge of MPPC signal is sampled by track-and-hold circuit. The front-end board, named Active Sensor Units(ASU), has been developed with the SPIROC2D chip which is the second latest version of SPIROC. Each readout board is designed to control 32 channels arrayed MPPC, and the 40 ASU boards are aligned on the surface of Water Module as shown in Fig. 2.11. The data acquisition system used for this detector, including back-end boards, has been developed for prototypes of ultra-granular calorimeters for the International Linear Collider (ILC)[24]. More detail is described in the chapter 4.

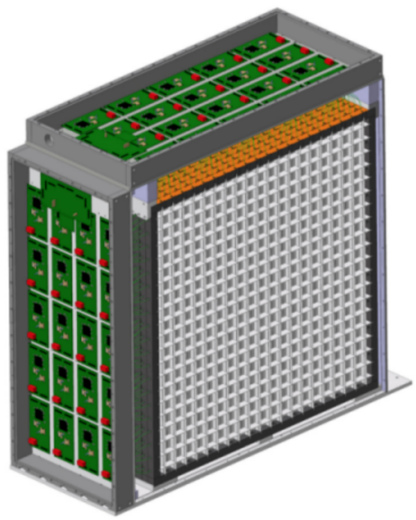

Figure 2.11: The schematic view of the alignment of ASUs and Interface board.

2.4 Other modules

As described above, side MRDs and original downstream magnetized MRD are not installed in current setup. Installation is planed in 2018 and neutrino beam measurement plans to start later in 2018. The design of the side MRDs and downstream MRD is described here. Their construction and performance are not covered in this thesis.

2.4.1 Side MRD

The side MRD is the side muon range detectors consisting of two modules which are placed at both side of the central detector. Each module consists of sandwich structure of 11 iron plates and 10 tracking planes. Each tracking plane is placed with the 13mm gap to iron plates. A iron plate is sized $30\times1610\times1800\text{mm}^3$. A tracking plane is composed of 8 scintillator bars with the dimension of $7\times200\times1800\text{mm}^3$. A scintillator bar is composed of mainly polystyrene and surrounded by reflector and a sinusoidal groove is milled along a scintillator bar to provide uniform light collection over the whole scintillator surface. A wave length shifting fiber, which is same as one used for Water Module, is glued with the optical cement in the S-shape groove. Both sides of fiber are glued into optical connector. The surface is polished and both sides are attached to MPPCs, S13081-050CS(X1). The MPPC signal is transported to a single MPPC card by a coaxial cable. The single MPPC card is a relay device between single MPPCs and a ASU board and it connects 32 channels of MPPC.

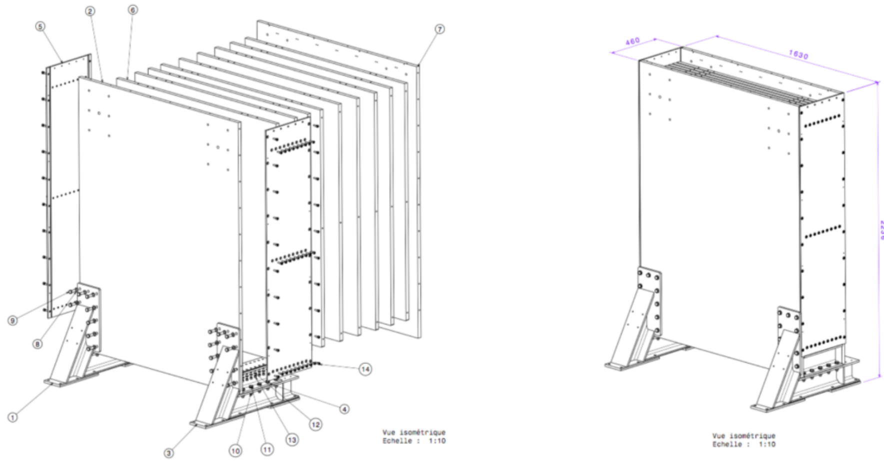

Figure 2.12: The schematic view of side MRD.

2.4.2 Downstream MRD

The downstream MRD, named Baby MIND[25], is the magnetized muon range detector which is placed at the downstream of the active target detectors for charge identification. Baby MIND consists of 33 iron modules and 18 tracking planes as shown in Fig. 2.13. An iron module is composed of an iron plate and coils. An iron module is sized $3500\times2000\times50\mathrm{mm}^3$ and its weight is 1900kg. The magnetic field is 1.5T for current of 150A and it is confirmed to be uniform over the central tracking region by the simulation as shown in Fig. 2.14. It is also confirmed by the test measurement with 9 pick-up coils.

A tracking plane is composed of 95 horizontal scintillator bars and 16 vertical scintillator bars. A horizontal bar is sized $2880\times31\times7.5\mathrm{mm}^3$ and has a groove along the long side of the bar to insert a wave length shifting fiber. A vertical bar is sized $1950\times210\times7.5\mathrm{mm}^3$ and U-shaped groove along the bar. The surface is polished and either side of a fiber of a horizontal bar is attached MPPCs, S12571-025C and both sides of a vertical bar are attached.

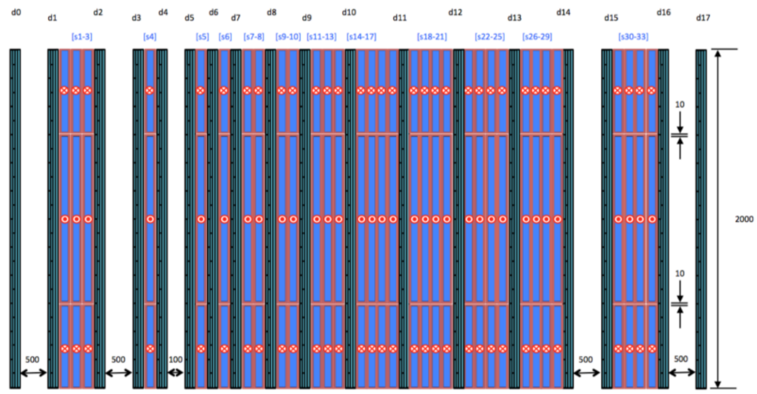

Figure 2.13: The schematic view of BabyMIND with muons incident from the left. Scintillator modules are referenced d0 to d17, magnet modules are referenced s1 to s33.

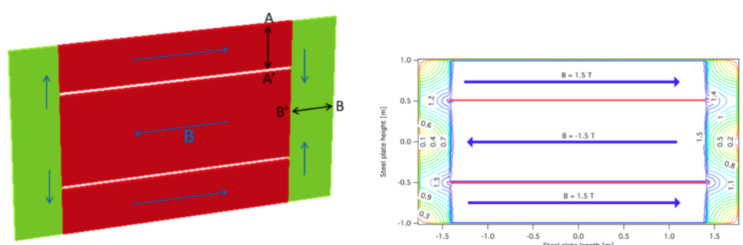

Figure 2.14: Complete return of the magnetic flux requires cross-sections A-A' and B-B' to be equal (left). Magnetic field map with a 280cm long coil, 1.5kA (right figure).

Chapter 3

Characterization of MPPC

The characteristics of MPPC are measured for eighty four 32-channel arrayed MPPCs for central module and about 1400 single MPPCs for MRDs. The specifications of arrayed MPPCs, named S13660(ES2), are listed on the Table.3.1 and that of single MPPCs, named S13081-050CS(X1) is listed on Table.3.2. Figure 3.1 shows the 32-channel arrayed MPPC and an enlarged view of a channel.

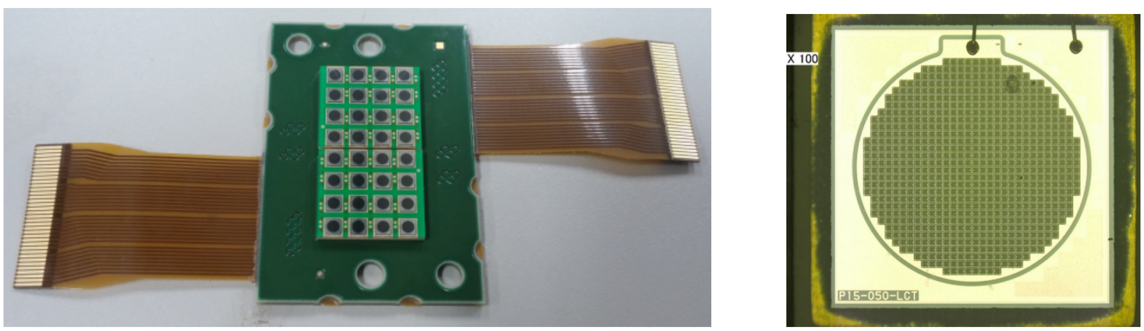

Figure 3.1: The view of 32-channel arrayed MPPC and an enlarged view of a channel.

Table 3.1: basic characteristic : S13660(ES2).

pixel pitch	50μm
size of sensitive area	ϕ1.5mm
operating temperature	-20 - 60°C
number of pixels	716
fill factor	74%
operating voltage(typ.)	53±5V
dark noise(typ.)	60kHz
cross talk probability(typ.)	3%

Table 3.2: basic characteristic : S13081-050CS(X1).

pixel pitch	50μm
size of sensitive area	1.3mm×1.3mm
operating temperature	-20 - 60°C
number of pixels	667
fill factor	74%
operating voltage(typ.)	53±5V
dark noise(typ.)	60kHz
cross talk probability(typ.)	1%

Measurement items are as follows.

1. Gain
2. Breakdown voltage
3. Crosstalk rate

4. Relative photo detection efficiency

3.1 Measurement setup

The measurement setup for mass measurement follows the thesis of F.Hosomi[26]. The schematic of measurement setup is shown in Fig. 3.2. Measured MPPCs are in a thermostatic bath with a reference MPPC which is used for measurement of relative photo detection efficiency as shown in Fig. 3.3. In the thermostatic bath, temperature is always set to $20°C$. MPPCs are connected on a readout circuit board as shown in Fig. 3.4 and the signal is transported to EASIROC[27]. Two EASIROC modules are used and one is used for readout of measured MPPCs and the other is for readout of reference MPPCs. These two EASIROC modules are synchronized and it makes the measurement of photo detection efficiency enable by comparing the light yield of measured MPPC to that of reference MPPC. ESIROC also controls the switch of blue LED. The intensity of blue LED can be controlled by amplifier and the intensity is set so that the mean of photo electrons measured by MPPC is 2-3 p.e. To get uniform light, several blue LEDs are placed in symmetrical position and a diffuser is placed between LEDs and MPPCs. It makes light intensity uniform within 3%. For each set of MPPCs, measurements are repeated several times with changing bias voltage and LED on and off respectively. The measurement and analysis automatically proceed and the data quality check and replacement of MPPC are done by hand. The stability of bias current, stability of temperature, correlation between MPPC parameters and bias voltage and the photo electron spectrum are checked and if there is a problem on MPPCs, such a MPPC is measured later again. If the same problem happens, the MPPC is rejected as a bad sample. The surface of MPPCs is wiped with absorbent cotton dipped with ethyl alcohol after measurement and MPPCs are stored in the dark box with packing materials.

Two arrayed MPPCs or 64 single MPPCs can be measured in 1 cycle. It takes two hours for 1cycle. It takes at least 64 cycles to measure all MPPCs.

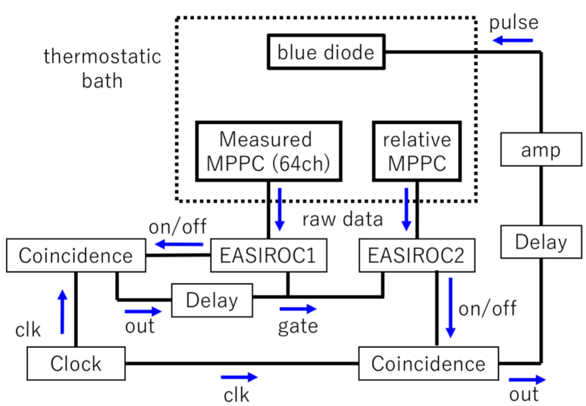

Figure 3.2: Setup for performance test of MPPC.

3.2 Gain and breakdown voltage

Gain of MPPC is approximately proportional to the bias voltage. The output charge of a pixel is given as

$$Q_{1p.e.} = C(V_{bias} - V_{bd}) \tag{3.1}$$

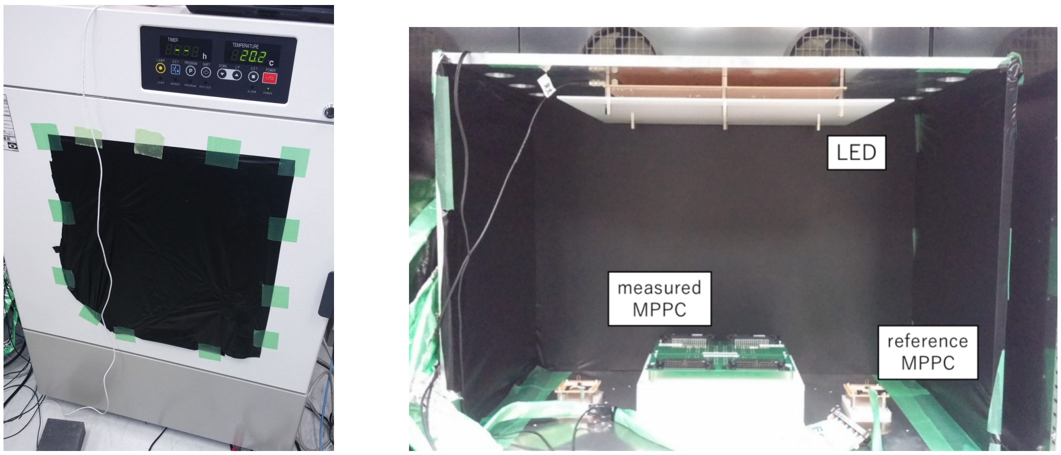

Figure 3.3: Picture of thermostatic bath(left) and setup of MPPC inside the thermostatic bath(right).

Figure 3.4: The readout circuit board for 32-channel arrayed MPPC(left) and for 64 single MPPCs(right)

$$\Delta V = V_{bias} - V_{bd}, \tag{3.2}$$

where C is a capacitance of MPPC, V_{bias} is the bias voltage and V_{bd} is the breakdown voltage of MPPC. Gain is calculated by the distance of two neighboring peaks as

$$Gain = M_{i+1} - M_i, \tag{3.3}$$

where M_i is the mean ADC count of i-th peak. The position of peaks is measured by fitting ADC distribution by four gaussian ash shown in 3.5. A result for a channel is shown in Fig. 3.6. It is fitted by linear function and breakdown voltage is extrapolated. The error of fitting parameter is about 0.5% and gain is measured with an accuracy of 0.1 ADC count and breakdown voltage is measured with an accuracy of 0.1 V.

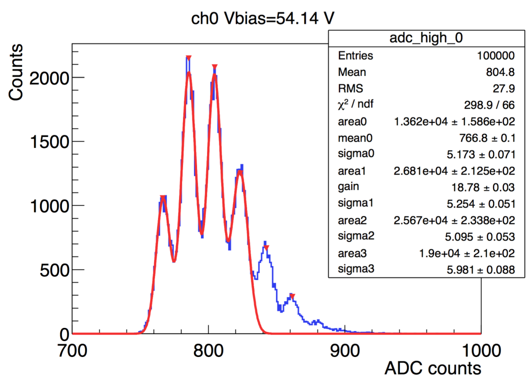

Figure 3.5: ADC distribution, fitted by four gaussian.

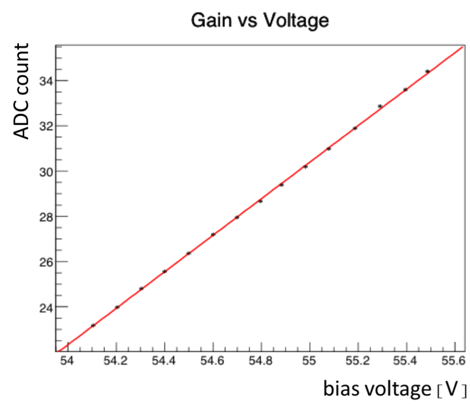

Figure 3.6: The correlation between bias voltage and gain.

The breakdown voltage for 76 arrayed MPPCs is shown in Fig. 3.7 and that for 1400 single MPPCs is shown in Fig. 3.8. The individual difference of gain and breakdown voltage of arrayed MPPC are larger than that of single MPPC. Breakdown voltage of arrayed MPPC is about 1.0V less than that of single MPPC. Figure 3.9 shows gain of arrayed MPPC with ΔV =3.0 V and Fig. 3.10 shows that of single MPPC. 97% of all channels of arrayed MPPCs is in the 10% range and all single MPPCs is in the 10% range.

3.3 Dark noise rate

MPPC dark noise is mainly due to thermal electron-hole pair production which induces avalanche multiplication. Dark noise is measured by counting the number of the signal over 0.5 p.e. This measurement is very sensitive to electric noise as shown in Fig. 3.11, so about 10-20% of all channels cannot be measured.

Figure 3.12 is the correlation between dark noise rate and bias voltage. Dark noise rate is proportion to breakdown voltage in the certain voltage range. Figure 3.13 shows dark noise rate of arrayed MPPC with ΔV =3.0V and Fig. 3.14 shows that of single MPPC. Almost all channels in the range from 30kHz to 100kHz. The result is shown except the channels which cannot be measured due to the electric noise.

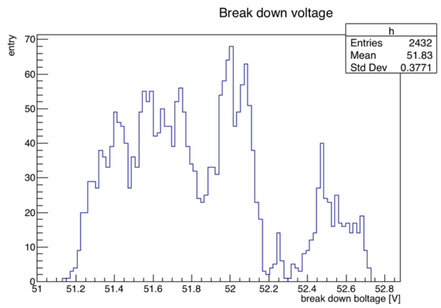

Figure 3.7: Breakdown voltage for 76 arrayed MPPCs.

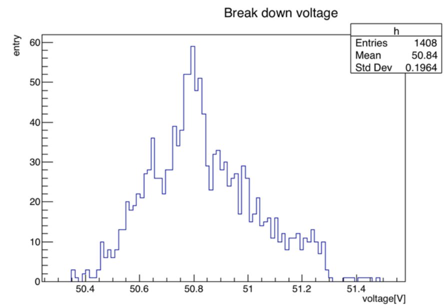

Figure 3.8: Breakdown voltage for 1400 single MPPCs.

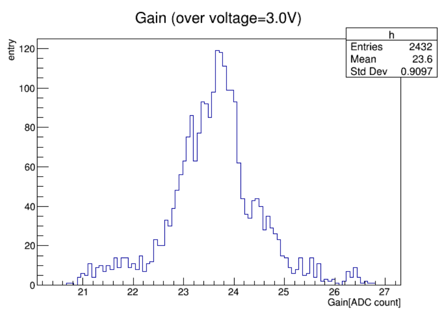

Figure 3.9: Gain of arrayed MPPC when ΔV =3.0 V.

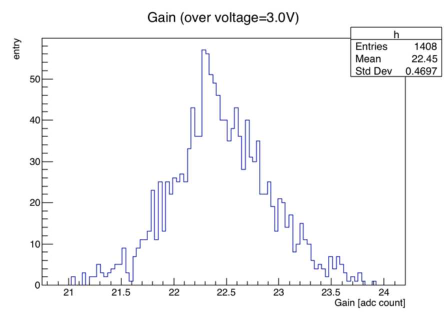

Figure 3.10: Gain of single MPPC when ΔV =3.0 V.

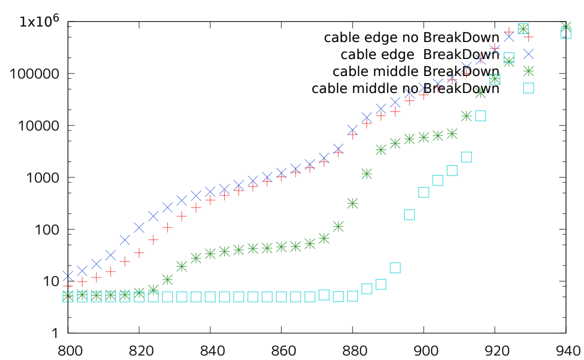

Figure 3.11: Scurve of noise rate without MPPC(red and light green) and with MPPC(blue and green). X axis is DAC value of threshold and y axis is noise rate. The red and blue line is for noisy channel and the others is for stable channel. Typical Scurve is seen at the stable channel. However, at the noisy channel, there is almost no difference between with and without MPPC. For such a channel, noise can not be measured.

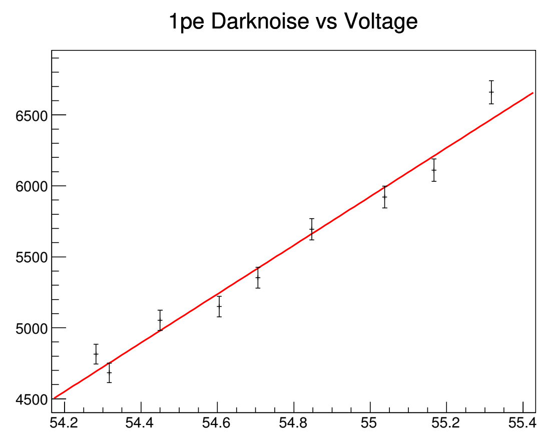

Figure 3.12: The correlation between bias voltage and dark noise rate.

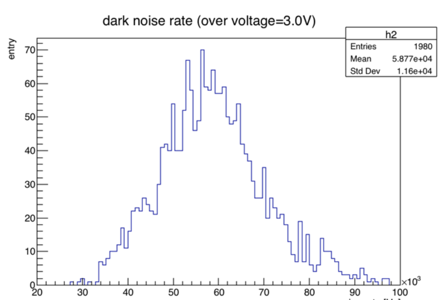

Figure 3.13: Dark noise rate of arrayed MPPC with ΔV =3.0 V.

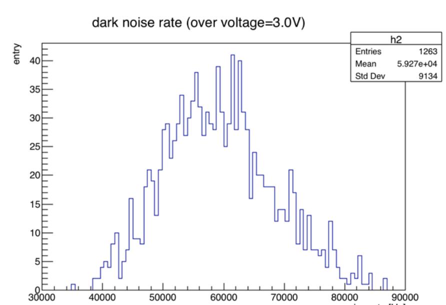

Figure 3.14: Dark noise rate of single MPPC with ΔV =3.0 V.

3.4 Crosstalk

The avalanche multiplication in a pixel sometimes induces the electron-hole pair in another pixel. It makes MPPC output get higher than true output. It is called crosstalk. Crosstalk probability is calculated by following equation.

$$Crosstalkprobability = \frac{Dark\ noise\ rate_{2p.e.}}{Dark\ noise\ rate_{1p.e.}} \tag{3.4}$$

Figure 3.15 shows the correlation between 2p.e. dark noise rate and bias voltage. Figure 3.16 shows crosstalk probability of arrayed MPPC with ΔV =3.0V and Fig. 3.17 shows that of single MPPC. Same as the measurement of dark noise, the result is shown except the channels which cannot be measured due to the electric noise. The dark noise rate is not so different between single MPPC and arrayed MPPC, but it is clear the crosstalk of single MPPC is more strongly suppressed.

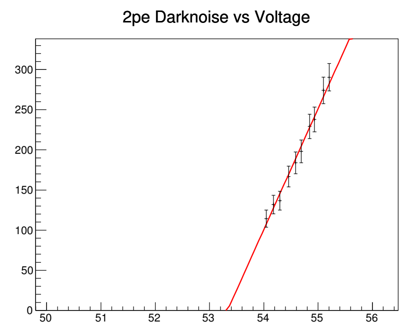

Figure 3.15: The correlation between 2p.e. dark noise rate and breakdown voltage.

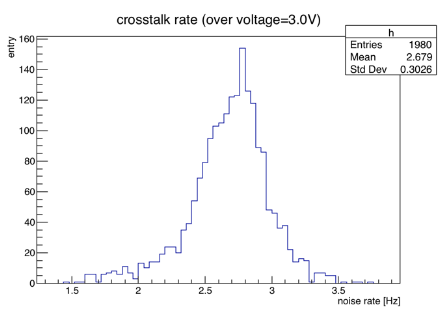

Figure 3.16: Crosstalk rate of arrayed MPPC with ΔV =3.0V.

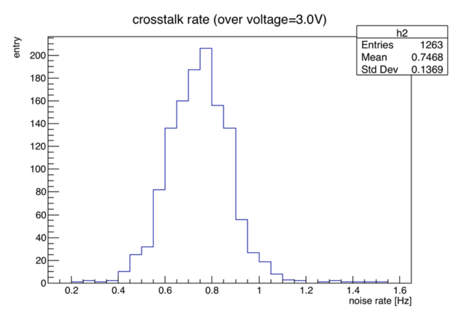

Figure 3.17: Crosstalk rate of single MPPC with ΔV =3.0V.

3.5 Relative photo detection efficiency

It is difficult to measure the absolute number of photon, so relative photo detection efficiency(PDE) is measured by comparing light yield to reference MPPC. The mean light yield is calculated by the assumption of the Poisson distribution as following equation

$$\lambda = -ln[Poisson(0)] = -ln(\frac{N_{pedestal}}{N_{total}}), \tag{3.5}$$

where λ is mean light yield, $N_{pedestal}$ is the number of events of pedestal and N_{total} is the number of total events. Then, the relative PDE is given as

$$relativePDE = \frac{\lambda_{sample}}{\lambda_{reference}} \tag{3.6}$$

$N_{pedestal}$ is measured by fitting ADC distribution by four gaussian in the same way as the measurement of gain. Figure 3.18 shows the correlation between relative PDE and bias voltage. Figure 3.19 shows relative PDE of arrayed MPPC with ΔV =3.0V and Fig. 3.20 shows that of single MPPC. Uniformity of light intensity is about 3%, so the deviation is not due to the individual difference of MPPCs but due to ununiformity of light intensity.

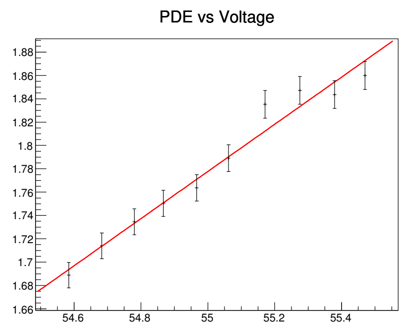

Figure 3.18: The correlation between relative photo detection efficiency and bias voltage.

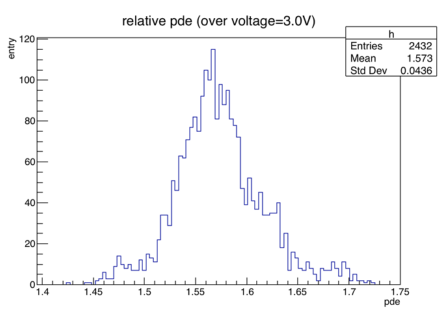

Figure 3.19: Relative PDE of arrayed MPPC with ΔV =3.0V.

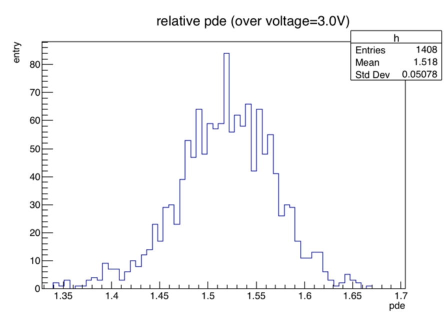

Figure 3.20: Relative PDE of single MPPC with ΔV =3.0V.

3.6 Bad arrayed MPPC

8 of 84 arrayed MPPCs are rejected as bad samples because the current is much more than that of good ones. We examine them with Hamamatsu and it is confirmed that the scratch made while manufacture process induces over current. Over current generates heat and it makes a short circuit. It is also confirmed by an endurance test that neither of short circuit nor current happens for good MPPCs.

3.7 Summary

Performance of 32-channel arrayed MPPC, S13360(ES2), and single-channel MPPC, S13081-050CS(X1), are measured. 76 of 84 arrayed MPPCs and all single MPPCs are good and 8 arrayed MPPC are rejected as bad samples. Table.3.3 lists the summary of performance test. The individual difference of arrayed MPPCs is larger than that of single MPPCs and the typical performance of gain, noise rate and relative PDE is same. Crosstalk of single MPPCs is 3 times more suppressed. Both of arrayed MPPCs and single MPPCs have sufficient performance and it is confirmed that MPPCs meet requirement.

Table 3.3: Summary of performance test with ΔV =3.0V

		S13360(ES2)	S13081-050CS(X1)
Number	Good	76	1400
	Bad	8	0
Gain [ADC Count]	Mean	23.60	22.45
	Std Dev.	0.91	0.47
Breakdown voltage [V]	Mean	51.83	50.84
	Std Dev.	0.38	0.20
Noise rate [kHz]	Mean	59	59
	Std Dev.	11	9
Crosstalk rate [%]	Mean	2.7	0.74
	Std Dev.	0.3	0.14
relative PDE	Mean	1.57	1.52
	Std Dev.	0.04	0.05

Chapter 4

Development of electronics and data acquisition system

The electronics of the WAGASCI experiment, including the whole DAQ system, has been developed at Laboratoire Leprince-Ringuet (LLR) of l ' Ecole polytechnique. The front-end and back-end board based on SPIROC chips have been developed. In this chapter, the development of the front-end board with SPIROC2D and developed data acquisition system are described.

This chapter consists of three parts. First part is about the requirement for electronics. Second part is about the description of design of electronics. Last part is about the test measurement of electronics. The overview of last part from the prototype board test measurement to tuning of electronics is listed up as following:

1. Test of basic characteristics with an ASU board.
   Basic characteristics of front-end board including threshold problem, hit timing measurement and charge measurement are tested. In this step, we confirm that the front-end board has sufficient performance for neutrino beam measurement.

2. Operation test with several boards.
   First operation with multi boards is tested. In this step, we confirm the front-end board has no problem and it is ready for mass production.

3. Operation test with a individual board for all boards.
   The operation test is for mass products. In this step, all boards are produced correctly.

4. Operation test with full setup.
   First operation with full setup as shown in Fig. 4.2 is tested. In this step, we confirm the whole electronics system works.

5. Test of basic characteristics and tuning of all boards for beam measurement.
   The basic characteristics of all boards with full setup is tested and all boards are tuned.

In the section4.3, first and second items are described. In the section4.4, the other items are described.

4.1 Requirements

Requirements from WAGASCI experiment for electronics are:

1. Charge measurement for track reconstruction and particle identification.
2. Hit timing measurement for neutrino event selection.
3. Stable control of 1280 channels of 32-arrayed MPPCs.

The typical light yield is about 10 p.e. per 3mm. So, charge measurement up to about a hundred p.e. is required for electronics. Charge resolution to measure MPPC signal peak one by one is also required.

T2K neutrino beam structure is shown in Fig. 4.1. Neutrino beam bunch comes 8 times every 581ns and the width of a bunch is 58ns. It is minimum requirement to distinguish two beam bunches. In order to measure the direction of particles, more precise hit timing measurement, about 1ns, is required.

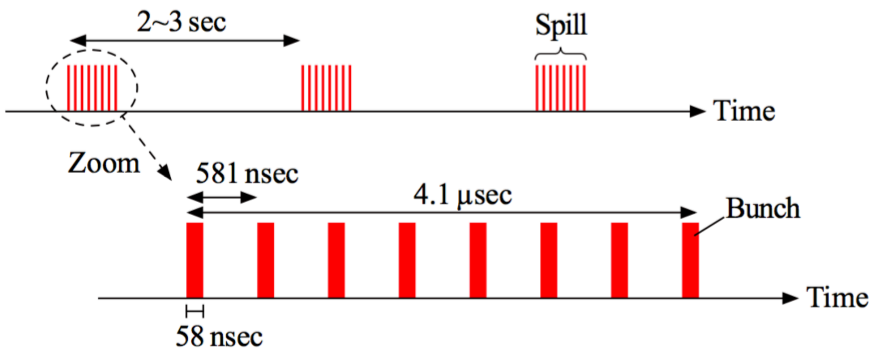

Figure 4.1: T2K neutrino beam structure.

4.2 Design of electronics

4.2.1 Overview

The SPIROC based WAGASCI readout and data acquisition system are shown in Fig. 4.2. Each SPIROC front-end board named Active Sensor Unit(ASU) processes a 32-channel arrayed MPPC. 20 ASUs are attached to a side of the detector for readout of 640 channels of MPPCs. The total number of required ASUs is 40. The control and readout signals from 20 ASUs are processed through an interface board (IF) and a detector interface board (DIF) which controls SPIROC chips, supplies the voltage, sends data acquisition signal and processes both of response signals and output data from chips. The DAQ signal is transported to ASUs serially and they configure a daisy chain. Each ASU and IF are connected with two 50-conductor flat cables. A DIF and an IF are connected with a 90-pin connector. Giga data concentrator card(GDCC) communicates with DAQ PC. DIF and GDCC are connected with a HDMI cable and the output data from 2 DIFs is sent to DAQ PC by one GDCC. The Clock and Control Card (CCC), where a global trigger decision is taken, receives the beam timing trigger and transmits clock and synchronous trigger to front-end boards via GDCC. The control and configuration of electronics including bias voltage to MPPCs are set remotely by PC. Beam trigger information is transported by Zed board, which is a FPGA evaluation board. Zed board converts 16-bit trigger number signal to hexadecimal data and send the data to GDCC via the hub. Figure 4.3-4.6 show the view of ASU, IF, DIF and GDCC. Table.4.1 shows the number of front-end and back-end boards used in Water Module.

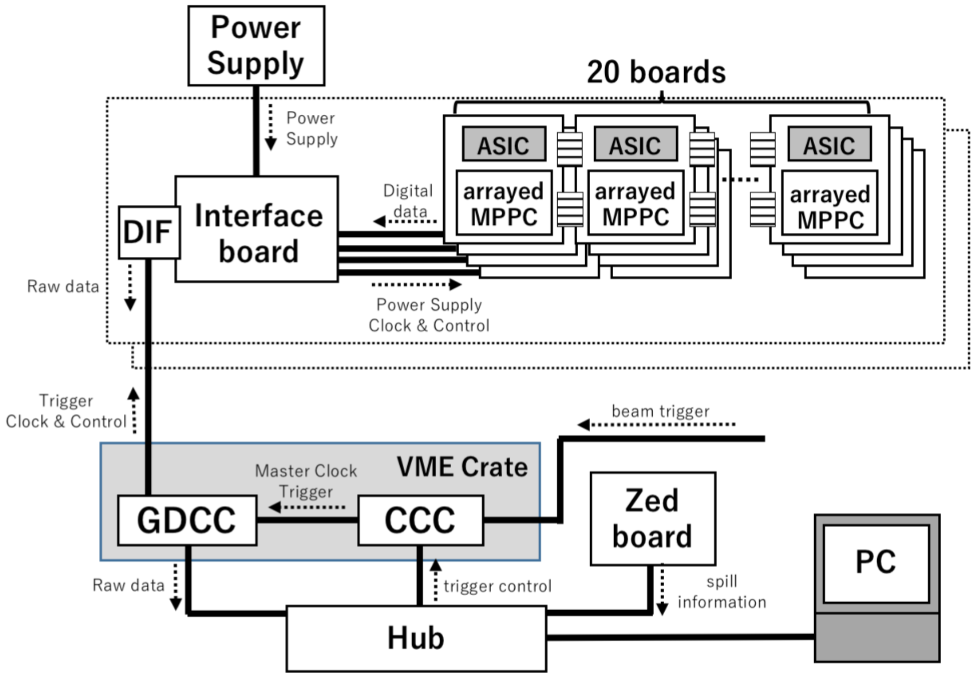

Figure 4.2: The schematic view of WAGSCI readout and data acquisition

Figure 4.3: Picture of Active Sensor Unit board (ASU).

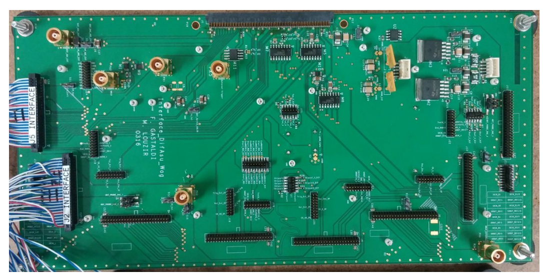

Figure 4.4: Picture of Interface board (IF)

Table 4.1: The number of front-end and back-end boards used for Water Module.

Board type	required number for a side	total number
ASU	20	40
IF	1	2
DIF	1	2
GDCC	1	1
CCC	1	1

Figure 4.5: Picture of Detector Interface board (DIF).

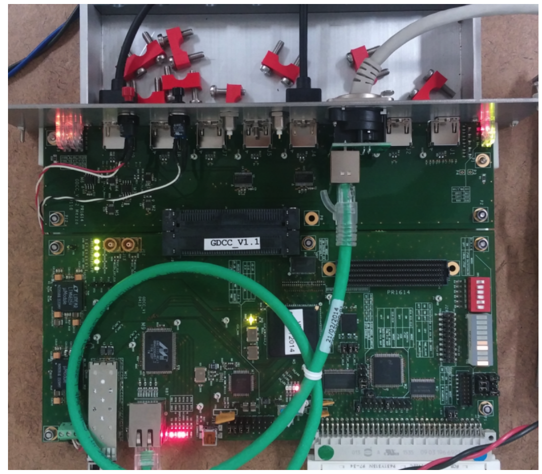

Figure 4.6: Picture of Giga Data Concentrator Card (GDCC)

4.2.2 SPIROC2

SPIROC2 has been developed to satisfy requirements such as large dynamic range, low noise, high precision and large number of readout channels. Figure 4.7 shows the block diagram of the analog parts for a channel in SPIROC2. SPIROC2 has identical 36 analogue processing circuit and can control bias voltage by 8-bit InputDAC, gain by 6-bit variable capacitor and threshold by 4-bit threshold adjustment for 36 channels independently. SPIROC2 has 16-deep analogue memory and it enables multi-hit data acquisition with one gate. Timing information is converted to charge referring to TDC ramp and charge and timing information is converted to digital data with 12-bit Wilkinson ADC.

Figure 4.8 shows the block diagram of the digital parts in SPIROC2. All systems of SPIROC2 are synchronized with bunch crossing clock[1]. At the timing of bunch crossing clocks, charge and timing information are stored in the analog memory and saved in the current data column. The number of counter of bunch crossing clock, called bunch crossing ID(BCID) is also stored in BCID registers. When the edge of bunch crossing counter clock is detected and OR of 36 channels is on, the data column moves to the next at the same time for all 36 channels. The schematic of data storage system is shown in Fig. 4.9. TDC ramp goes up and down in response to bunch crossing clock as shown in Fig. 4.10. The slope of ramp is fixed so the hit timing is uniquely converted from time to voltage. The converted hit timing is digitalized with the AD converter. Using BCID and TDC information, hit timing from the start of spill is calculated. When acquisition gate is closed or all 16-deep analogue memory gets full, AD conversion starts and and transportation out of the chip and reset of analogue memories starts sequentially.

4.2.3 Link between DAQ and SPIROC

Sequence of phases on the digital parts in SPIROC is controlled by signals from DAQ. SPIROC provides response signals for DAQ. Signals sent from DAQ to SPIROC are start acquisition, start conversion, and start readout, as well as reset and clocks. Signals from SPIROC to DAQ are chip saturation and end readout. Figure 4.11 shows the schematic of the DAQ signals for each case with all the 16-deep memory full or not full. The DAQ signals control the process in the following order.

[1]SPIROC2 has been developed for International Linear Collider so the clock is named as "bunch crossing".

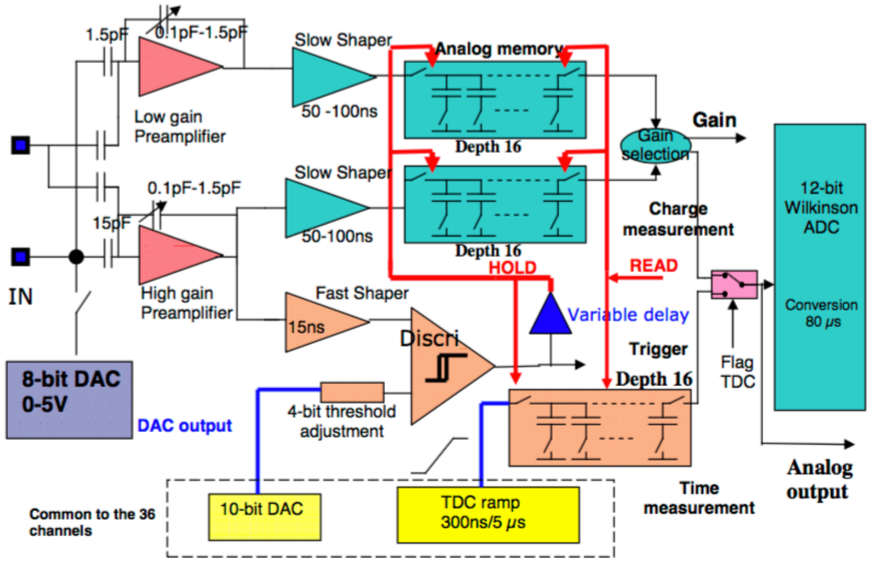

Figure 4.7: Block diagram of analogue part of SPIROC2

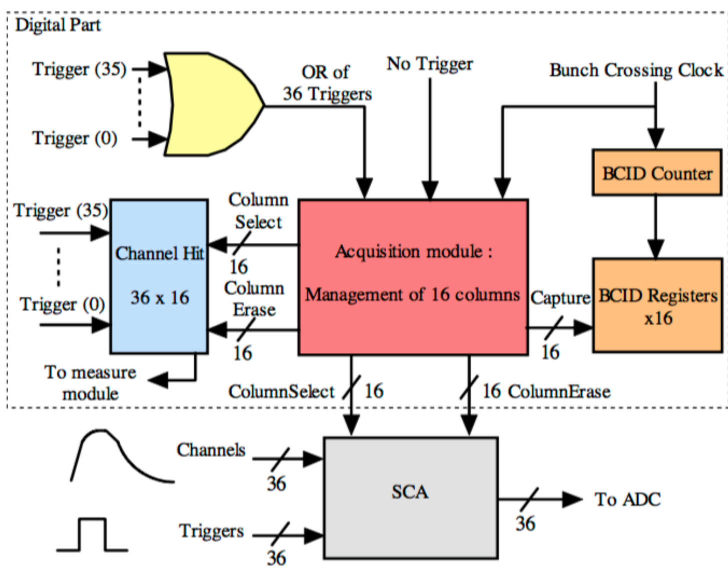

Figure 4.8: Block diagram of digital part of SPIROC2

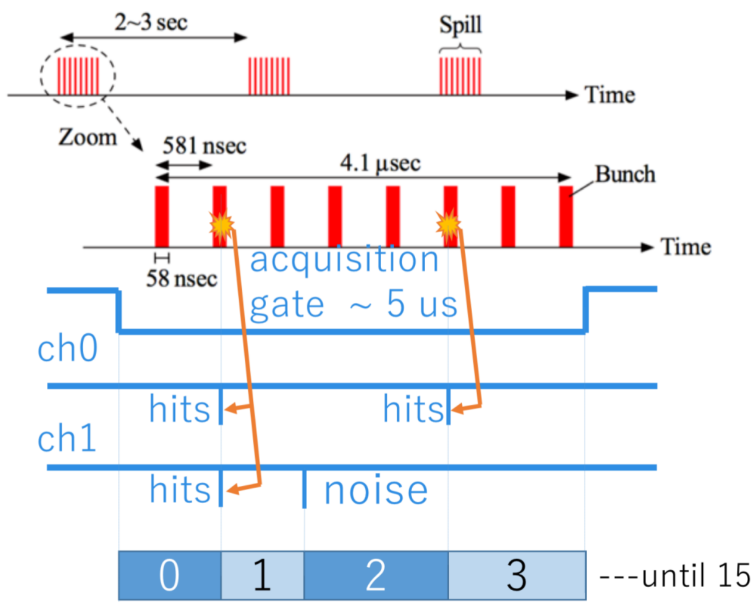

Figure 4.9: Schematic of data storage system

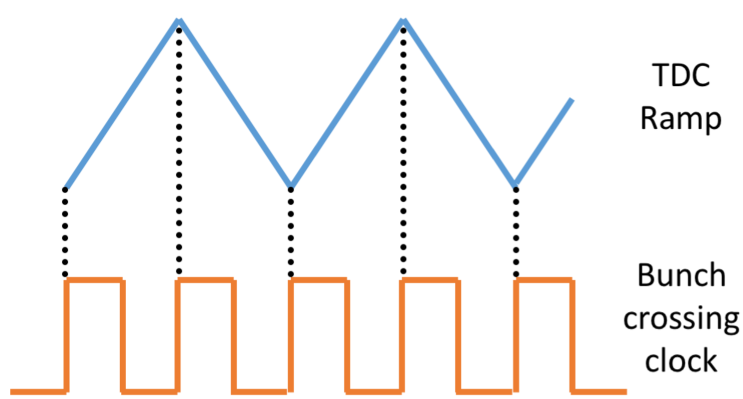

Figure 4.10: Schematic of TDC ramp.

1. Reset
   All the digital parts are reset first.

2. Start acquisition
   The acquisition phase starts and is maintained during this signal.

3. Chip saturation
   When 16-deep memory gets full, the acquisition phase finishes and then the conversion phase starts. When the memory does not get full while the acquisition gate is open, the acquisition phase ends at the timing that acquisition gate is closed and the chip saturation signal is induced to start the conversion phase.

4. Start conversion

5. Start readout. As the conversion phase ends with the trailing edge of the chip saturation signal, the readout phase starts with the start readout signal. The data bitstream is readout with the frequency of bunch crossing clock in serial. It depends on the frequency of bunch crossing clock and data size, but it takes at most 11ms to readout the data of a chip.

6. End readout

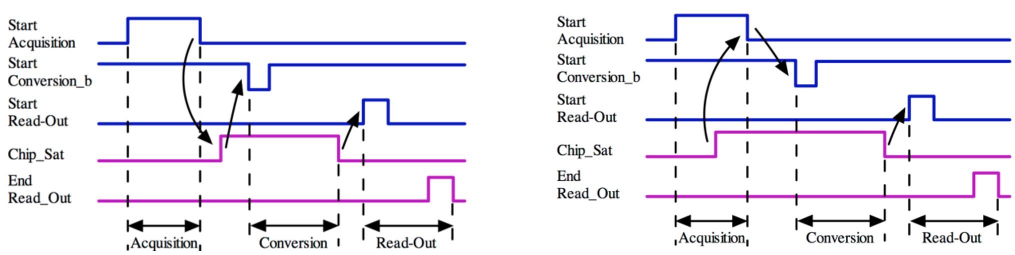

Figure 4.11: Schematic of the DAQ signals in case that the chip does not get full(left) and in case that the chip gets full (Right).

Synchronization of signals sent from DAQ to SPIROC for start acquisition is shown in Fig. 4.12. Start acquisition gate gets open at the edge of 50MHz master clock just after external acquisition gate comes. Bunch crossing clock, which is generated by counting master clock, starts at the same time as start acquisition gate gets open. DAQ valid trigger which starts acquisition gets open at the edge of bunch crossing clock. Bunch crossing counter and TDC ramp start at the same time. Due to the gap between external acquisition gate and master clock, there is 20ns jitter in absolute timing measurement.

Each ASU board is connected with two 50-conductor flat cables and a DAQ signal is transported along a corresponding line of the cable. Figure 4.13 shows the schematic of connection of boards and transported signal. Interface board has 4 connecting ports. In Fig. 4.13, 5 ASU boards are serially connected to a connecting port and the total number of connected ASU boards is 20. Each 5 ASU boards are apparently connected in parallel, but actually they configure a daisy chain and a DAQ signal from DIF board is transported thorough the daisy chain. The chips are identified by the order in the daisy chain.

4.2.4 Data structure

SPIROC2 data stream is shown in Fig. 4.14. The charge and time information converted by a 12-bit Wilkinson ADC are stored with 1-bit hit information and 1-bit gain select information. In order to

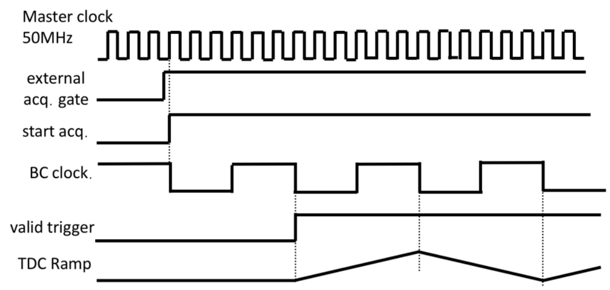

Figure 4.12: Schematic of link between DAQ and SPIROC.

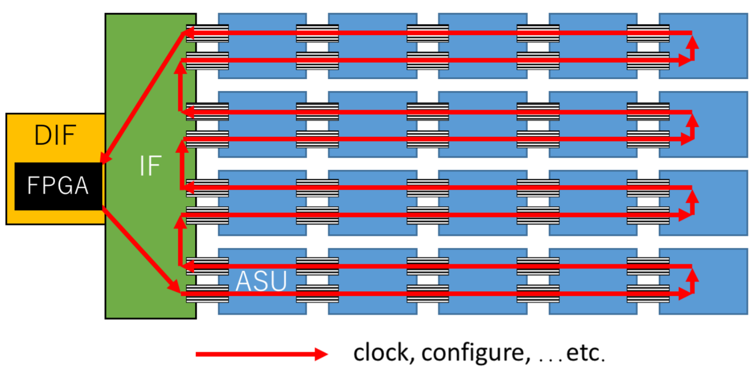

Figure 4.13: Schematic of ASU daisy chain.

acquire charge information with large dynamic range and to save the data size, SPIROC2 adopts two different magnification preamplifier, high gain preamplifier and low gain preamplifier, and the switch of them which enables automatic shift from high gain to low gain when the amplitude of signal is very high. 1-bit gain select information is the flag of this switch. 1-bit hit information indicates whether the signal of the corresponding channel is triggered by the threshold or not. The charge and time information are stored 36-channels together and bunch crossing ID follows it. In the end of data stream, chipID is stored.

SPIROC2 data stream is packaged chip by chip with the DIF header and trailer including 8-bit DIF identifying chipID, which is different from chipID of SPIROC2. The chip data stream is packaged with the GDCC header and trailer including 32-bit GDCC counting acquisition gate number. Above of all, the beam trigger information which contains lower 16-bit beam trigger number information and 8-bit trigger mode are stored . The highest bit of 8-bit trigger mode indicates the acquisition gate is generated by external trigger or internal periodic trigger.

4.3 Test measurement of the prototype board

The test measurement of the prototype front-end board based on SPIROC2D is done. The purpose of test measurement is to understand the behavior of the board, improve it and confirm the board satisfies experiment requirement. In the measurement, second and later prototype board with SPIROC2D are tested.

The first test for first prototype front-end board with the two different types of the chip, SPIROC2B/2D had been done in 2015[29]. SPIROC2B is the first generation of SPIROC and SPIROC2D is the third generation of SPIROC. SPIROC2B has some bugs and they are modified in SPIROC2D. SPIROC2D is adopted in WAGASCI experiment for the first time so this is the first application of SPIROC2D to the experiment. In the measurement of the first prototype board with SPIROC2B/2D, it was confirmed that the first prototype board with SPIROC2B worked but prototype board with SPIROC2D failed to read out signal from MPPC and modification of prototype board with SPIROC2D was needed. In this section, test measurement for the updated prototype board is described.

The test for first prototype board with SPIROC2D in 2015 confirmed the connection between ground and chip, which had been needed in case of SPIROC2B, made the state of chip very unstable. In the second and later prototype board, this connection is removed and it is confirmed that the chip state gets stable. The measurement with a board and an arrayed MPPC, and test of chain connection with multi boards is the main topic of this section.

One of the known issues is that the reference of the comparator in SPIROC2D is wrong as shown in Fig. 4.15. Due to this issue, it is only possible to set the discriminator threshold at undershoot. It may make measurement very sensitive to electronics noise. This issue occurs not on a mounting board but on a ASIC chip, so it is difficult to fix this issue. It is one of most important tests to confirm the effect of wrong position of comparator.

4.3.1 Setup

The test setup is shown in Fig. 4.16. An ASU board with an arrayed MPPC is placed in a dark box together with an interface board. In the dark box, LED and an attenuator board same as the one used in chapter 3 are equipped. The external gate trigger is generated by a function generator and it is sent to CCC and the other function generator as the gate trigger. The other function generator generates bunch structure trigger for LED. The frequency of external gate trigger is set to 10Hz. The period of bunch is set to 4us. Light from LED is injected to 32-channel MPPC and the intensity can be controlled by changing width and height of pulse. Synchronization of each trigger is one of the problems to measure TDC resolution. The main source of asynchronous is the accuracy of a function

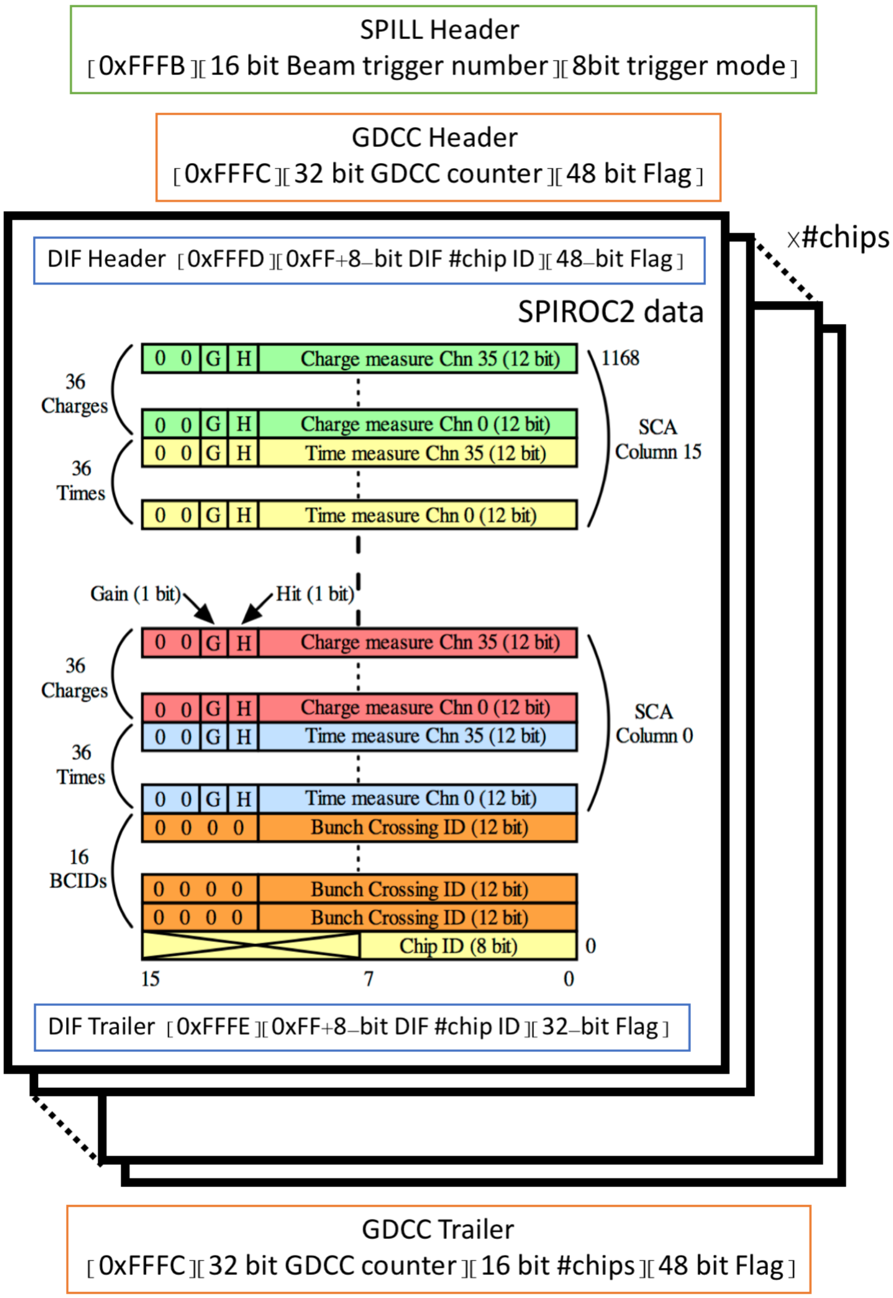

Figure 4.14: SPIROC2 data structure.

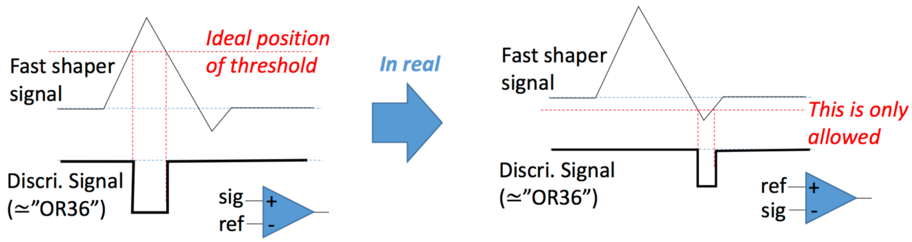

Figure 4.15: Wrong position of comparator of SPIROC2D. It forces to set the discriminator threshold at undershoot.

generator and it makes about 10ns inaccuracy of light generation time. The value of supplied HV is fixed at 56.0V. The fine tuning of HV is done by inputDAC. In this measurement, an arrayed MPPC of which breakdown voltage of all 32 channels is around 52.0V is used. The inputDAC can control HV in the range from -2.5V to 0.0V, so the operating voltage of MPPC can be controlled in the range from 1.5V to 4.0V.

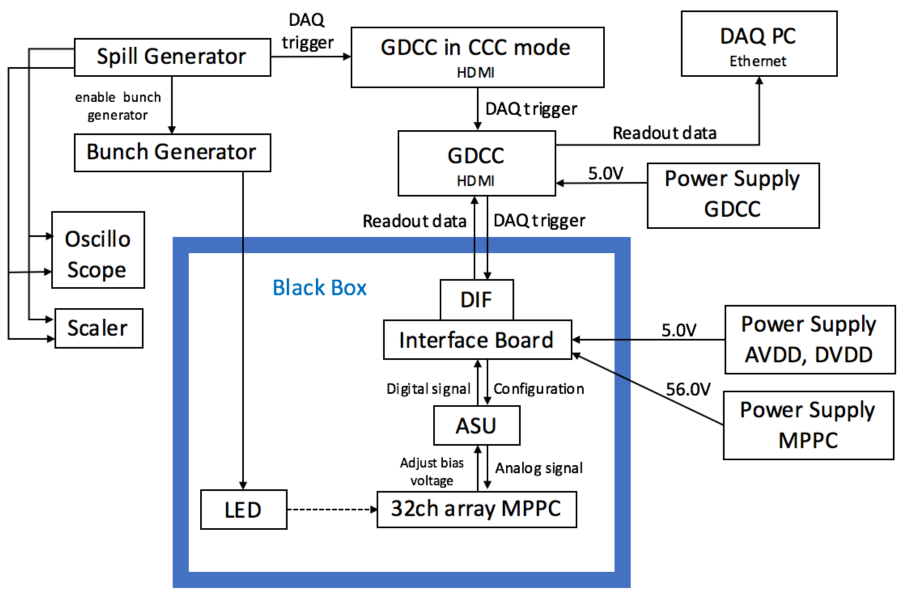

Figure 4.16: Schematic of link between DAQ and SPIROC.

4.3.2 Threshold problem

In order to confirm the effect of wrong position of comparator, MPPC dark noise rate is scanned with changing threshold. The measurement is done without LED light and with only a ASU board and a interface board.

SPIROC does not have a counter, so dark noise rate is measured by using BCID data. Figure 4.17 shows the typical plot of BCID of dark noise. Dark noise arises randomly, so the number of entry of each bin basically becomes equal, but the tail of curve is seen because acquisition gate is closed when

16-deep analogue memory gets full. The noise rate is calculated as following equation:

$$Noise\ rate = \frac{A}{A+N} * \frac{1}{T}, \tag{4.1}$$

where A is the number of entry of a bin obtained by fitting plateau range of BCID with constant, N is the number of total acquisition gates and T is the time corresponding to a BCID bin, which was 400ns this time. The equation takes multi dark noise hits in a BCID bin into account. For example, in case of Fig. 4.17, A=30.5 events, N=28725 events and T=400ns, so noise rate is calculated at 2.6kHz. By this method, the measurement of noise rate is limited up to 2-3 MHz depending on the period of bunch crossing clock. However, it makes no problem on the measurement of MPPC noise rate because it is confirmed that MPPC dark noise rate is less than 1MHz.

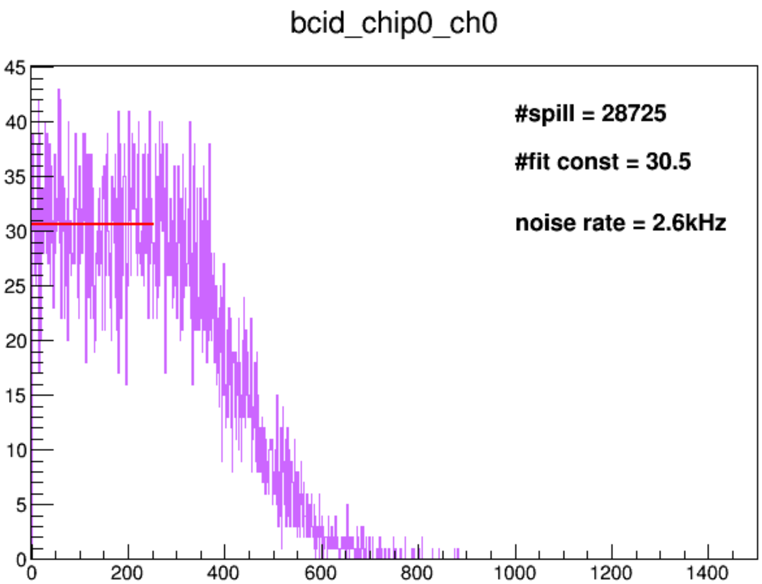

Figure 4.17: BCID plot and fitting for one of 32 channels. X axis is BCID and Y axis is the number of entry. This plot shows the plot when threshold is set to 2p.e. equivalent level.

Figure 4.18 shows the result of the scanning using above method with two different over voltage, 2.3V and 3.1V. The gain with ΔV =3.1V is about 1.35 times more than that with ΔV =2.3V. The typical curve of MPPC noise rate which has some plateau ranges is seen. Each plateau range corresponds the threshold range for each photo electron equivalent level and plateau ranges from 1p.e. to 3p.e. are clearly seen. It means that threshold can be set from 1p.e. although position of comparator is wrong. However, the position and width of plateau range especially of 2p.e. and 3p.e. are different between two operating voltage as expected. It means that the precise tuning of threshold according the gain is needed.

4.3.3 BCID distribution

After checking threshold, the readout of BCID information is tested with LED light injection. Threshold is set to 1.5 p.e. equivalent level and only a channel is open. The LED light is injected with the bunches of which frequency is 250kHz and that of spill is 10Hz. In other words, LED light is injected every 10 BCIDs.

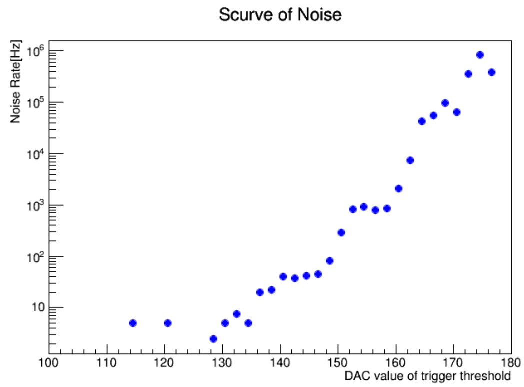

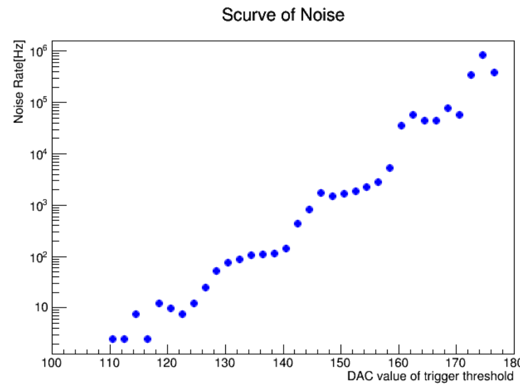

Figure 4.18: Scurve of noise rate with operating voltage 2.3V(left), 3.1V(right). X axis is the DAC value of threshold and Y axis is the noise rate.

Figure 4.19 shows BCID distribution and Fig. 4.20 shows the difference between measured BCID and expected BCID. 89.1% of all events comes in the expected BCID, but 4.3% comes before expected and 7.6% comes after expected. It is over expected 10ns inaccuracy of LED light injection timing.

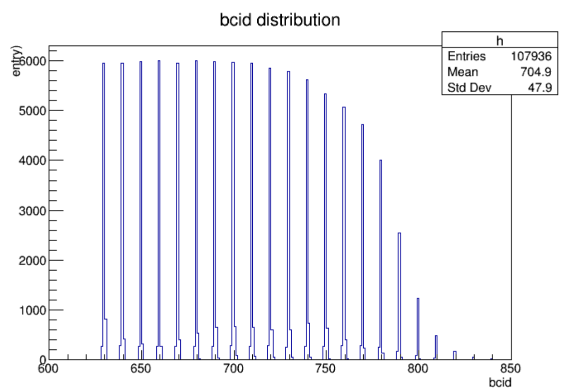

Figure 4.19: BCID distribution with LED light injection. Threshold is set to 1.5 p.e. equivalent level.

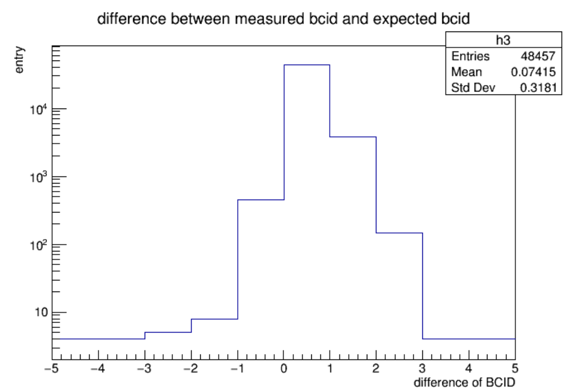

Figure 4.20: The difference between expected BCID and measured BCID. Negative value means measured event comes before expected timing. The flat distribution is the background due to MPPC dark noise.

The issues that events before expected timing is because timing synchronization between bunch crossing clock and external acquisition trigger is not going well. Bunch crossing clock is generated by counting 50MHz master clock. When the counter gets 2N where N is the constant integer, the bunch crossing clock of which period is 20*2N ns is generated. Synchronization between bunch crossing clock and external acquisition gate is done by reseting the counter to 0 when external gate trigger comes. Unfortunately, the reset does not work well now, so the time difference between the timing of rising edge of bunch crossing clock and start acquisition is randomly distributed from 0ns to 20*(2N-1) ns. Also, there is 20ns jitter between timing of start acquisition and that of external gate trigger due to the gap between external acquisition gate and master clock. These make uncertainty of the gap between timing of external gate trigger and the leading edge of bunch crossing clock. In this measurement, the period of bunch crossing clock is set to 400ns (N=10).

The issues that events after expected timing is because threshold is sensitive to ringing signal due to wrong position of comparator as shown in Fig. 4.21. Ringing of signal is not irregular phenomena, but it is not triggered in regular case because threshold can be set at higher level than ground enough to neglect ringing. But in case of SPIROC2D, threshold must be set near ground and shaping time is around 100ns, so ringing effect appears. Figure 4.22 shows ADC distribution according to difference between measured and expected BCID. Almost all the events after expected timing comes under the threshold, so it is confirmed that the events after expected timing is mostly due to ringing effect. Some comes over threshold and it is due to MPPC dark noise or afterglow of LED light. Figure 4.23 shows the dependence of ringing effect on threshold. As expected, it is clear that the ringing effect strongly depends on threshold. Especially in case that threshold is set at 0.5 p.e. equivalent level, the ringing effect is severe although fake hits due to ringing effects can be mostly neglected by the selection that ADC count is over threshold. It is because 16-deep analogue memory gets full and acquisition gate is closed before 8th of neutrino beam bunches comes due to high MPPC noise rate and its fake hits. So the measurement with 0.5 p.e. threshold is not realistic. In case that threshold is set at 1.5 p.e. equivalent level, fake hits are made in the probability of about one-tenth so fake hits is not negligible but its effect is small enough for neutrino beam measurement because neutrino event rate and background event rate is low enough even if the intensity of neutrino beam gets more strong. In case that threshold is set at 2.5 p.e. or higher equivalent level, the probability that fake hits are made is less than 0.5% and the effect of fake hits is negligible.

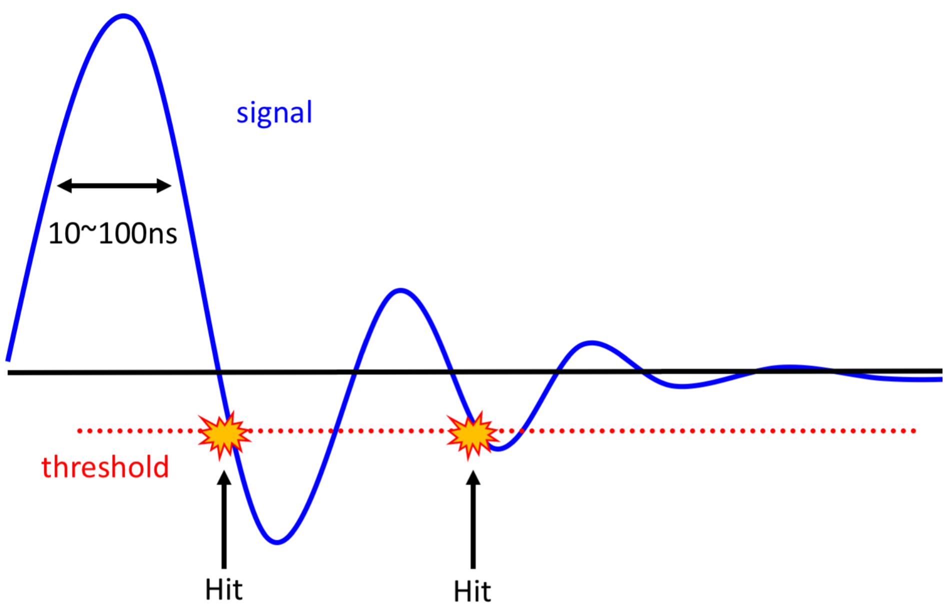

Figure 4.21: A schematic of ringing effect.

4.3.4 ADC distribution

After checking BCID, the readout of ADC information is tested. The test setup is same as the setup for BCID measurement. Figure 4.24 shows the ADC distribution. Each photo electron peak are observed clearly. Strange distribution below threshold comes from fake hits due to the ringing effect.

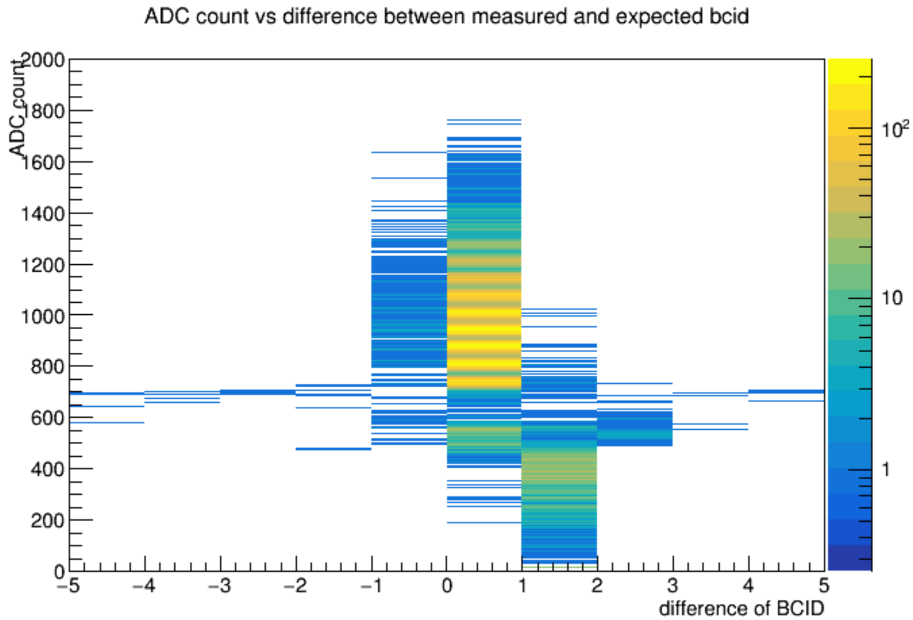

Figure 4.22: ADC distribution according to the difference between measured and expected BCID. X axis is difference of BCID and positive value means measured events comes after expected timing. Y axis is ADC distribution according to each differences of BCID.

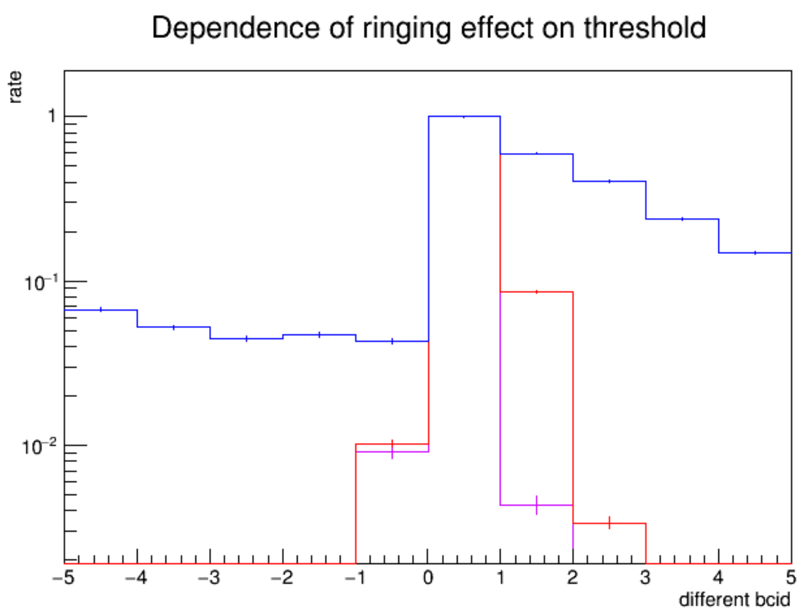

Figure 4.23: The difference between expected BCID and measured BCID. Positive value means measured event comes after expected timing. The threshold of each line is different. Blue line is for data taken with 0.5 p.e. equivalent threshold and red line with 1.5 p.e. and violet line with 2.5 p.e.

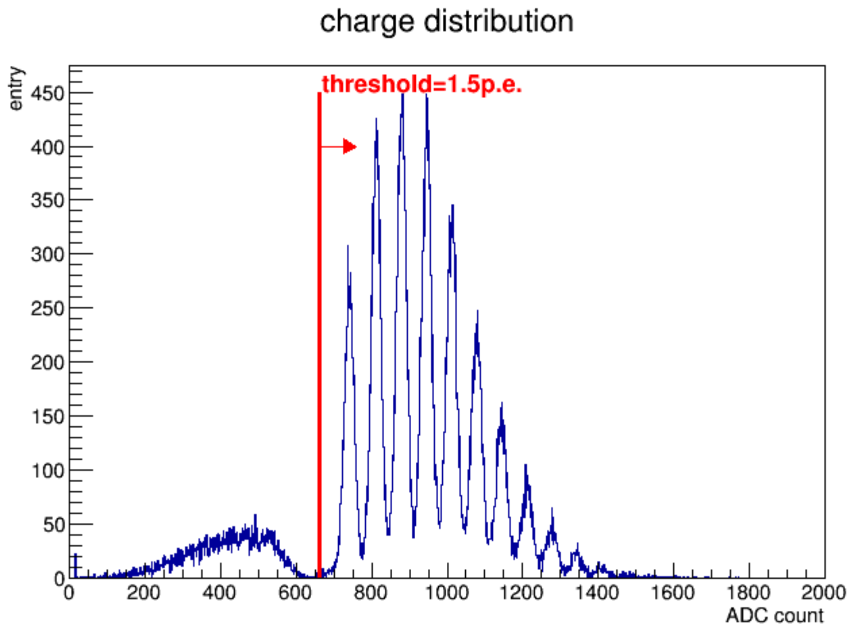

Figure 4.24: ADC distribution with LED light injection. Threshold is set to 1.5 p.e. equivalent level.

ADC distribution of each analogue memory is shown in Fig. 4.25. Except 10th and 14th memory, photo electron peaks are clearly seen like Fig. 4.24, but no peak other than pedestal is seen in 10th and 14th memory. On investigation, it is revealed that 10th and 14th memory recover by adjusting the reset signal, which is sent from DIF in order to initialize analogue memory. Figure 4.26 shows the charge distribution of each memory after the modification. In all memories including 10th and 14th, photo electron peaks are clearly seen. The difference of MPPC gain and intensity of LED light are due to difference of setup.

Stability of gain and pedestal among 16-deep analogue memory is also checked. Gain is calculated by measuring the distance of two neighboring peaks same as Eq.3.3 as shown in Fig. 4.27. Pedestal is calculated by extrapolating 0 p.e. equivalent ADC count as shown in Fig. 4.28. Figure 4.29 shows gain and pedestal of each analogue memory. Gain is stable among 16 memories and standard deviation is less than 1% of mean value. In contrast, pedestal is not so stable among 16 memories and standard deviation is about 20% of mean value of gain. It is due to the individual difference of 16 analogue memories, so it is corrected when ADC count is converted to photo electron. ADC count is converted to photo electron as following equation.

$$photo\ electron = \frac{(ADCcount) - (pedestal)}{Gain} \tag{4.2}$$

The converted photo electron distribution is shown in Fig. 4.30. It is clearly seen that each peak of 16 memories comes same position and the pedestal correction is well done. And it is confirmed that the strange distribution seen in Fig. 4.24 is below ground.

Gain linearity is also checked. Figure 4.31 shows ADC counts of peak position according to the number of photo electrons and Fig. 4.32 shows two neighboring peak distance according to the number of photo electrons. Gain linearity is sufficient and the each of two peak neighboring distance is in 10% range of mean value.

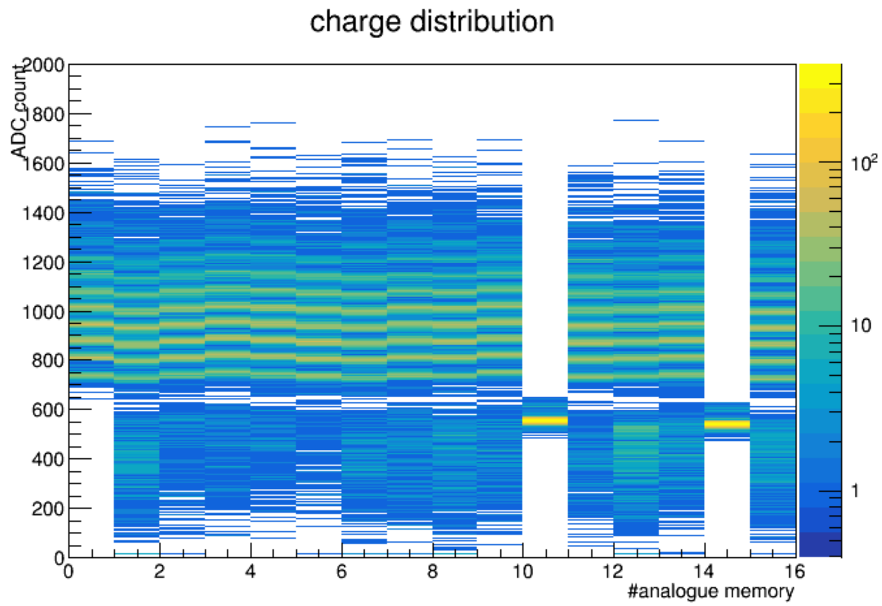

Figure 4.25: ADC distribution of each memory with LED light injection. X axis is the number of analogue memories and Y axis is the ADC distribution of each memory.

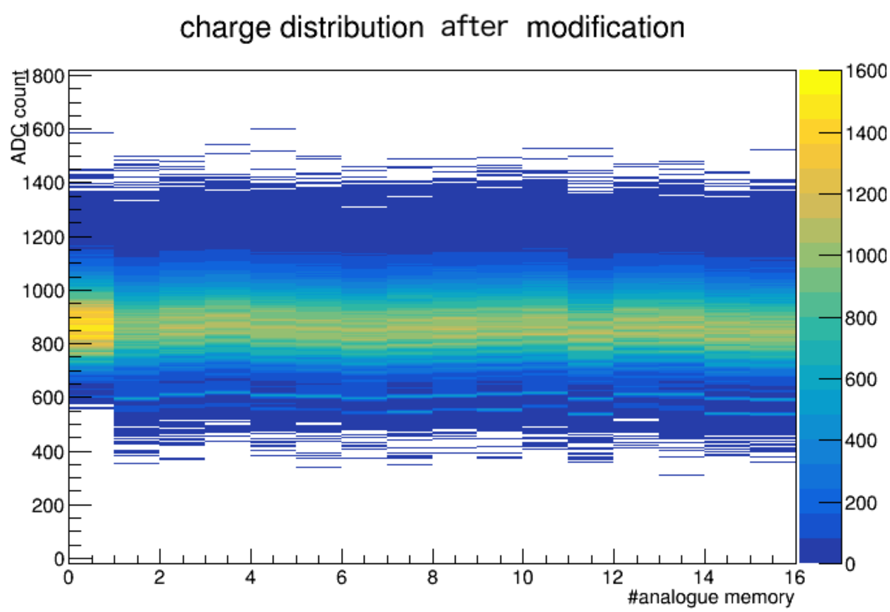

Figure 4.26: ADC distribution of each memory with LED light injection. X axis is the number of analogue memories and Y axis is the ADC distribution of each memory.

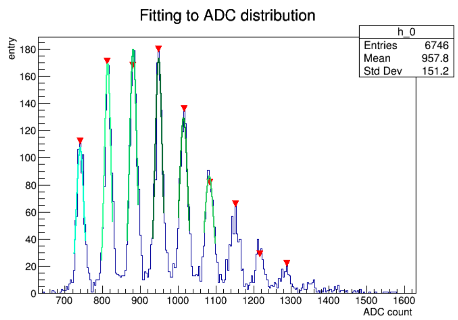

Figure 4.27: Fitting of charge distribution. Each peak is fitted by gaussian.

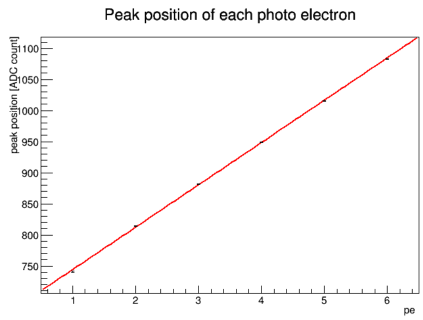

Figure 4.28: Linear fitting of mean peak position of each photo electron.

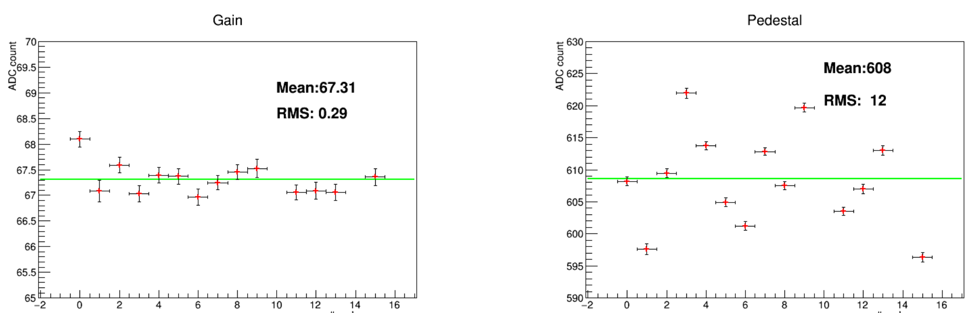

Figure 4.29: Gain(left) and pedestal(right) of each analogue memory. X axis is the number of analogue memories and Y axis is Gain(left) and Pedestal position(right).

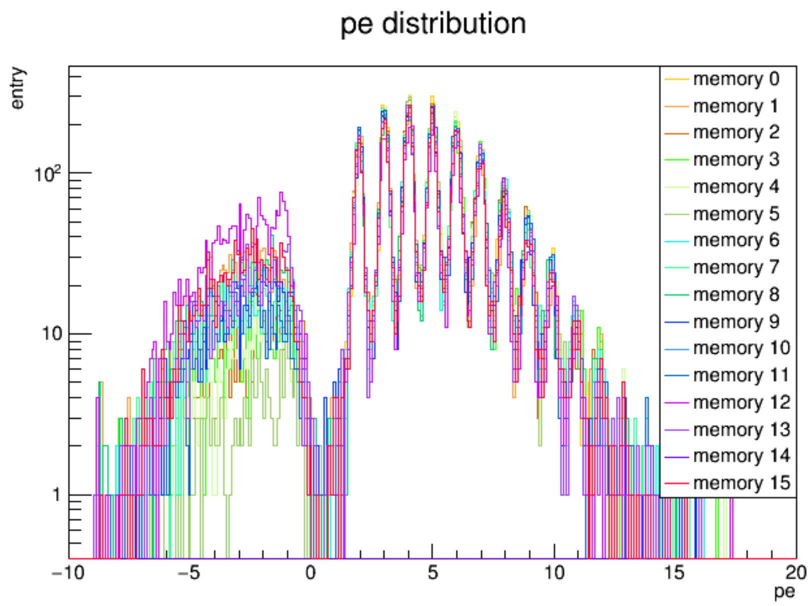

Figure 4.30: Photo electron distribution. Each histogram with different color is the p.e. distribution of different memory.

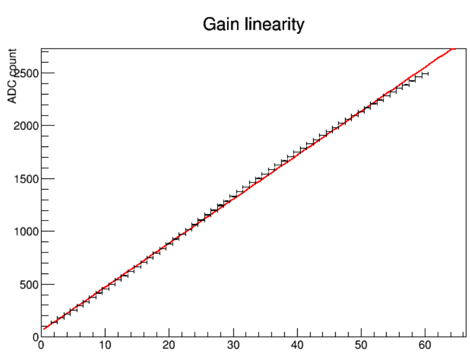

Figure 4.31: Gain linearity.

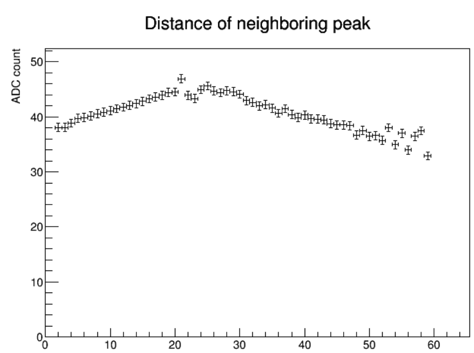

Figure 4.32: Two peak distance according to the number of photo electrons.

4.3.5 TDC distribution

Because timing synchronization between bunch crossing clock and external acquisition gate trigger is not going well, it is difficult to measure absolute hit timing as shown in Fig. 4.33. However, the uncertainty due to asynchronous of bunch crossing clock does not affect on the relative hit timing, so relative hit timing time is evaluated.

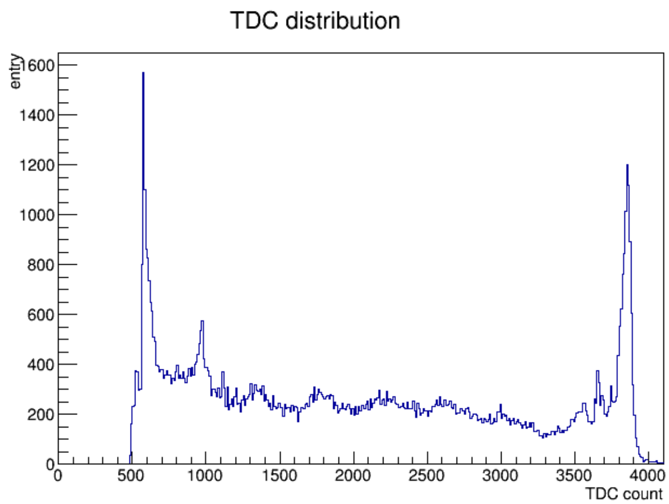

Figure 4.33: Absolute TDC distribution. The edges of distribution correspond either start point of TDC ramp and end point. The slope of ramp is fixed on the scale 1bin 100ps.

For the evaluation of TDC, the data taken with the LED light of which frequency is 250kHz is used. For cutting off noise and fake hit, the events which go out from expected BCID and of which charge are below threshold are rejected. The relative hit timing is calculated by comparing a hit timing with that of reference channel. LED light is injected every 4μs, so it is expected that all hits are in expected timing in accuracy of LED light injection, about 10ns. Not only for cutting off noise and fake hits but also for cutting off time walk effect, charge of reference channel is cut in certain range as shown in Fig. 4.34. Then, the hit timing in selected range is defined as expected timing. The relative hit timing is calculated by subtracting expected hit timing from measured one, so negative value means the event is observed earlier than expected timing. Figure 4.35 shows the result of relative hit timing measurement, where charge of measured events is cut off in the same range as reference for neglecting time walk effect. Almost all events are in expected timing in accuracy of LED light injection,10ns. Some of them distributes a bit wider than expected, but it is expected due to the afterglow of LED light.

Time walk is also measured. Figure 4.36 shows correlation between relative hit timing and normalized charge. Normalized charge is calculated by subtracting pedestal position from charge information. It is clearly seen that hit timing is strongly correlated with charge and the time walk between small charge and large charge is about 40ns.

Figure 4.37 shows the function of time walk according to charge which is obtained by fitting Fig. 4.36. Pedestal is also subtracted. Minus value means signal is triggered faster than expected timing. In regular case, hit timing of small charge is slower and that of large charge is stable due to high magnification of amplifier. However, in case of SPIROC2D, it is totally different due to the wrong position of comparator. In contrast, hit timing of small charge is faster than expected timing and that of large charge is not stable but strongly correlates with charge because the high

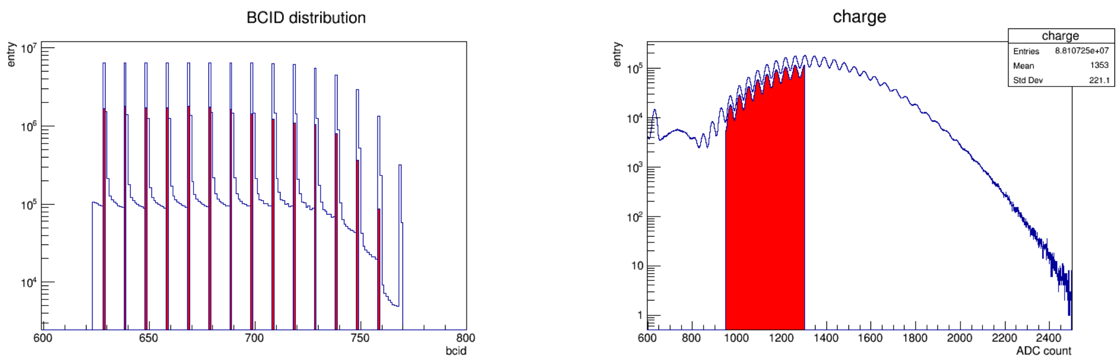

Figure 4.34: Cut of BCID(left) and charge(right) distribution for reference channel. Red area is used one as the reference.

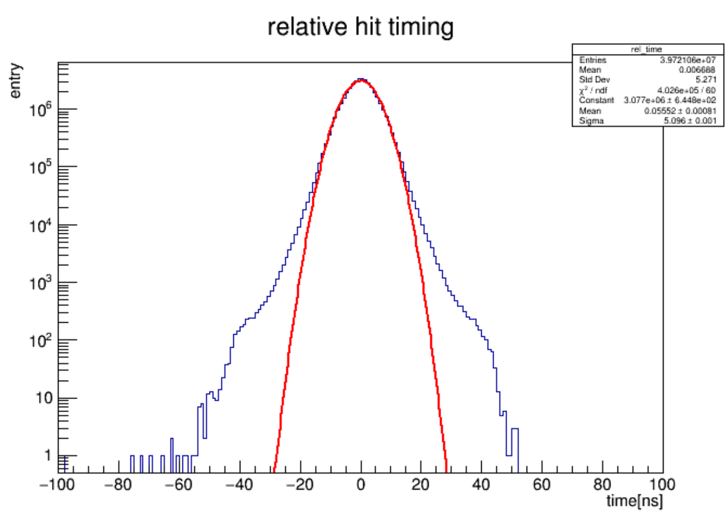

Figure 4.35: Relative hit timing. Red line is the gaussian fitting.

magnification of amplifier is no use. Hit timing is corrected following this function, but this correction has 5ns uncertainty. It is not significant for time clustering, but is likely to effect correction TOF measurement.

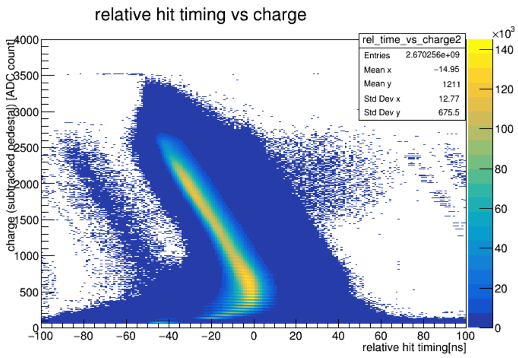

Figure 4.36: Correlation between hit timing and charge. X axis is relative hit timing. Y axis is charge. Pedestal is subtracted from charge.

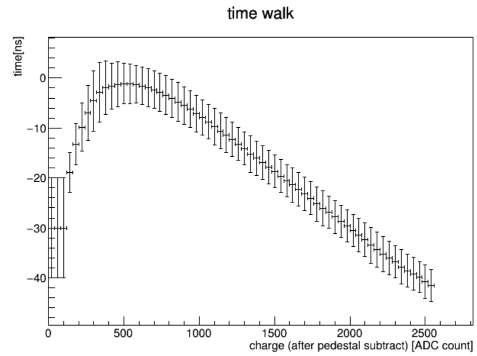

Figure 4.37: Function of time walk according to charge. Pedestal is subtracted from charge. X axis is charge and Y axis is hit timing.

4.3.6 Operation test with several boards

As the first measurement with multi front-end boards, the operation test is done with 4 prototype boards. In order to check that boards configure daisy chain correctly, the test is done with 4 cases as shown in Fig. 4.38. In case A and case C, all boards correctly load the configuration and can readout MPPC signal. In case B, a downstream board can not load the configuration and not readout MPPC signal. In case D, two downstream boards can not load the configuration and not readout MPPC signal. It is due to the design of a prototype ASU board and a line for DAQ signal is wrongly connected. By cutting a corresponding signal line and connecting it with the correct one, it is confirmed that ASU boards correctly configure daisy chain. The design of boards is checked and all problems including about 16-deep analogue memory are fixed.

4.3.7 Summary

By a prototype board test, basic characteristic is tested and it is confirmed SPIROC2D has enough performance for WAGASCI experiment. It is confirmed that the wrong position of comparator effects on the measurement, especially in case of low threshold, but its effect gets sufficiently small by setting threshold over 1.5 p.e. equivalent level. Another problem about 16-deep analogue memory is found, and it can be fixed by adjusting reset signal.

4.4 Test measurement with mass production board

After fixing the problem on the prototype board, 46 ASU boards are produced as shown in 4.39. Firstly the board arrangement is checked by eye and then the operation check for all boards individually is performed with the same setup for prototype test measurement. In the operation check, an arrayed MPPC is used and the current for ASU boards and for MPPC is monitored. Also the behavior

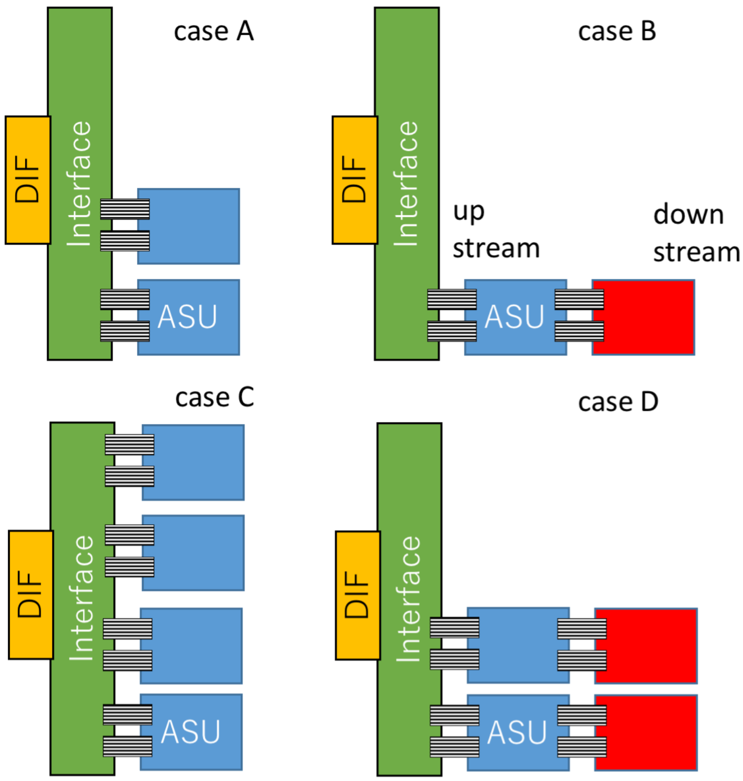

Figure 4.38: 4 configuration of test setup. Blue box is correctly configured ASU boards and red one is not correctly configured boards.

of 16-deep analogue memory, pedestal and trigger is checked by MPPC dark noise rate and ADC distribution. 44 of 46 products works correctly, but the other 2 products does not work due to the over current. It is expected that a short circuit is accidentally made while production and over current is observed. The two boards are rejected as bad samples.

Figure 4.39: Production of all 46 ASU boards.

4.4.1 Operation test with full setup

After operation check of all boards, operation test with full setup is done. Figure 4.40 shows the measurement setup. The measurement is done in the same place as the detectors installed and temperature is stable at 20 degrees. 20 ASU boards, 1 interface board and 1 DIF board are required to readout of each side of tracking planes. There are two side so the total required number is double. All boards and MPPCs are placed in a dark box. Each ASU board is connected with two 50-conductor 10cm flat cables and four most upstream ASU boards are connected to interface board with two 20cm flat cables. DIF is directly attached with interface board and it is connected with GDCC by 10.5m HDMI cable. The HV supply modules are set outside of black box and bias voltage is supplied with coaxial cable. It is difficult to prepare LED because the size of dark box is too large to get uniform light, so operation is tested by MPPC dark noise only.

In order to check operation with full setup, the daisy chain configuration is firstly tested. The test is done by increasing the number of ASU boards one by one. Up to about 10 boards, the daisy chain is correctly configured but it gets broken around 10 boards. After several tests with different configuration, it is revealed it is due to the attenuation and reflection of bunch crossing clock. A DAQ signal including bunch crossing clock is serially transported through daisy chain so the transportation length depends on the number of connected ASU boards. Also, the capacitance of daisy chain depends on the number of connected ASU boards. It makes the mismatch of impedance and DAQ signal is affected. Most DAQ signals are not so affected but the daisy chain line of bunch crossing clock is strongly affected. DAQ is synchronized to bunch crossing clock so it is critical issue.

This problem is fixed by making a patch to bunch crossing clock line. To prevent the attenuation of bunch crossing clock and match impedance, 4ch buffer, CDCLVC1104[28], is applied to bunch crossing clock line as shown in Fig. 4.41. The buffer is high performance and fast response one. The delay is 0.8-2ns, which is less than 1% of the period of bunch crossing clock, so the effect on the timing of

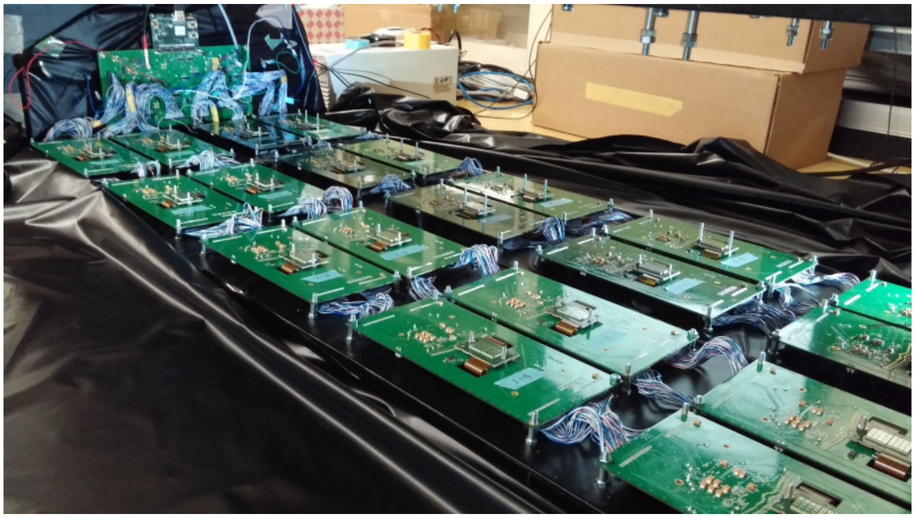

Figure 4.40: Setup for operation test with full setup.

bunch crossing clock is negligible. This patch works fine and daisy chain is configured correctly with full setup.

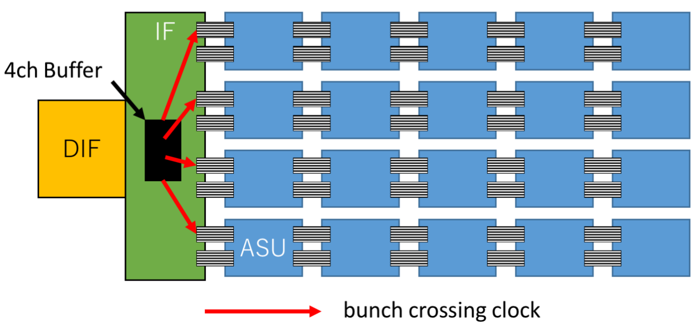

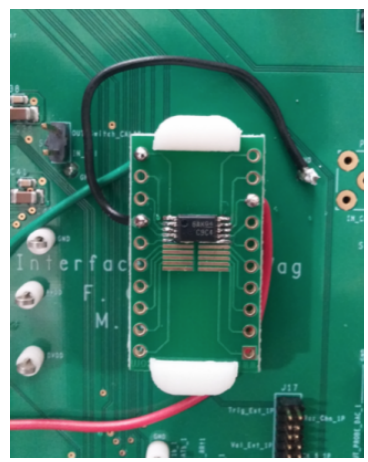

Figure 4.41: Schematic view of patch for bunch crossing line(left) and used 4ch buffer(right).

4.4.2 Gain and threshold tuning

After daisy chain problem is solved and operation check with full setup, gain and threshold with 40 ASU boards have been tuned. Gain is tuned by changing bias voltage. SPIROC can control bias voltage of each 32 channel in range of -2.5V to 0.0V. However the breakdown voltage distributes the wide range as shown in Fig. 3.7 compared to adjustable range. So 40 arrayed MPPCs of which breakdown voltage of most 32 channels is in the range from 51.4 to 52.2 are selected. Figure 4.42 shows the breakdown voltage of selected MPPC when over voltage=3.0V.

MPPC gain and threshold for all 1280 channels are tuned to certain values. Referring photo electron distribution of prototype module and dynamic range of SPIROC2D, gain is set to 40 ADC

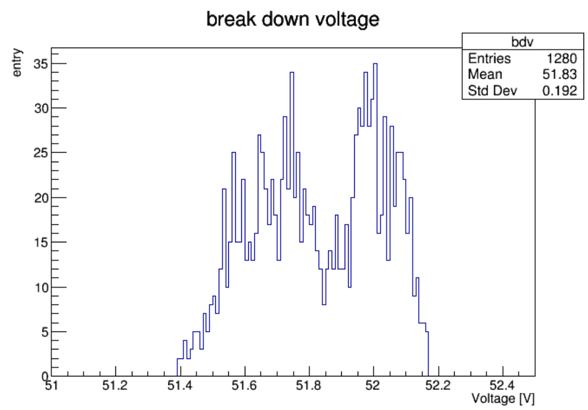

Figure 4.42: Breakdown voltage of selected 40 arrayed MPPC.

count, where charge up to 60 p.e. equivalent level is measured by high gain. Threshold is set to 2.5 p.e. equivalent level, where ringing effect and MPPC dark noise is negligible and signal is not cut.

Firstly, the correlation between inputDAC and threshold for 1 and 2 p.e. equivalent level is measured as shown in Fig. 4.43. Each center position of threshold value is calculated by scanning threshold with a inputDAC value. There is negligible correlation especially in case of 2 p.e. so threshold is optimized according to inputDAC.

It is also checked that global threshold can be applied to 32 channels at same p.e. equivalent level. Figure 4.44 shows the plateau range of threshold for 32 channels of a chip. It indicates the variation of plateau range among 32 channels is very small and all channel can be triggered at same photo electron equivalent level by a global threshold without fine tuning for each channel.

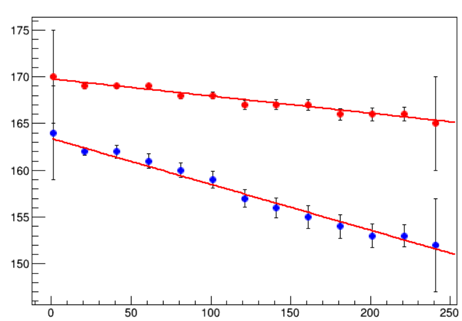

Figure 4.43: Correlation between inputDAC and threshold. X axis is inputDAC and Y axis is center position of threshold for 1 p.e. (Red) and 2 p.e. (Blue). Center position of threshold value is the center value of plateau of S-curve for each photo electron.

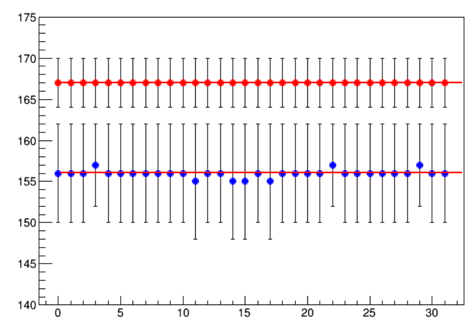

Figure 4.44: Plateau range of threshold for 32 channels of a chip. X axis is channel number and Y axis is threshold for 1 p.e. (Red) and 2 p.e. (Blue).

Secondly, the correlation between inputDAC and gain is measured. Gain is calculated by subtracting 1 p.e. peak position from 2 p.e. peak position. Figure 4.45 shows the correlation between inputDAC and gain for 32 channels and linear fitting for gain. The optimized inputDAC value is calculated by the result of fitting.

Thirdly, pedestal is measured after optimizing gain and threshold by extrapolating from 2p.e. peak position as shown in Fig. 4.46. Also, 3 p.e. equivalent threshold is measured by scanning threshold. Pedestal position and gain are recorded as the default value and they are used for checking data quality. Figure 4.47 shows the gain for all 1280 channels. Almost all channels is in the 10% range of mean value, but 32 channels of a chip is out of range. It is because the board is damaged and readout of signal does not work. The board is replaced to another one when electronics is installed.

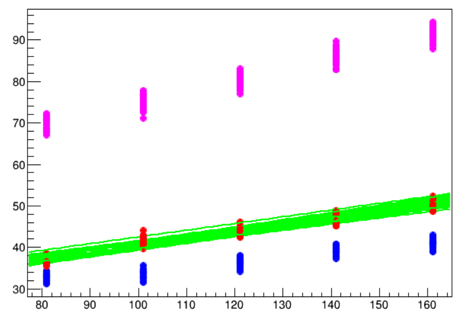

Figure 4.45: Correlation between inputDAC and gain. X axis is inputDAC and 10 inputDAC is corresponds to 0.1V. Y axis is gain. Violet point is gain for 2 p.e. and blue point is that for 1 p.e. and red point is gain.

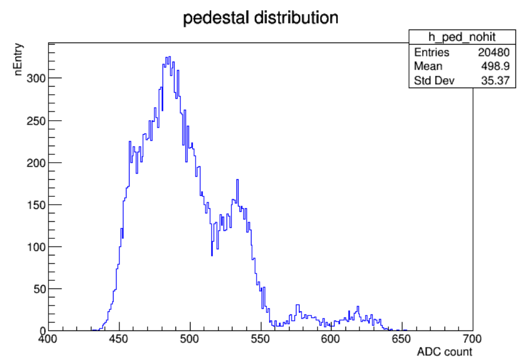

Figure 4.46: Pedestal position for 16-deep analogue memory of all 1280 channels.

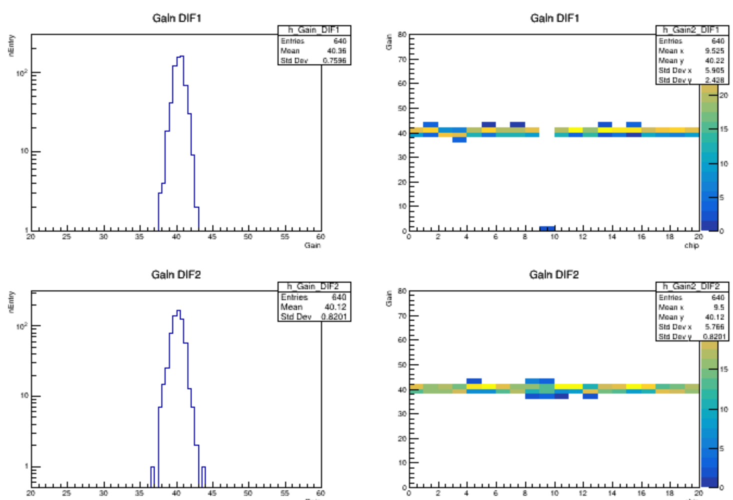

Figure 4.47: Gain of all 1280 channels.

4.5 Summary

A new electronics based on SPIROC2D has been developed. It is confirmed that a new electronics has sufficient performance. Some problems on ASU boards are fixed and 44 boards have been produced correctly. The daisy chain problem is also fixed and we succeed to operate the electronics with full setup. The tuning of threshold and gain is done. There is no problem on all boards and electronics is ready for installation.

However, the problem on timing synchronization between bunch crossing clock and acquisition gate has not solved yet. Timing synchronization is the problem on the DIF firmware and modification of DIF is difficult due to the lack of man power. So it is not modified in current setup and it makes the precision of hit timing measurement very worse. In current setup, hit timing measurement is enable only by BCID so the precision is hundreds micro second. If the problem is fixed, the hit timing measurement can be done with at least 10ns accuracy.

Chapter 5

Construction and installation

5.1 Construction

Water Module was constructed from October 2016 for 8 months in Neutrino Assembling Building in J-PARC. From October to November, the preparation for construction had been done. From December 2016 to February 2017, processing for scintillator bars had been done. Module assembling and evaluation had started in March 2017 and finished in June 2017. Construction process is listed as below.

1. Gluing wave length shifting fiber with optical cement
2. Painting reflector
3. Black spraying
4. Tracking plane assembling
5. Sub-module assembling
6. Module assembling and installation to the water tank

Figure 5.1 shows the process of gluing of optical cement in order to fix wave length shifting fiber to groove on the plane scintillator bars. For processing to 1280 scintillator bars with small individual difference, semi-auto system has been developed. In this system, a nozzle is moved along fixed route by two sliders automatically and optical cement and reflector is ejected from a nozzle by applying pressure while a nozzle is moving above wave length shifting fiber in the groove of a scintillator bar. A wave length shifting fiber and a scintillator bar are fixed on an aluminum plate by jigs and a plate is fixed on prescribed position of the stage. To reject air bubble inside optical cement and painting and fix a wave length shifting fiber on the groove of a scintillator bar sufficiently, optical cement and reflector are deformed with the vacuum chamber and the amount and proportion of them are optimized. After gluing and painting, scintillator bars are placed on a shelf with a plate and left for a day to dry optical cement and reflector. 25 scintillator bars are processed in a cycle for about 2 hours and 100 scintillator bars are processed in a day.

After processing gluing and painting, the scintillator bars are dismounted from the plate and checked whether there are air bubble or cracks on the fibers or not. The scintillator bars with bubble or crack are rejected in this phase. The good scintillator bars are sprayed by black painting as shown in Fig. 5.2. The scintillator bars are sprayed several times to avoid non-uniformity. Scintillator bars is immersed in water, so black spray insoluble in water is used.

Figure 5.1: The semi-auto process to gluing a wave length shifting fiber to a scintillator bar and to paint reflector.

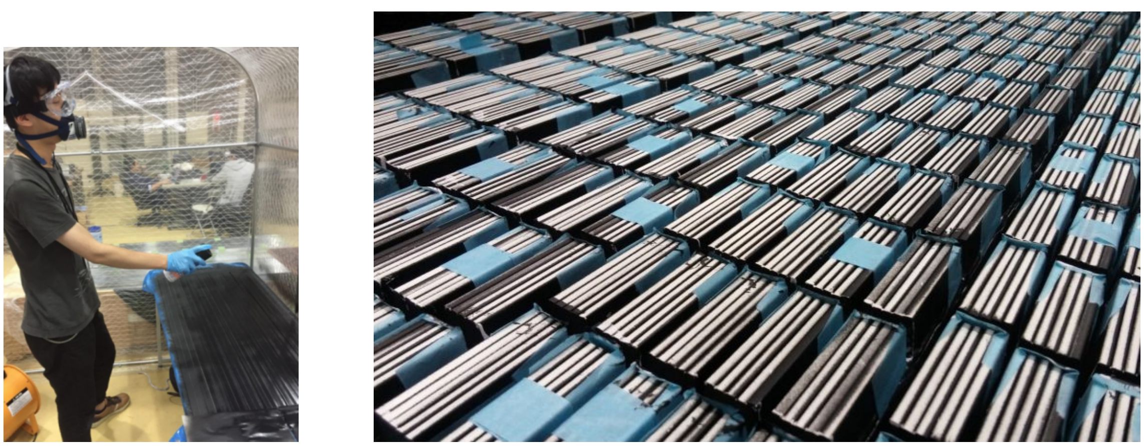

Figure 5.2: Black painting for scintillator bars.

After black painting, mass and volume measurement is done for confirming the density of scintillator bars. The mass is simply measured by a weighting scale and the mass measurement is done for all scintillator. The volume measurement is done for sampled scintillator bars. The volume is measured by putting a scintillator bar into a cylinder filled with water and measure the increased volume. Table.5.1 shows the mean and standard deviation of mass, volume and density. The deviation is so smaller than mean that individual difference of the density of the scintillator bars can be negligible.

Table 5.1: The table of mass, volume, density of parallel and grid scintillator bars

		mean	standard deviation	deviation/mean
grid	mass [g]	76.41	0.30	0.40%
	volume [cm^3]	70.44	0.25	0.35%
	density [g/cm^3]	1.084	0.002	0.27%
parallel	mass [g]	79.31	0.47	0.59%
	volume [cm^3]	73.41	0.23	0.31%
	density [g/cm^3]	1.080	0.004	0.44%

After black painting, light yield test had been done for 20% scintillator bars. Figure 5.3 shows the schematic of light yield measurement. Two measured scintillator bars were placed between trigger scintillator bars. In order to read out light from WLSF, an optical connector was fit at an edge of WLSF and was polished by hand. Light source was cosmic muon and a coincidence signal over 2.5 p.e. of two trigger scintillator bars becomes trigger. Light yield is defined as the mean of p.e. distribution. The result is shown in Fig. 5.4. The result is almost same between parallel and grid and mean of light yield is about 17 p.e. Light yield of 3 samples is lower than 10 p.e. It was due to the air bubble inside scintillator bars or the crack on the fiber. The same measurement was done for the other scintillator bars which had been processed in same cycle as low light yield bars, and none was lower than 10 p.e. These 3 samples were rejected as bad samples and the scintillators which had air bubble or crack were also rejected before assembling module.

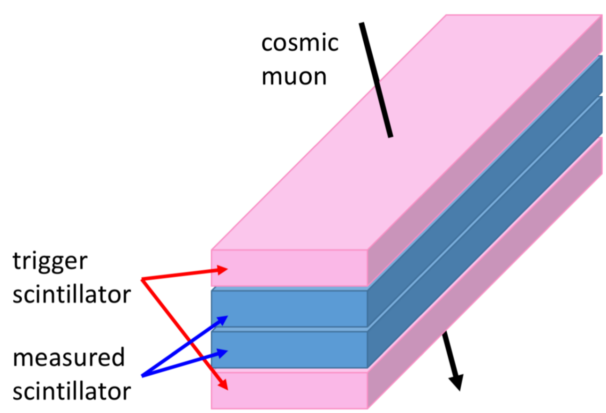

Figure 5.3: The schematic of light yield measurement

Unfortunately, it became clear that the width of slits of grid scintillator bars was not enough for assembling layer while testing layer construction, so grid scintillator bars were machined by a company in order to widen the slit from 3.5mm to 4.5 mm. After machining, mass, width of slits, and light yield were tested. Table.5.2 lists the measured difference of scintillator bars before and after widening the slits. It was confirmed that there were almost no difference in performance between before and after

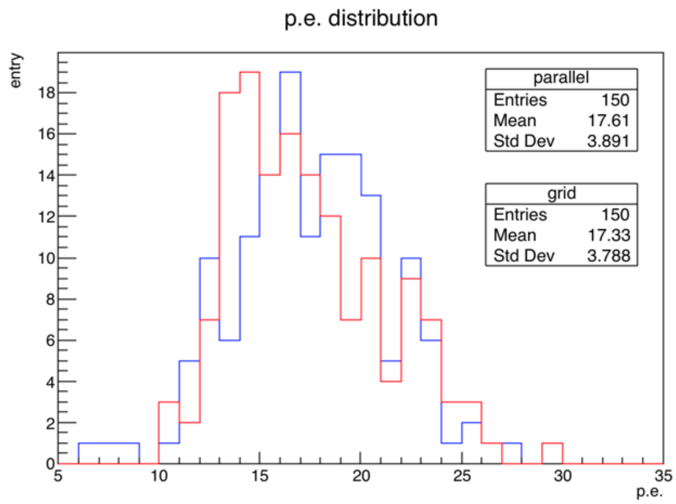

Figure 5.4: The result of light yield measurement of parallel scintillator bars(blue) and grid scintillator bars(red).

machining. It delayed construction schedule about 2 months.

Table 5.2: The difference before and after widening the slits of grid scintillator bars.

	before	after	difference
mass [g]	76.4	75.7	-0.7
width of slits [mm]	3.5	4.6	+1.1
volume [cm^3]	70.44	69.78	-0.66
density [g/cm^3]	1.084	1.084	0.0
light yield [p.e.]	17.33	17.18	0.15

Finally, 1500 scintillator bars, of which is 750 are parallel scintillators and the others are grid scintillator, are processed.

After process and evaluation of scintillator bars, module had been assembled in about two months. A tracking plane is assembled as shown in Fig. 5.5. A sub-module is composed of 4 tracking plane and assembled as shown in Fig. 5.6. The process of assembling is listed as below. Module assembling had gone without any problem except slit width and it finished on 22nd July as shown in Fig. 5.14.

1. Assemble tracking plane (Fig. 5.7)
2. Assemble four tracking planes into sub-module(Fig. 5.8)
3. Bundle wave length shifting fibers(Fig. 5.9)
4. Polish surface of fibers(Fig. 5.11)
5. Assemble four sub-module into a module(Fig. 5.12)
6. Install module to water tank(Fig. 5.13)

While sub-module assembling and after installation to water tank, light yield and channel mapping of each bundle had been tested by cosmic ray. Due to the delay of electronics, EASIROC is used

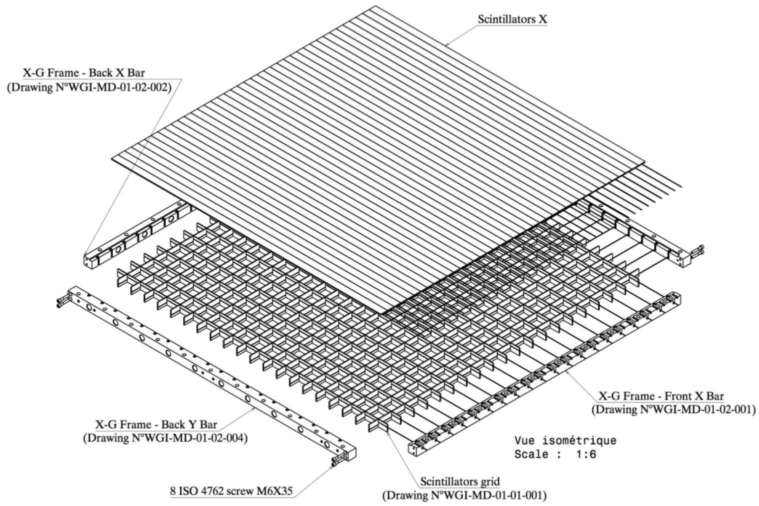

Figure 5.5: A tracking plane structure.

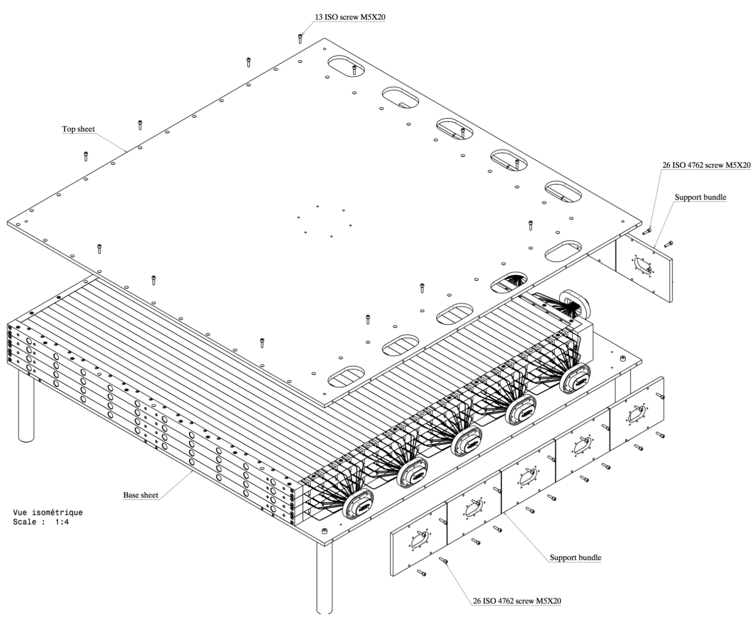

Figure 5.6: Submodule structure consisting of 4 tracking planes.

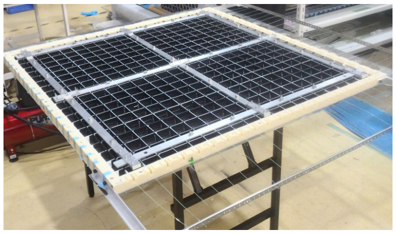

Figure 5.7: An assembled layer.

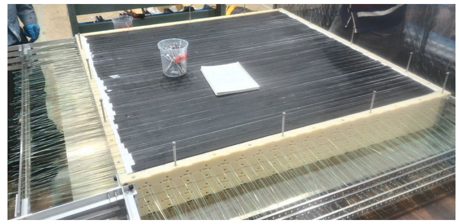

Figure 5.8: An assembled Sub-module.

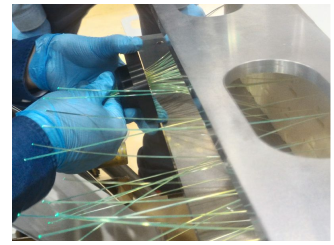

Figure 5.9: Bundle fibers into a cookie.

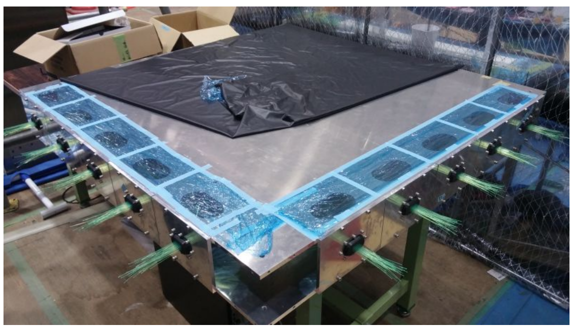

Figure 5.10: Sub-module after assembling.

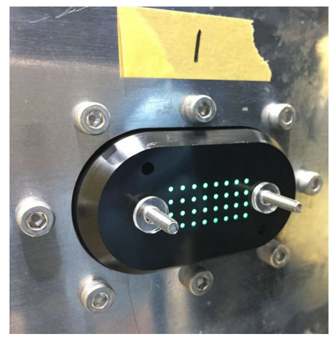

Figure 5.11: Surface of bundled WLSFs after polishing.

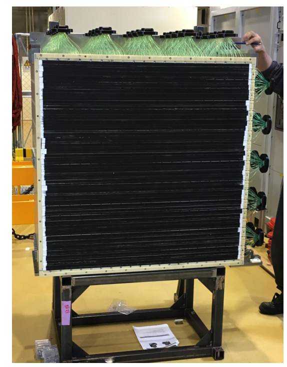

Figure 5.12: An assembled module.

Figure 5.13: Install a module to water tank.

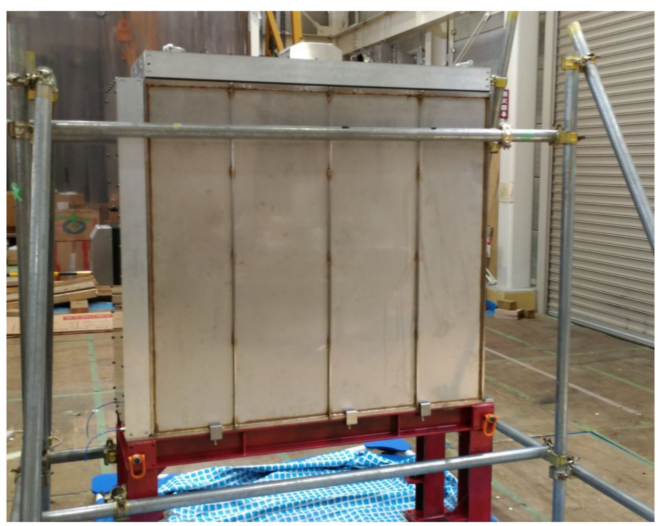

Figure 5.14: Completed module.

instead. Light yield is evaluated by calculating mean of photo electron distribution and the result for all 1280 channels is listed in Table.5.3. The channel of which light yield is less than 15 p.e. is defined as the bad channel and 3 bad channels has been found since sub-module assembling. It is confirmed by eye check that it is because the crack on the wave length shifting fiber. The difference of mean value between while sub-module assembling and after install to water tank is due to the direction of module.

Channel mapping is carefully checked while bundling fibers because wrong channel mapping makes strong tension on the fibers and such a fiber is likely to be broken. Also, channel mapping is quickly checked by watching event display of cosmic by eye.It is confirmed that all channels is in the correct position.

Table 5.3: The result of light yield measurement for all 1280 channels after construction.

		#channels	Mean	RMS	#bad channels
sub-module assembling	grid	640	28.2	3	2
	parallel	640	24.2	3	1
after install to water tank	grid	640	22.8	3.7	2
	parallel	640	26.9	3.5	1

5.2 Installation

Water Module was installed to 1.5° off-axis place in the middle of August together with Proton Module and INGRID module as shown in Fig. 5.15. The forward module is Proton Module, central module is Water Module and backward module is INGRID module.

Electronics was installed as shown in Fig. 5.19 in the beginning of September. Array MPPCs are firstly installed and MPPC light receiving surface are set and fixed to the position of wave length shifting fibers. Then ASU boards are installed and connected with each arrayed MPPC. Interface boards and DIF are also installed inside of electronics box. There are some connectors on electronics box and cables inside box can be connected with ones outside box through them. Electronics box is fixed to the water tank and rubber cushion is placed between them in order to avoid light leak. Electronics is covered with stainless plate and it become the darkroom inside it. In the case of water leak inside electronics box, a fine tube is set to the bottom of electronics box. It is designed not to leak light from there. A fan is equipped at the center of the cover of electronics box and it makes the temperature inside box constant. Also, temperature and humidity sensor is set inside electronics box and temperature and humidity is always monitored.

The gain and pedestal position is measured again after install of electronics for checking the effect of installation as shown in Fig. 5.16. The ratio of gain between before and after installation is shown in Fig. 5.17. The difference of gain for channels is less than 6% and the broken boards is recovered and the chip is also tuned well. The difference of pedestal position for a chip before and after installation is shown in Fig. 5.18. The difference of pedestal position is little, and it is confirmed that there is no effect of installation on electronics.

After evaluation of effect on installation, water was poured to Water Module in the middle of September for a week. Firstly, pure water is prepared. Water is filtered to remove impurities. After filtering, compound is added to water with the 0.25% ratio to water volume to avoid water corrosion. Water is left more than three days to remove air bubble inside water. Then, water is poured to the detector. When water is poured, the detector is leaned to remove air bubble inside cells. While the pouring, water flow is accumulated to calculate the amount of water inside tank.

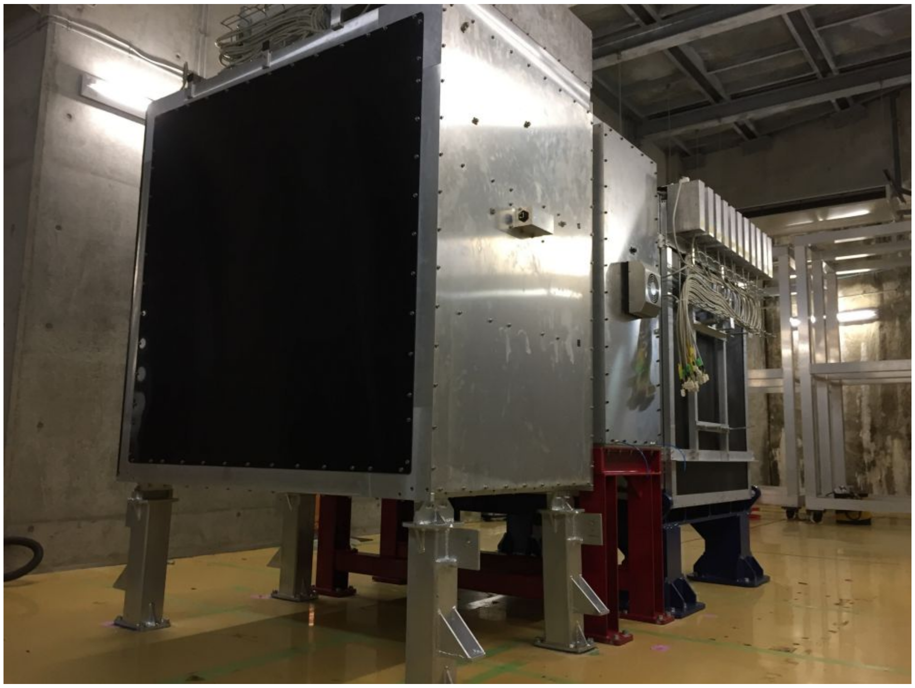

Figure 5.15: Picture of installed modules. Forward module is Proton Module, center one is Water Module and backward one is INGRID module.

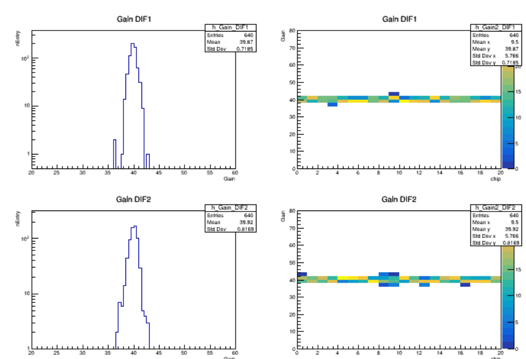

Figure 5.16: Gain of all 1280 channels after install.

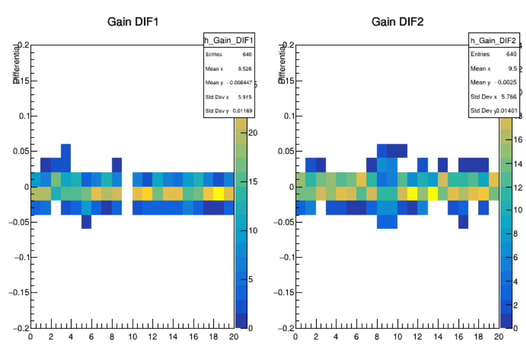

Figure 5.17: Ratio between gain between before and after install. X axis is the id of chip and Y axis is the ratio of gain.

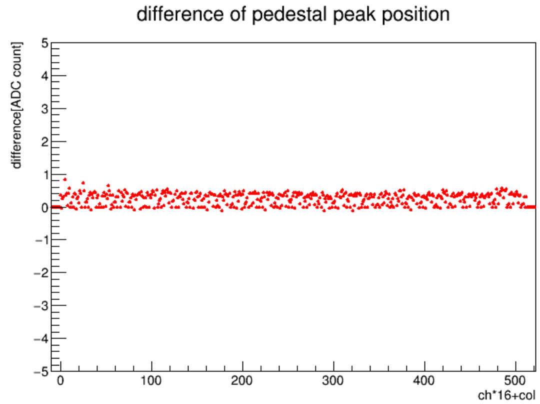

Figure 5.18: The difference of pedestal position of 16-deep memory of 32 channels of a chip before and after installation.

After pouring water and checking there was no water leakage, cable work was done. Figure 5.20 shows the module rack after cable work. GDCC, CCC, PCs and other modules are set a module rack. GDCC and CCC are mounted on VME crate and Zed board, NIM/TTL and ECL/TTL module are mounted on NIM crate. The modules are connected to PCs via a hub and they can be controlled remotely. Three PCs are prepared for WAGASCI experiment, and one is for data acquisition and control of electronics and one is for semi-offline analysis and data storage and the other is for remote access. The two former PCs are mounted on the rack and the other is set to a control room of NA building. The control of run and electronics can be done via the access PC except in case of emergency. All PCs are supplied power via uninterruptible power supply module and they are guaranteed safety in case of sudden power outage.

After cable work was done, monitor system and data acquisition system was checked for a week. All system got ready for neutrino beam measurement a week before neutrino beam started. Finally, neutrino beam measurement has started in October 15th.

Figure 5.19: Picture of installed electronics.

Figure 5.20: Picture of module rack

Chapter 6

Commissioning with cosmic ray

In this chapter, the result of commissioning is discussed. This chapter consists of three parts. Firstly, track reconstruction algorithm is explained. Secondly the stability of MPPC and electronics is discussed. Finally, detector performance is discussed using reconstructed events.

6.1 Data set

The analysis uses the cosmic data taken in September 2017. Because the electronics of WAGASCI does not prepare dedicated cosmic trigger[1], the cosmic data is taken by periodic trigger mode. In the periodic trigger mode, 5ms acquisition gate opens every 260ms. While gate is open, MPPC dark noise and accidentally coming cosmic ray are taken. Such a cosmic ray is used for analysis. The threshold is set to 2.5 p.e. equivalent level, where MPPC noise rate is small enough not to make 16-deep analogue memory full during 5ms acquisition.

The data set is from three periods. First period is from September 7th to September 8th. No water was filled in this period. Second period is from September 11th to September 15th. The detector was leaned and water was poured in this period. Third period is from September 22nd to September 30th. The detector stands up and the detector has been filled with water in this period. Installation work was going on in parallel to data taking, so it affects DAQ status and data quality.

6.2 Track reconstruction

For selection of charged particle events from hit information on Water Module, track reconstruction algorithm is developed. The reconstruction algorithm is based on INGRID, Proton Module [20] and prototype module[31]. This algorithm is improved for three-dimensional grid structure and for new electronics of Water Module. The reconstruction algorithm is under development. Here, the intermediate progress is described.

Figure 6.1 shows an event display of the cosmic event on Water Module. The left display is for YZ view and right one is for XZ view. Z direction is a direction parallel to beam axis and Y direction is a direction vertical to the surface of the ground and X direction is a direction perpendicular to Y and Z direction. YZ view is defined as side view and XZ is defined as top view.

The flow of the track reconstruction for Water Module is as follows: The detail of these selections is explained in this section.

1. BCID clustering

[1] It is due to the lack of man power. Technically, we can prepare cosmic trigger.

2. TDC clustering
3. Two-dimensional track reconstruction
4. Three-dimensional track matching
5. Veto and side-escape selection

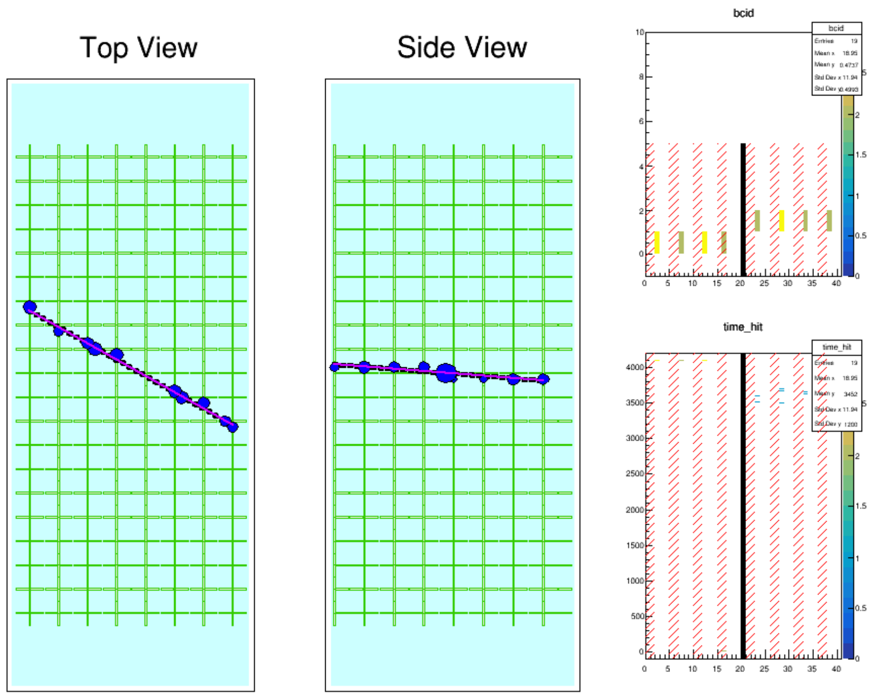

Figure 6.1: The event display of the cosmic event on the Water Module. The size of circle is according to measured photo electron. Blue circle is the hits which is used for track reconstruction.

6.2.1 BCID clustering

Channels of which signal is larger than 2.5 p.e. threshold are defined as hit. Each hit has ADC information, TDC information and BCID information. At first, hits are clustered according to BCID with the following criteria : If three or more hits are in either of side view or top view and they have same BCID, the BCID is defined as clustered BCID. Then, all the hits of which difference of BCID from clustered BCID is up to one are classified into a cluster. The difference of BCID of all hits from clustered BCID is shown in Fig. 6.2. Hits of which difference of BCID is more than 1 are distributed flat because they are due to noise. The hit of which difference of BCID is one is due to bad synchronization of bunch crossing clock so it is included in a cluster.

Unfortunately, mismatches of BCID between chips exist due to the wrong reset timing of bunch crossing clock. There are two mismatches. As shown in Fig. 4.41, bunch crossing clock is transported to ASU boards in four parallel line. First is a mismatch between two downstream ASU boards and

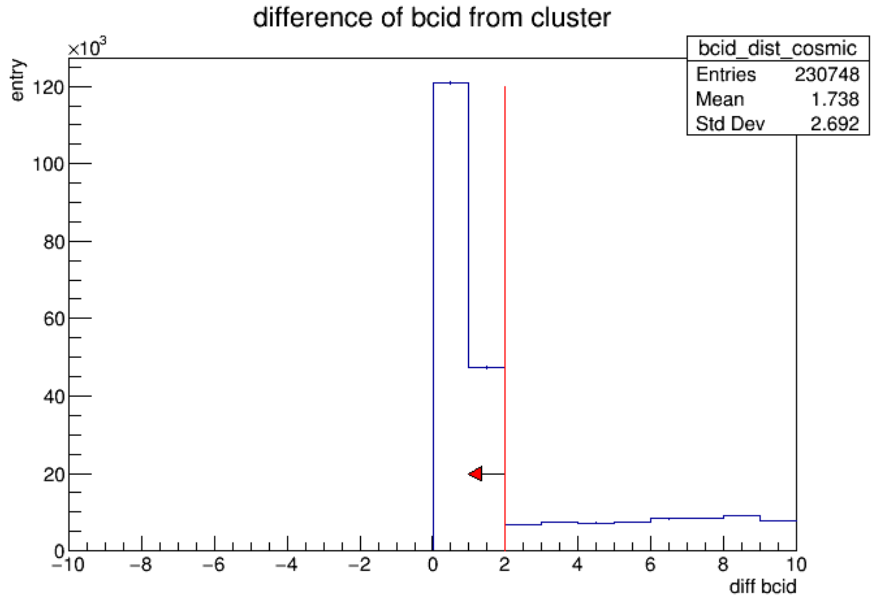

Figure 6.2: Difference of BCID of all hits from clustered BCID.

that of three upstream ASU boards in a line. The bunch crossing clock is transported to a line in serial so the transportation length depends on the partition of the chips. It makes the mismatch. It is confirmed the mismatch is always one so this mismatch is corrected in BCID clustering.

Second is a mismatch between top view and side view. The bunch crossing clock is generated in DIF and two DIF boards are used for each side. Now the reset of bunch crossing clock has problem so the two DIF is not correctly synchronized. It not always but sometimes makes a mismatch, which never gets more than one. So BCID clustering is firstly done view by view. When the difference of clustered BCID between two views is less than one, the hits included in clusters of two views become a cluster. If there is no corresponding cluster in a opposite view, such a cluster is rejected.

6.2.2 TDC clustering

The next step is TDC clustering but it is temporary omitted because of the bad synchronization of bunch crossing clock. It should be updated when DIF firmware is updated.

6.2.3 Two-dimensional track reconstruction

The next step is the reconstruction of 2D tracks, which are reconstructed independently in top view and side view. The track reconstruction algorithm is based on cellular automaton which has been used for track reconstruction in T2K. It is a discrete calculation model composed of many cell. The detail is described in Appendix A. This algorithm can reconstruct a track if there is at least three hits.

6.2.4 Three-dimensional track matching

After two-dimensional tracking, the pair of two-dimensional tracks in top view and side view is searched. Three-dimensional track matching is done with the following criteria : if difference of upstream point Z of side view track and top view track is smaller than six reconstruction planes, they are combined into a three-dimensional track. Here, the definition of reconstruction plane for along-z is used. If there is more than one candidates of two-dimensional track in opposite view, the pair of tracks with the smallest difference of upstream point Z is combined. If there is more than one pair of two-dimensional side view track and top view track which has the same difference of the upstream point Z, the pair of tracks which has the smallest difference of the downstream point Z is combined, and if it is also same, the pair of tracks which has the smallest difference of mean p.e. per hits is combined.

Figure 6.3-6.5 shows event displays of reconstructed track. Track is correctly reconstructed as shown in Fig. 6.3. However, sometimes charged particle runs the gap between tracking planes, track is not correctly reconstructed as shown in Fig. 6.4. Also, when there are many short tracks at a short distance, tracks are not correctly reconstructed as shown in Fig. 6.5.

It can be improved to optimize the two-dimensional reconstruction method. The source of problem is that vertex position is not determined in the step of two-dimensional reconstruction and that short track is mis-reconstructed. The following method can avoid these problems. The method is to reconstruct tracks again after searching vertex position in three-dimensional track matching. The produced particles in a neutrino interaction is concentrated to a single vertex so it constraints the start point of track. A long track is likely to be reconstructed correctly, so a vertex can be determined with a start point of a long track.

Currently, such a method is not taken, so multi-track events is likely not to be reconstructed correctly.

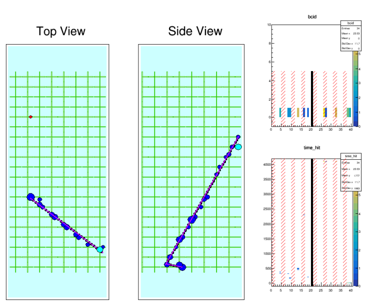

Figure 6.3: Correctly reconstructed tracks. A short track is also reconstructed correctly.

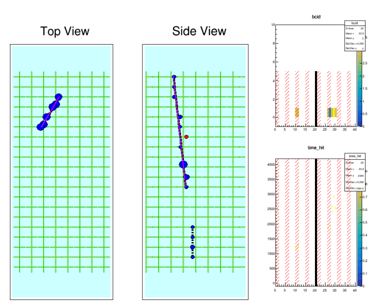

Figure 6.4: Charged particle run the gap between layers and reconstructed track is cut to two tracks.

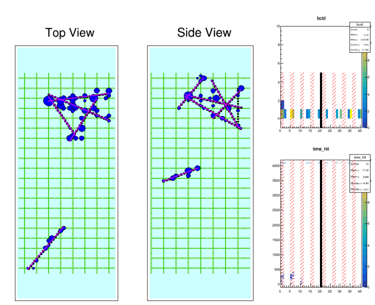

Figure 6.5: Many short tracks exist at a short distance and most of them can not be reconstructed.

6.3 Stability check

Secondly, the stability of the detector and electronics has been checked. The stability is monitored by checking gain, pedestal position, pedestal width, MPPC dark noise rate and light yield. It is monitored every 3 hours to accumulate sufficient statistics. Accumulated acquisition gate time is about a hundred seconds for 3 hours data acquisition. Dark noise rate with 3p.e. equivalent level is at least 10 Hz, so a thousand events of dark noise are expected.

The stability of gain is checked for monitoring MPPC stability. Gain is given from the mean position of 3 p.e. peak. Gain is calculated as following equation.

$$Gain = \frac{(Mean\ position\ of\ 3p.e.) - (pedestal)}{3} \tag{6.1}$$

Strictly speaking, the given gain is not same as one given by the past definition of gain, which is defined as the distance of two neighboring peak. However, the linearity of gain is guaranteed, so the given gain value can approximate the true gain value. The reason why we take this method is that the noise rate of 3 p.e. equivalent level and crosstalk rate is low. If the gain is given by fitting two peak distance, we need more statistics to measure gain with the same accuracy of this method. We want to monitor at least every 3 hours so this method is taken. However, this method highly depends on optimization of threshold. Sometimes 2 or 4 p.e. equivalent peak is wrongly fitted and gain value is measured lower or higher than the true value. In such a case, the raw ADC distribution is checked to confirm the gain is stable.

The stability of pedestal is checked for monitoring the electronics stability. Pedestal position and width is given by fitting pedestal with gaussian.

MPPC dark noise rate is also checked for monitoring MPPC stability and for monitoring electronics stability. Dark noise rate is calculated by the same method as the method written in section 4.3.2.

Light yield is checked for monitoring detector stability. Light yield is calculated by the mean of photo electron distribution of cosmic event.

- Gain
  Figure.6.6 shows the gain history in September. Tuning of gain and threshold is done on September 7th, and then data taking has been started. Gain was stable in first period but it got unstable on September 14th. It was because the light was leaked from the gap between the water tank and electronics housing. The water tank has been leaned in September 11th and the variation of the width of pedestal also has been seen in September 11th as shown in Fig. 6.8. So it was considered that the fixing of electronics housing was not sufficient and small gap was made while leaning water tank, and the gap gots wider while working of water pouring. After standing up water tank again, the electronics housing was fixed again and the connecting edge was covered by black tape. Tuning of gain and threshold was done again in September 21st and gain for all channels gathered, and it was confirmed that there was no light leak.

  In third period, most of channels were stable but some of them were out of 10% range. It was but because the temperature inside electronics housing changed as shown in Fig. 6.7. Operation test of fans attached on electronics housing has been started in September 22th just after tuning of gain finished. The temperature got about 2°C lower than before operation of fans, so the gain of MPPC changed. It also effected on the optimization of threshold and fitting of 3 p.e. peak was not going well. The tuning parameter was optimized again after the third period under the operation of fans.

- Pedestal
  Figure.6.8 shows the difference between pedestal mean position and default value and pedestal width history. The default value of pedestal mean position is defined as the pedestal peak position measured in tuning. In first and third period, pedestal was stable. The effect of light leak in second period was also seen in pedestal history. The pedestal position was stable and width of pedestal is smaller than gain enough to separate two peak positions, so electronics worked stably.

- Noise rate
  Figure.6.9 shows the stability of noise rate. Most of channel except a channel was stable in first period. Noise rate increased in second period due to light leak. Noise rate gets smaller in third period due to the temperature inside electronics housing gets lower. The result is consistent with stability of gain and stability of pedestal.

- Light yield
  Figure 6.10 shows the stability of light yield. Light yield is stable so the detector is stable.

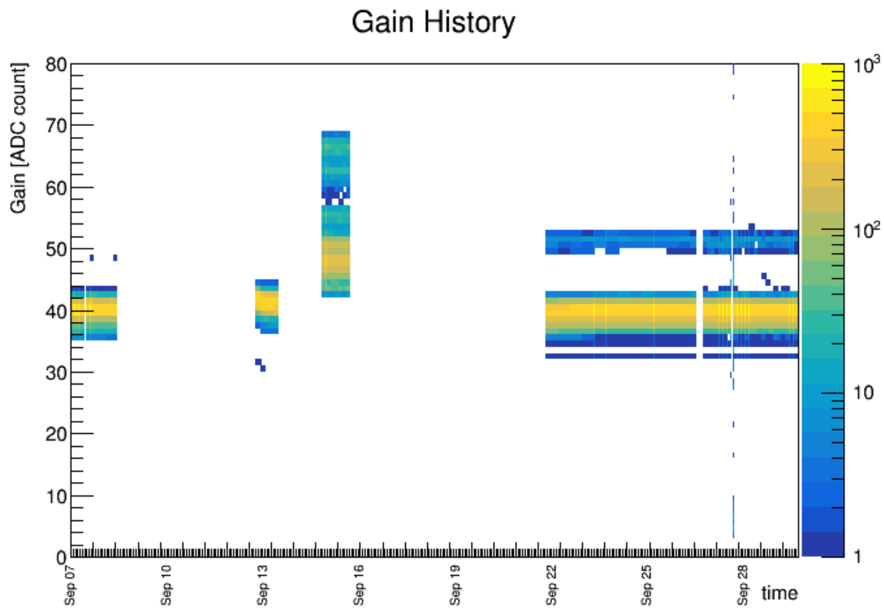

Figure 6.6: The stability of MPPC gain.

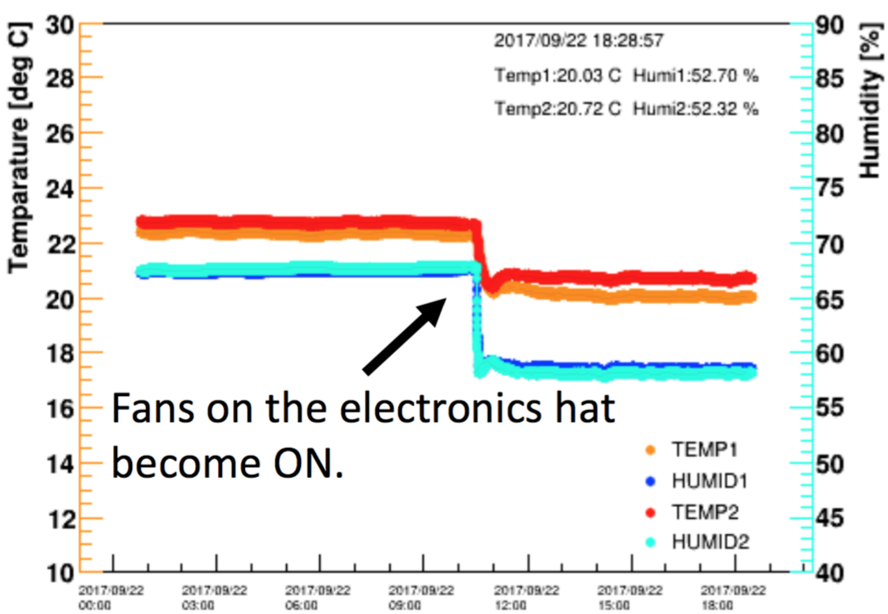

Figure 6.7: The temperature and humidity inside electronics housing. Red line is for temperature and blue line is for humidity. Both temperature and humidity changed before and after fans on the electronics housing working, but both of them is stable.

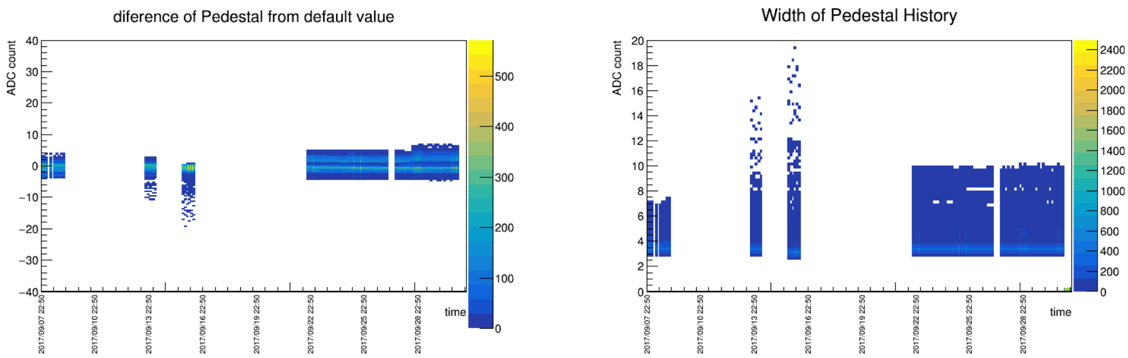

Figure 6.8: The stability of pedestal mean(left) and width(right).

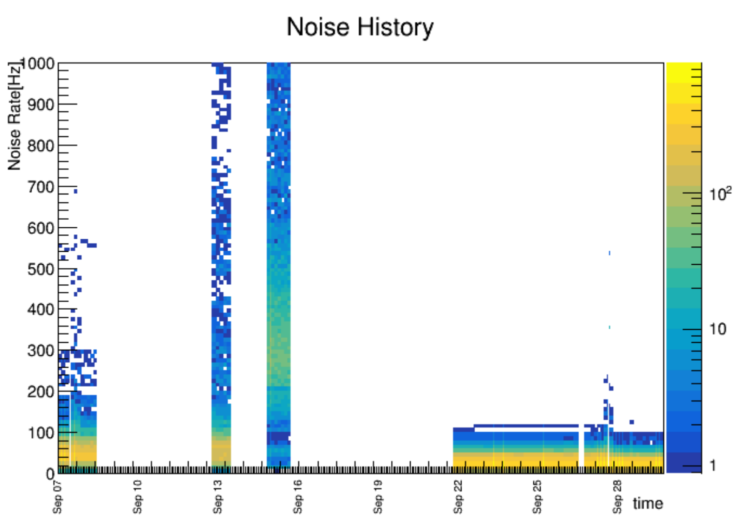

Figure 6.9: The stability of noise rate.

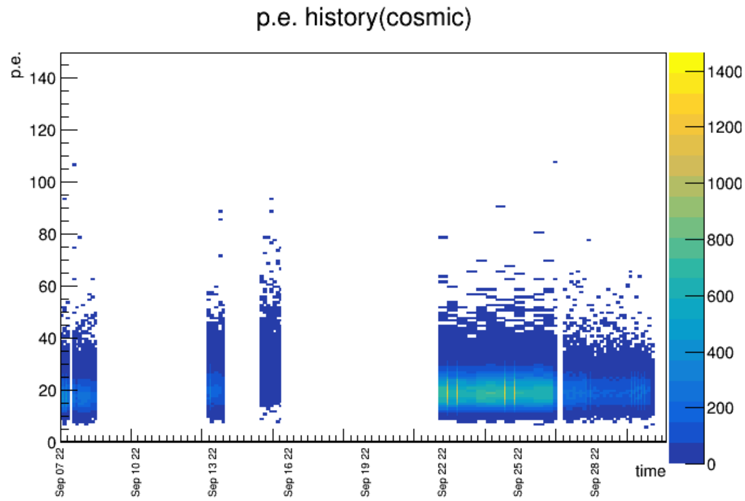

Figure 6.10: The stability of light yield.

Light leak was found while pouring water and it made DAQ unstable, but MPPC, electronics and the detector has been working stable with no dead channel.

6.4 Basic distribution

For the reconstructed track, basic distribution is checked. Because of the inefficiency of track reconstruction of multi-track events, the event in which the number of tracks is one is only selected. This selection rejects cosmic shower events and accidental coincidence events shown in Fig,6.11 and single muon event is selected.

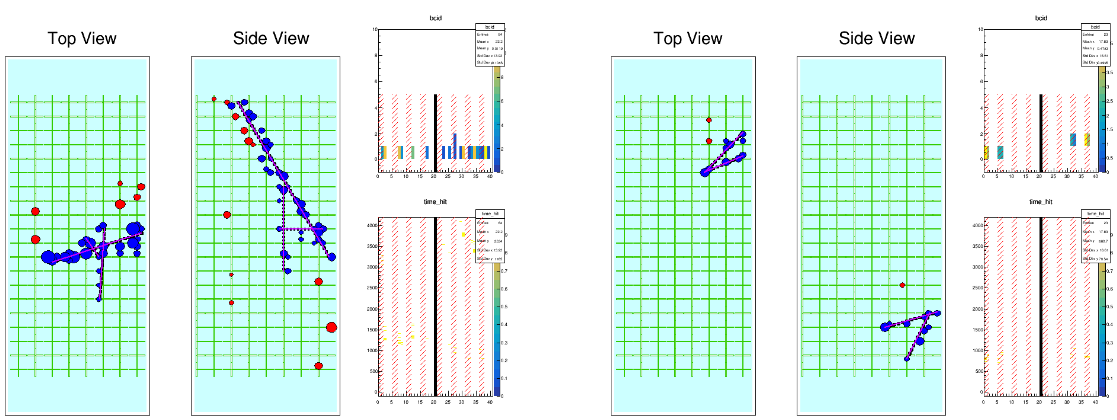

Figure 6.11: Cosmic shower event(left) and accidental coincidence event(right).

6.4.1 Photo electron distribution

Figure 6.13 shows the raw p.e. distribution and normalized p.e. distribution with path length. The light yield of both grid and parallel scintillator bars of top view and grid scintillator bars of side view is higher than grid scintillator bars of side view. It is because the long side of both parallel and grid scintillator bars of top view and parallel ones of side view is parallel to vertical line so path length is long for cosmic rays. The normalization of p.e. by path length cancels the path length effect. The mean of energy deposit converted into p.e. is about 10.

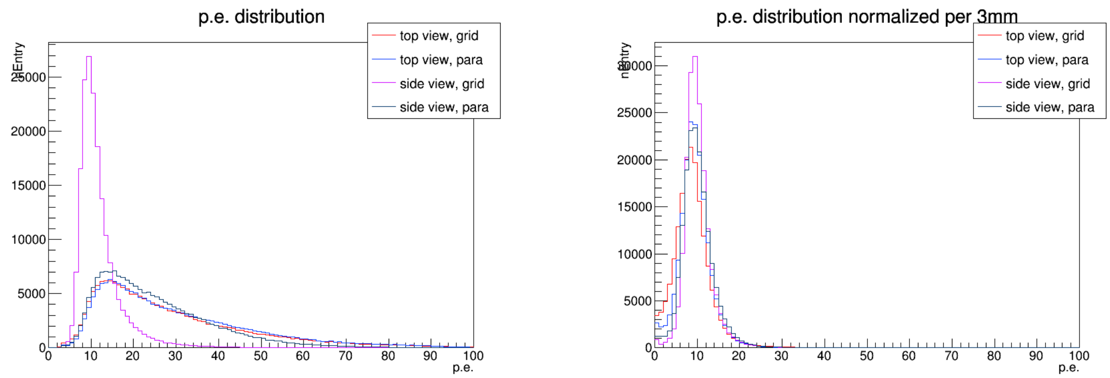

Figure 6.12: Photo electron distribution (left) and normalized photo electron distribution with path length distribution(right).

Figure 6.13 shows the map of mean of raw p.e. and normalized p.e. The individual difference of scintillator bars is seen, but energy deposit is roughly uniform. Figure 6.14 shows the one-dimensional histogram of normalized p.e. There are three bad channels and they corresponds the known three bad channels.

Figure 6.15 shows the accumulated number of hits of all channels. The difference of acceptance between grid scintillator and plane scintillator is seen in side view. In contrast, it is uniform in top view. The efficiency of bad channels is lower than the other channels, but it does not affect the efficiency of other channels around bad channels. It means the effect of these bad channels on reconstruction efficiency is small.

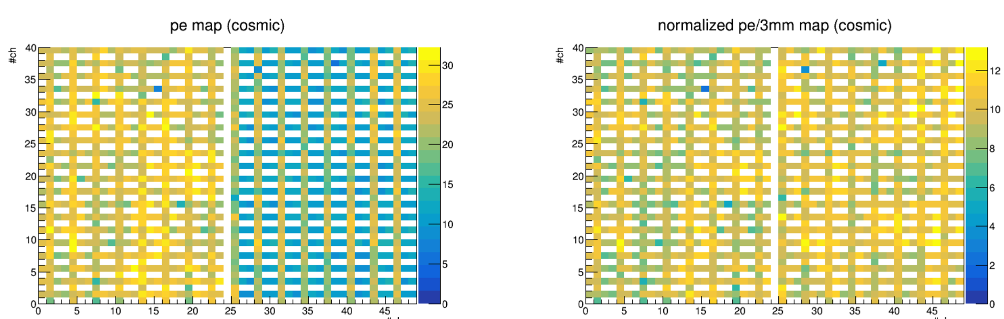

Figure 6.13: The map of mean p.e. (left) and p.e. normalized with path length (right).

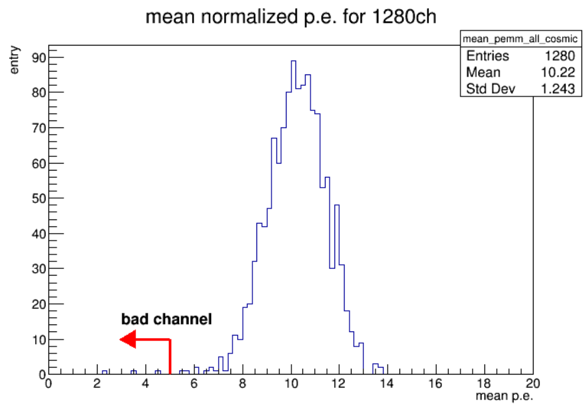

Figure 6.14: The normalized p.e. distribution. The p.e. is normalized per 3mm path length.

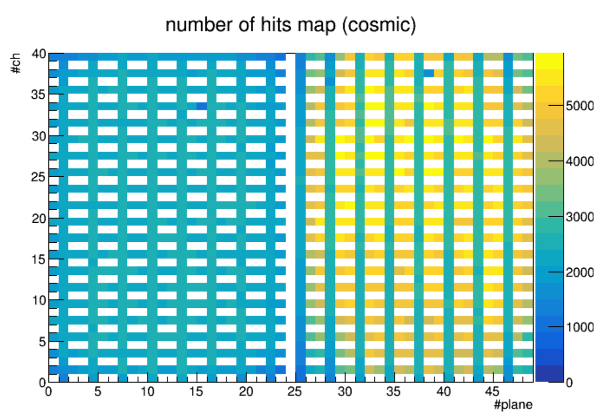

Figure 6.15: The map of the number of hits. The number of hits of bad channels is lower than the others.

6.4.2 Vertex position

Figure 6.16 shows the position of vertex and Fig. 6.17 shows the two-dimensional position of vertex. The vertex is defined as the upstream point of track so vertex position z is biased to upstream. Also, the vertex position x and y tends to be in the both side because cosmic muon comes from outside of the detector.

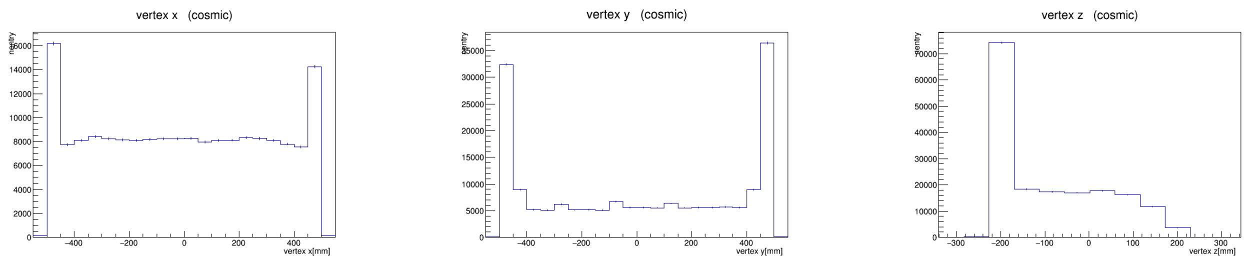

Figure 6.16: Vertex position of x(left), y(Center), z(Right).

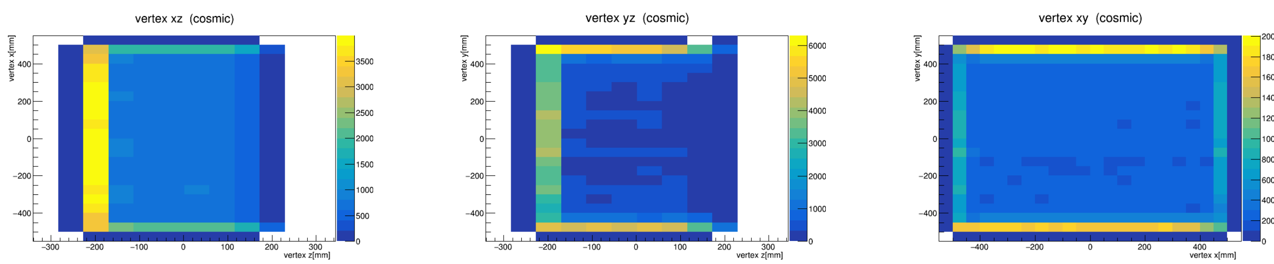

Figure 6.17: Vertex position of xy(left), xz(center), yz(right).

6.4.3 Angle

Figure 6.18 shows the distribution of zenith angle and azimuth angle. The azimuth angle is defined as the track of which azimuth angle is zero is parallel to X axis. Cosmic events are biased to the zenith direction. Azimuth angle distribution is not uniform and it is due to the structure of the detector. Figure 6.19 shows the azimuth angle distribution with rough binning. Because the efficiency of the detector is not so uniform that the distribution is not perfectly flat, it is roughly consistent with the flat distribution.

6.4.4 Event rate

Figure 6.20 shows the event rate history of cosmic events for third period. Event rate is calculated as following equation.

$$Event\ rate\ [Hz] = \frac{(The\ number\ of\ observed\ tracks)}{(The\ number\ of\ accumulated\ spill) \times (acquisition\ gate\ time[s])}\ , \tag{6.2}$$

where acquisition gate time for periodic trigger is 5ms.

The event rate of cosmic is stable. The event rate of cosmic is 12.88±0.4 Hz and it corresponds 6×10^{-5} events per one spill in the neutrino beam window. In current typical operation status of

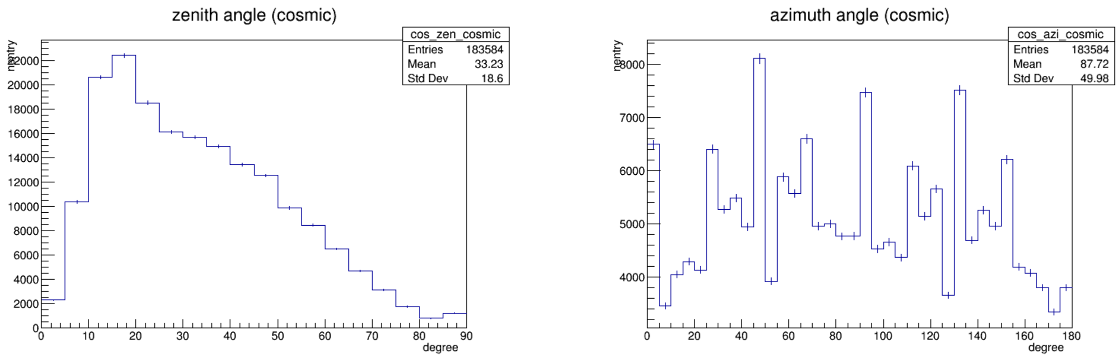

Figure 6.18: zenith angle distribution (left) and azimuth angle distribution(right).

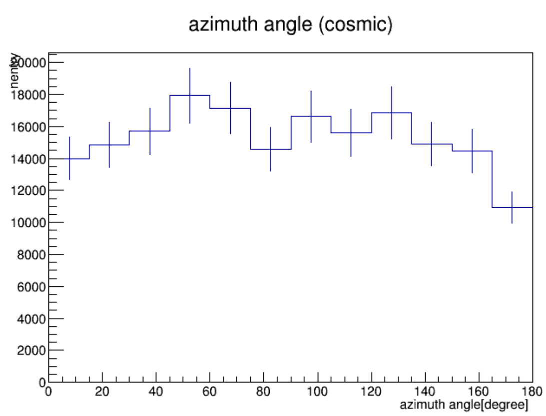

Figure 6.19: azimuth angle distribution with rough binning.

neutrino beam line, about 2×10^{14} protons on targets are expected in a spill so 30 cosmic events are expected in the neutrino beam window when $1.0{\times}10^{20}$ POT is accumulated. The expected number of neutrino candidates depends on the selection, but it is around a hundred events in $\bar{\nu}$ CCQE mode. So cosmic events is not negligible without veto cut. The contamination of cosmic event to neutrino beam measurement is discussed in the next chapter in detail.

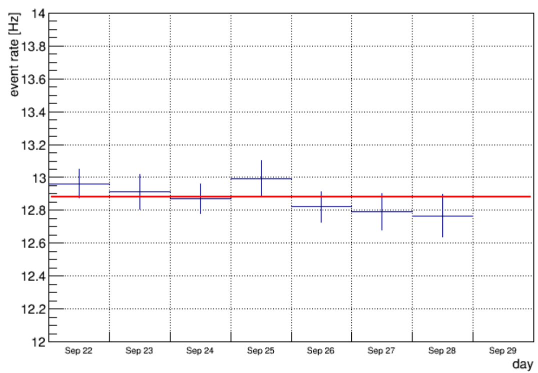

Figure 6.20: The event rate of cosmic events.

6.4.5 TDC clustering

As described in section 5.4.2, TDC clustering is not done in current analysis because there is the constant mismatch of BCID among chips. But as described in chapter 4, relative hit timing measurement is valid so relative hit timing is checked. Relative hit timing is calculated by subtracting mean hit timing of hits on track from hit timing of a hit. Because the effect of the gap of BCID is obscure, mean hit timing is calculated from hits of which BCID is same value. Figure 6.21 shows relative hit timing distribution of hits in a track. Currently the calibration of the TDC offset of each chip has not been done, so relative hit timing depends on the offset of each chips, but almost all hits is in the $\pm$100ns range.

However, a large number of hits are concentrated to a bin. It is because TDC ramp goes out from the valid range of a 12-bit AD converter and TDC value is saturated as shown in Fig. 6.22. Originally, the slope of TDC ramp is designed for the bunch crossing clock of which period is 400ns. One bit of TDC is optimized to correspond about 100ps (400ns/4096(12bit) 100ps). However, we changed the period of bunch crossing clock from 400ns to 580ns in order to optimize for T2K bunch structure. The slope of TDC ramp are fixed, so the ramp overflows the valid range and dead range corresponding to about 180ns appears.

The dead range can be estimated by counting saturated accidental events because the the probability that accidental events comes randomly and So the dead range is evaluated by the ratio of saturated events to not saturated events. Table.6.1 shows the ratio of underflow and overflow events to not saturated events. It indicates there is the dead range corresponding about 142ns and the effective range corresponds to 438ns.

Figure 6.23 shows the relative hit timing distribution except such saturated hits. A concentrated bin disappear and the hit timing distributes gaussian. 99.5% of all hits is in the $\pm$100ns range. It indicates the possibility of TDC clustering with relative hit timing. Also, if the problem on reset of bunch crossing clock is solved, more strong constraint for neutrino beam timing cut can be applied.

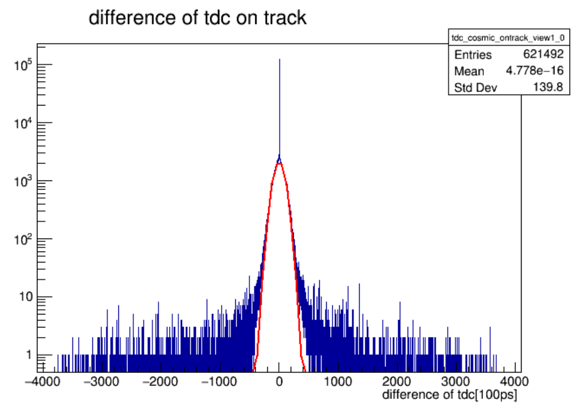

Figure 6.21: Relative hit timing distribution.

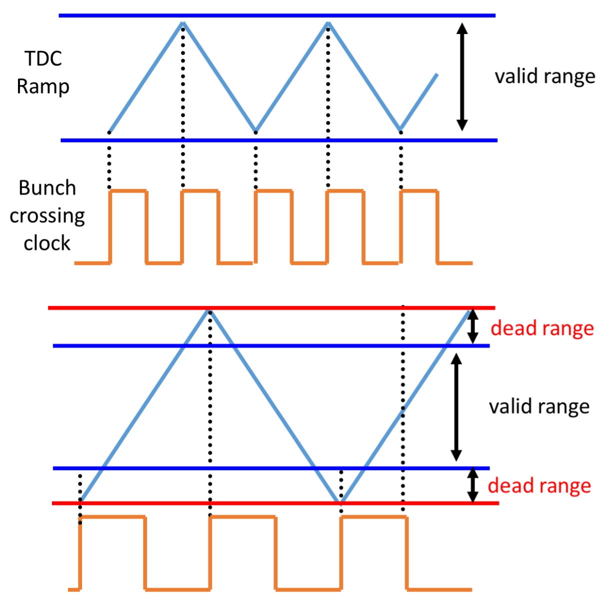

Figure 6.22: Schematic of TDC ramp and dead range.

Table 6.1: The ratio of saturated events to not saturated events. The values in brackets is the calculated valid or dead time in case that the period of bunch crossing clock is 580ns.

Ramp direction	underflow event	overflow event	not saturated event
up	1773	2418	17143
	10.34%(60.0ns)	14.10%(81.8ns)	75.60%(438.2ns)
down	1772	2431	17173
	10.31%(59.8ns)	14.16%(82.1ns)	75.53%(438.1ns)

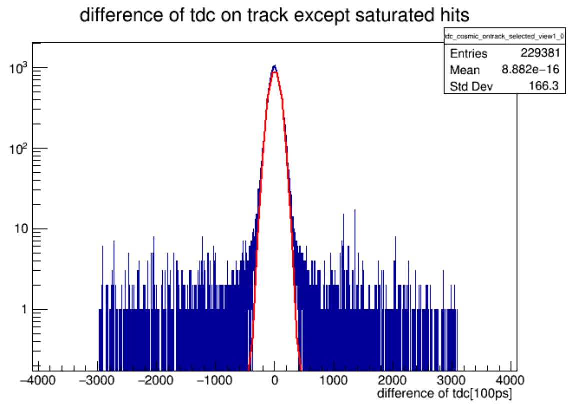

Figure 6.23: Relative hit timing distribution except saturated hits.

6.5 Summary

The module was installed on 1.5° off-axis and has started the operation. The detector and electronics have been working stably and succeeded to reconstruct tracks and to measure the cosmic events. The mean energy deposit converted into p.e. is about 10 and vertex position matches the distribution of cosmic ray. The event rate of incoming cosmic to Water Module is 12Hz and it indicates the need of veto cut for neutrino beam measurement.

Chapter 7

Measurement with neutrino beam

WAGASCI experiment has taken data with the neutrino beam from October 15th, 2017 to December 22nd, 2017. This chapter reports the status and performance of detector during neutrino beam measurement.

7.1 Data set

The neutrino beam data is taken by beam trigger mode. In beam trigger mode, 46.4μs acquisition gate opens 14.5μs before first neutrino beam bunch comes. After acquisition gate for neutrino beam measurement is closed, dark noise and cosmic ray are taken by periodic trigger in order to check the stability of the detector. The width of periodic trigger is 5ms and the period is 260 ms. The periodic trigger repeats six times and it finishes about 500ms before beam trigger comes.

Fortunately, we have beam time for both neutrino mode and anti-neutrino mode. Neutrino beam measurement has been done from October 15th to October 22nd and anti neutrino beam measurement has been done from October 22nd in December 22nd. Figure.7.1 shows the history plot of the accumulated number of protons on target(POT). Sometimes DAQ stops for switching of run and some beam triggers are missed. Table.7.1 shows the summary of pot and spill and data taking efficiency.

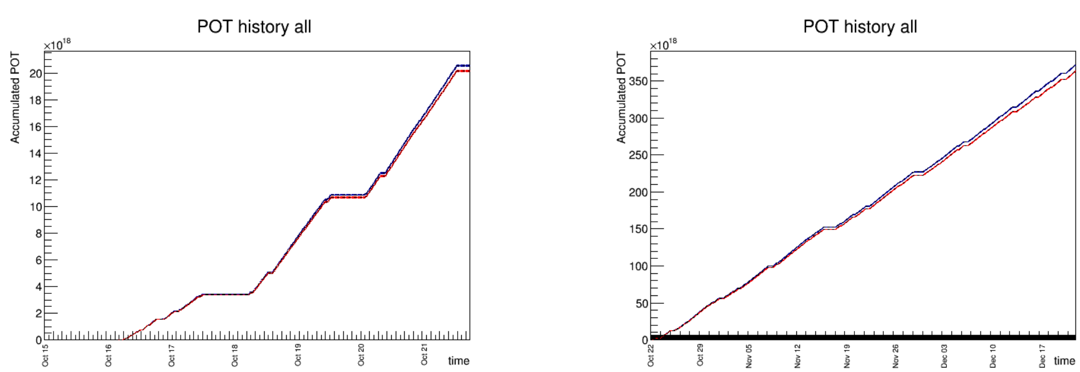

Figure 7.1: Accumulated protons on target history while neutrino mode (left) and anti while anti neutrino mode(right). Red line is for recorded POT and black is for total.

Table 7.1: The number of accumulated POT.

	neutrino mode	anti neutrino mode
period	Oct. 15-Oct. 22	Oct. 22-Dec. 22
recorded POT	2.01657×10^{19}	3.63108×10^{20}
missed POT	3.87620×10^{17}	8.50674×10^{18}
total POT	2.05534×10^{19}	3.71615×10^{20}
recorded spill	111882	1561365
missed spill	2137	34820
total spill	115019	1596185
data taking efficiency	98.1%	97.7%

7.2 MPPC and electronics stability

Figure 7.2 shows the gain history. While neutrino mode, gain is totally stable. While anti neutrino mode, the gain is almost stable but the small variation had been seen since November 21st for 9 days. While the period, the humidity decreased suddenly from 56% to 24%. So the electronics housing was opened and the source of problem was investigated but no abnormality was found on the electronics and temperature and humidity sensor. However humidity recovered to 42% so electronics housing was closed and restarted to run. This investigation was done while neutrino beam stopped, so it did not affect the DAQ status. Also, the variation of gain is sufficiently small. A channel had larger gain but it was not because the gain was abnormal but because the threshold tuning was not for optimized as shown in Fig. 7.2. This channel was independently checked and no abnormality was seen in photo electron distribution so the channel was not included in dead channel.

Figure 7.3 shows the noise history. Same as gain history, noise rate is stable except the period from November 21st to November 30th. In this period, threshold was set a bit higher than 2.5 p.e. equivalent level but smaller then 3.0 p.e. equivalent level so the noise rate got a bit smaller. The observed photo electron while commissioning was higher than 3.0 p.e. as shown in Fig. 6.12 so it did not affect the data quality.

The effect of dark noise to reconstruction can be calculated. Noise rate is less than 70Hz and in the current reconstruction method, the hits in 2 BCID corresponding 1.06μs is clustered. So the expected number of noise hits is calculated as following:

$$
\begin{aligned}
\#expected\ dark\ noise\ hits &= 1280\ channels \times 1.06\ \mu s \times 70\ Hz \\
&= 0.10
\end{aligned}
$$

So the effect of dark noise on reconstruction is almost negligible.

Figure 7.4 shows the pedestal history. The pedestal is very stable for all period.

Figure 7.5 shows the width of pedestal history. Same as gain, width of pedestal is stable except the period from November 21st to November 30th. It is expected that the ground got a bit unstable for that period. However the variation was also small so it did not affect the data quality.

Figure 7.6 shows the mean p.e. history of the accidental events. It is stable.

7.3 Event selection

For neutrino measurement, background events such as cosmic muon events and sand muon events should be rejected efficiently. Sand muon event is the background produced by neutrino interaction in upstream materials, mainly the wall, so the event timing is synchronized to the beam trigger.

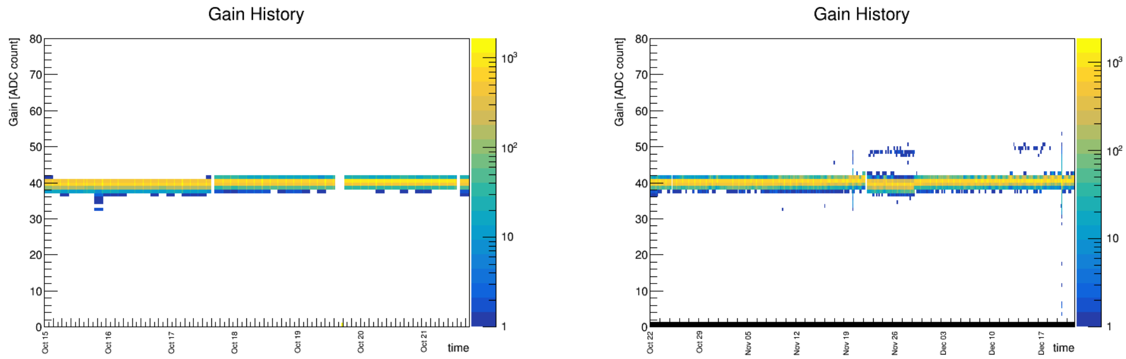

Figure 7.2: Gain history while neutrino mode(left) and while anti neutrino mode(right).

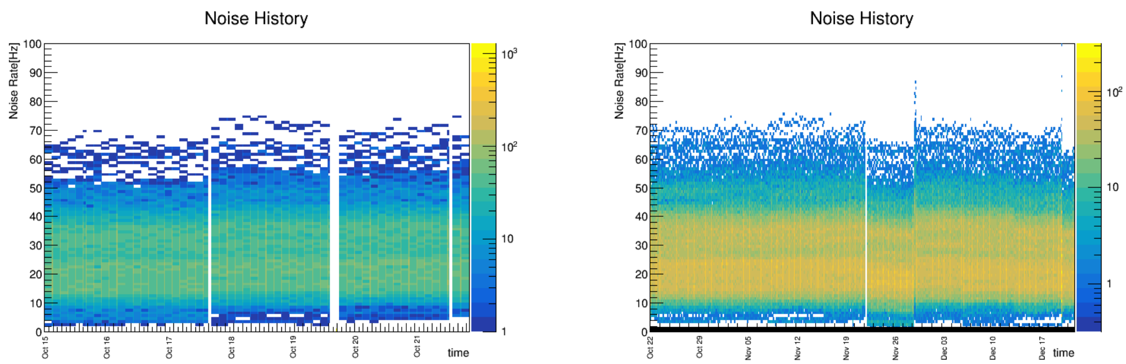

Figure 7.3: Noise history while neutrino mode(left) and while anti neutrino mode(right).

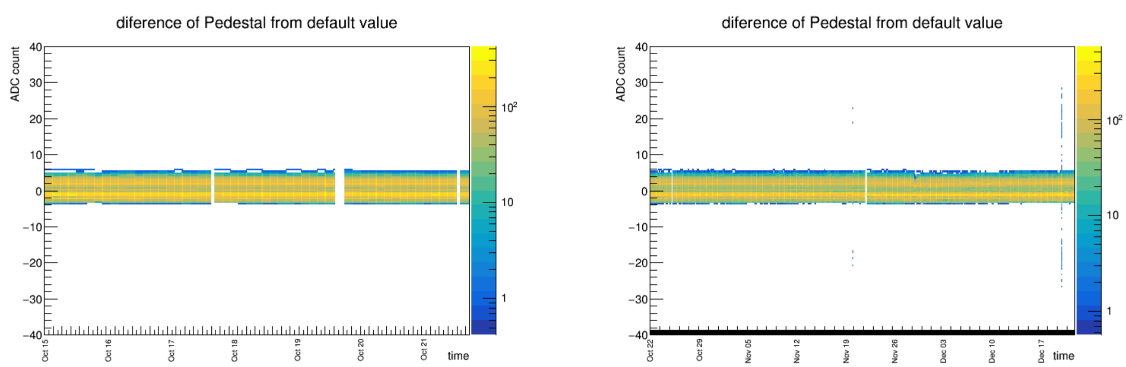

Figure 7.4: Pedestal history while neutrino mode(left) and while anti neutrino mode(right).

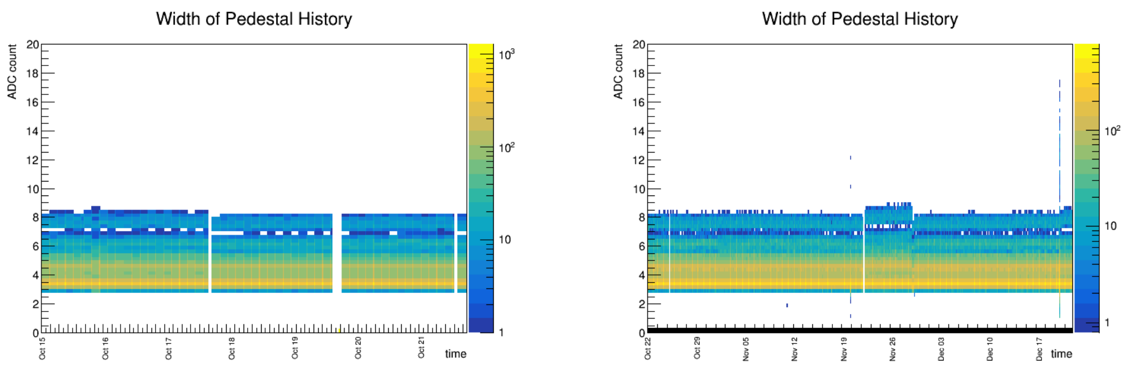

Figure 7.5: Width of pedestal history while neutrino mode(left) and while anti neutrino mode(right).

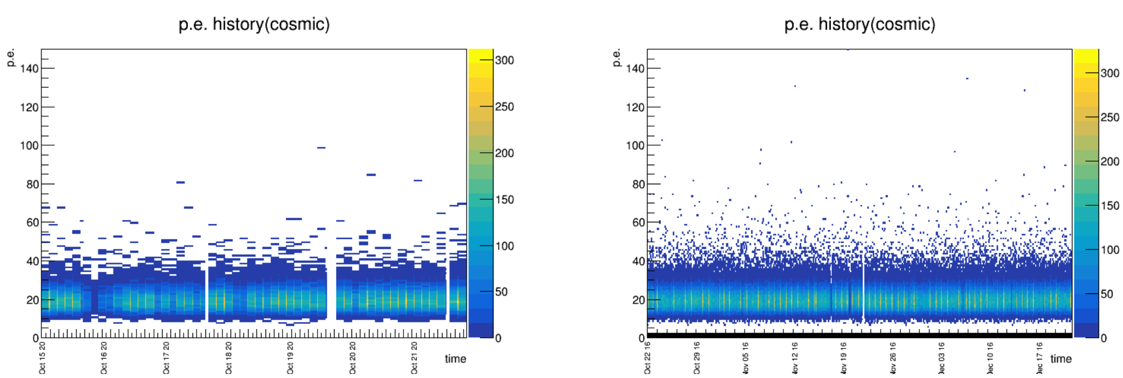

Figure 7.6: Mean p.e. history of accidental events while neutrino mode(left) and while anti neutrino mode(right).

This selection is temporary. It should be also checked using MC simulation and evaluated comparing the data and true information. The following list is the current selection method.

1. Light yield cut
   As described in section 4.3.4, there are fake hits. In order reject them, the hits of which measured p.e. is less than 2.5 are rejected.

2. Track reconstruction cut
   The events that at least one two-dimensional track is reconstructed in both top and side view are selected. Figure 7.7 shows the example of a rejected event by this selection. The events that two-dimensional track is reconstructed in both top and side view but fail three-dimensional track matching are also rejected. Figure 7.8 shows the example of a rejected event by this selection.

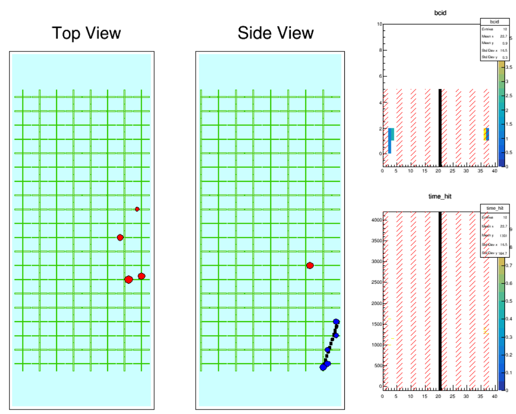

Figure 7.7: A event rejected for no track in ether of view.

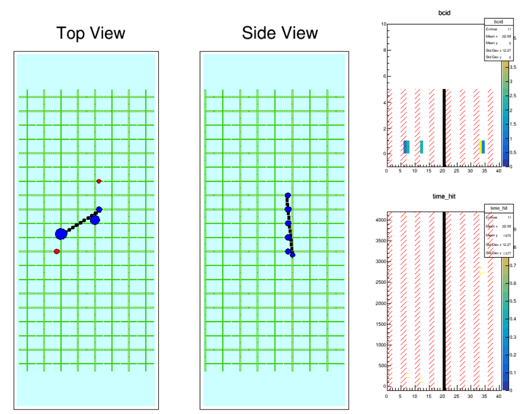

Figure 7.8: A event rejected for no three-dimensional matching track.

3. Timing and trigger mode cut
   As described in section 7.1, there is two trigger. One is the beam trigger and the other is the periodic trigger. The former is for neutrino measurement and the later is for data quality check. The events which taken by the beam trigger is only used.

   Beam timing is also checked. The number of beam bunches is 8 so beam timing is originally expected to distribute 8 over BCID bins. However, considering the wrong reset timing of bunch crossing clock, it is expected to distribute 9 BCID bins. The acquisition gate for the beam trigger opens 15μs before first neutrino beam bunch comes, so beam timing windows is set from 26 to 35 BCID.

4. Veto cut
   In order to reject background events coming from outside, the veto cut is applied. Figure 7.9 is the region of veto plane. Considering the inefficiency, the outside two planes are defined as the veto planes. When a vertex is inside veto planes, the event is rejected.

   By veto cut, the background due to incoming charged particles from the upstream and side of the detector, especially sand muon event, is rejected. However, the background which incomes from downstream of the detector and stops inside detector can not be separated from neutrino events. The decay muon events also can not be separated.

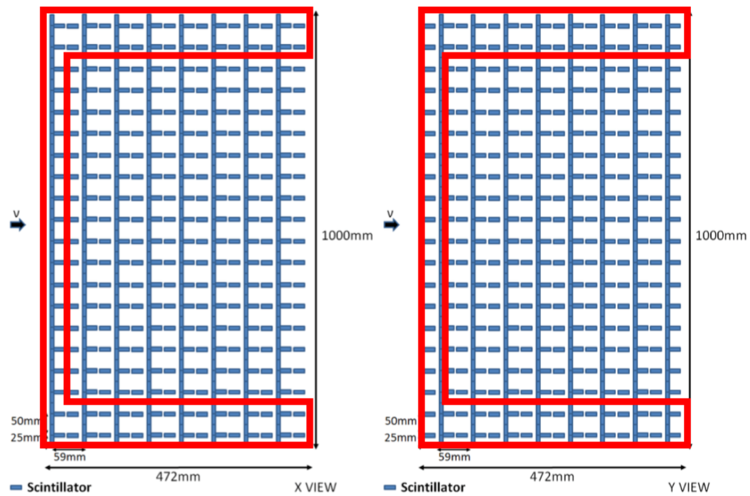

Figure 7.9: The definition of veto region.

7.4 Event rate of background sand muon

The event, in which charged particle is produced in neutrino interaction inside walls and it incomes to the detector, is called sand muon event. Depending on the inefficiency of veto cut, almost all sand muon events are rejected by applying veto cut. However, event rate of sand muon events correlates with neutrino beam flux, so it is useful to monitor event rate of sand muon events. Sand muon event is defined as the event which is inside beam timing cut but is cut off by applying veto cut.

Firstly, Beam timing is checked. Fig. 7.10 shows the BCID distribution. The blue line is for the all reconstructed events taken by the beam trigger mode. Almost all events is in the expected timing.

However, the tail is seen after beam timing in both neutrino mode and anti neutrino mode. It is expected due to the electron produced in the decay of muon which stops inside the module. The lifetime is calculated by fitting this tail with an exponential function. The calculated lifetime is shown in Table.7.2. It is consistent with the μ^+ lifetime, 2.20us at 1σ range. μ^- lifetime gets shorter than μ^+ lifetime due to absorption by nuclei. About 80% of detector volume is filled with water so the fit result is compared with μ^- lifetime in O[32], 1.80us. It is also consistent at 1σ range.

Red line is for cosmic events taken by periodic trigger. As described in section 6.4.4, the cosmic event rate is not so small. Here the veto cut is applied to evaluate event rate after selection. Also, the number of events is normalized by the ratio of the number of periodic triggers to that of beam triggers. The 95% of cosmic events is rejected by veto cut and the contamination of cosmic events for neutrino beam measurement is very low.

Table 7.2: The best-fit value and 1 sigma allowed range of calculated lifetime.

	neutrino mode	anti neutrino mode
best-fit value [us]	1.50	2.22
1σ range [us]	1.23-1.91	2.06-2.40

Secondly, vertex position is checked. Figure 7.11 shows the vertex position of sand muon events in neutrino mode and Fig. 7.12 shows that in anti-neutrino mode. Little difference of vertex position is seen in neutrino mode and anti-neutrino mode. Most of vertex position z of sand muon events are

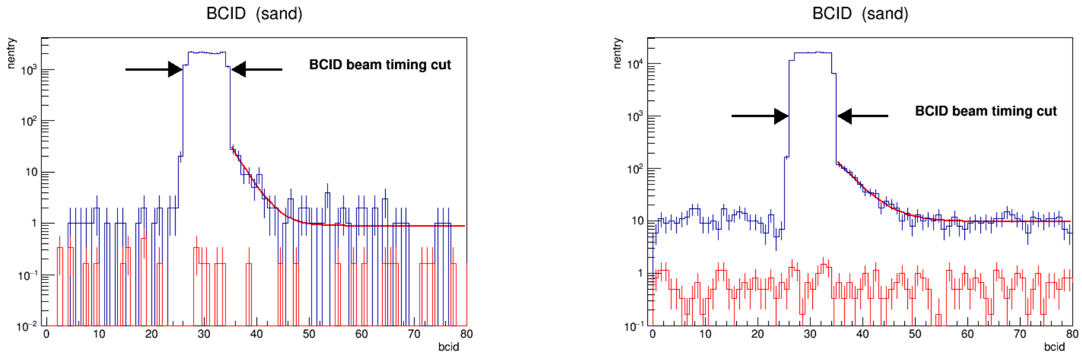

Figure 7.10: BCID distribution for neutrino mode(left) and anti neutrino mode(right). The blue line is for the all reconstructed events taken by neutrino beam trigger mode and red line is for the reconstructed cosmic events. For the cosmic events, veto cut selection is applied.

inside most upstream plane. It is consistent with sand muon distribution. Vertex position x and y depends on the installation position of the detector, it is under investigation.

Also, in order to select sand-muon like events, the event in which the number of tracks is equal to one is only selected. Figure 7.13 shows the number of tracks of background events after applying beam timing cut. It shows the main component of back ground events is one track events and little difference is seen in neutrino mode and anti-neutrino mode. So one track event selection makes sense to estimate event rate of sand muon.

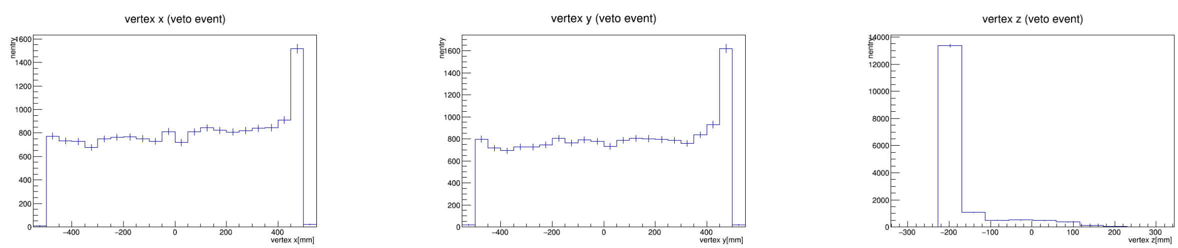

Figure 7.11: Reconstructed vertex distribution of sand muon events in neutrino mode.

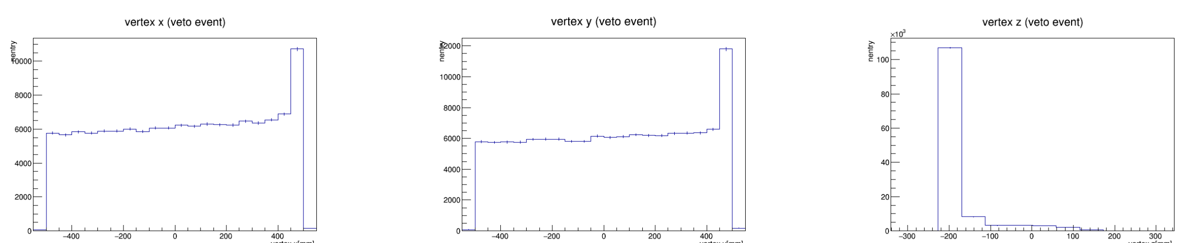

Figure 7.12: Reconstructed vertex distribution of sand muon events in anti-neutrino mode.

Figure 7.14 shows the event rate of sand muon events with neutrino mode and with anti neutrino mode. The event rate is stable. Table 7.3 shows the result of fitting of event rate with neutrino mode and with anti neutrino mode.

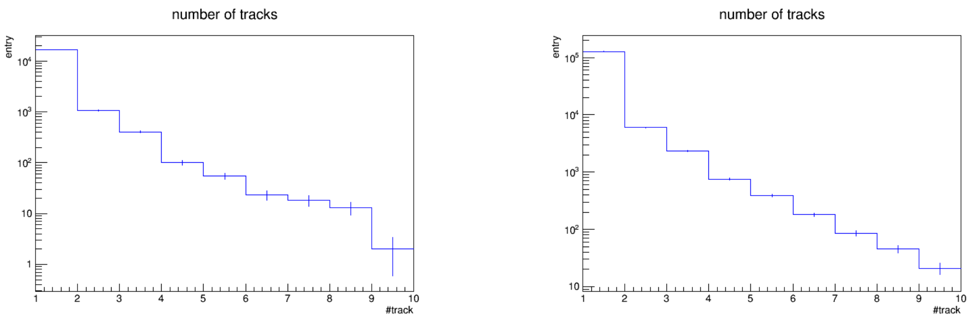

Figure 7.13: The number of tracks distribution in neutrino mode(left) and anti-neutrino mode(right). One track event is the main contribution in both of neutrino and anti-neutrino mode.

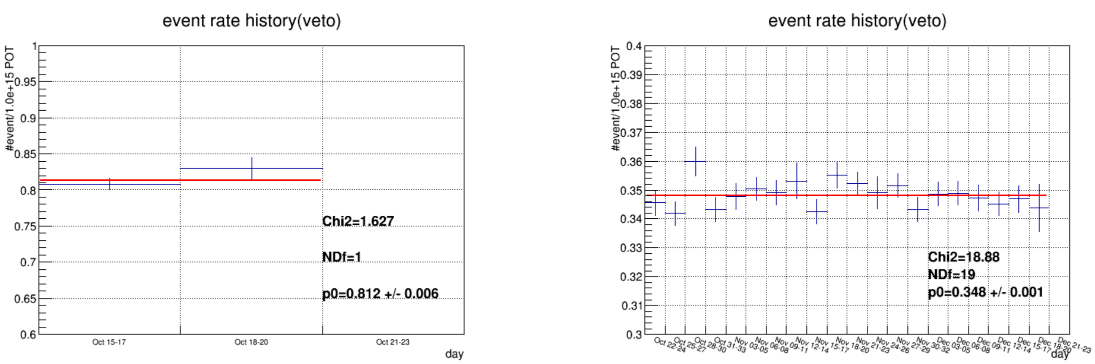

Figure 7.14: The event rate of sand muon events with neutrino mode(left) and anti neutrino mode(right). The event rate is normalized by 10^{15}POT.

Table 7.3: The best-fit value and 1 sigma allowed range of event rate of sand muon.

	neutrino mode	anti neutrino mode
best-fit value [#events/10^{15}POT]	0.812	0.348
1σ range [#events/10^{15}POT]	0.806-0.818	0.347-0.349

7.5 Observation of neutrino event

The selection is applied to observe neutrino event. However, the contamination of background events, especially decayed muon, is under investigation. So the result of vertex position after veto cut and several event display for observed neutrino candidates are described.

Figure 7.15 shows the vertex distribution before applying veto cut in neutrino mode and Fig. 7.16 shows that in anti-neutrino mode. Figure 7.17 shows the vertex distribution after applying the veto cut in neutrino mode and Fig. 7.18 shows that in anti-neutrino mode.

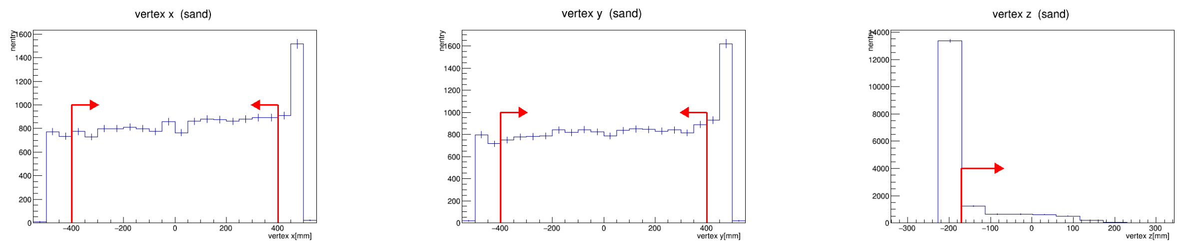

Figure 7.15: Reconstructed vertex distribution before applying veto cut in neutrino mode. Left figure is for vertex x position, center is for y position and right is for z position. Red arrows show the region outside vertex region.

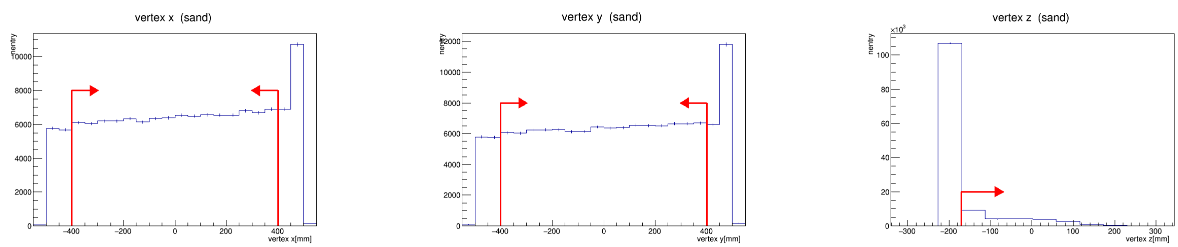

Figure 7.16: Reconstructed vertex distribution before applying veto cut in anti-neutrino mode. Left figure is for vertex x position, center is for y position and right is for z position. Red arrows show the region outside vertex region.

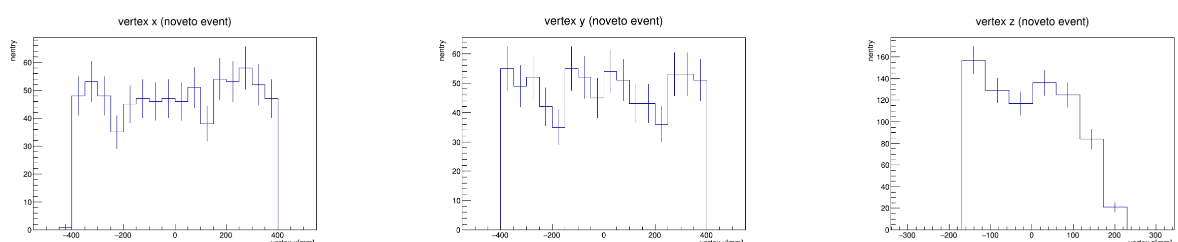

Figure 7.17: Reconstructed vertex distribution after applying veto cut in neutrino mode.

During beam measurement, we have succeeded to observe the neutrino event candidates. Here, several neutrino candidates are shown in Fig. 7.19-Fig. 7.28.

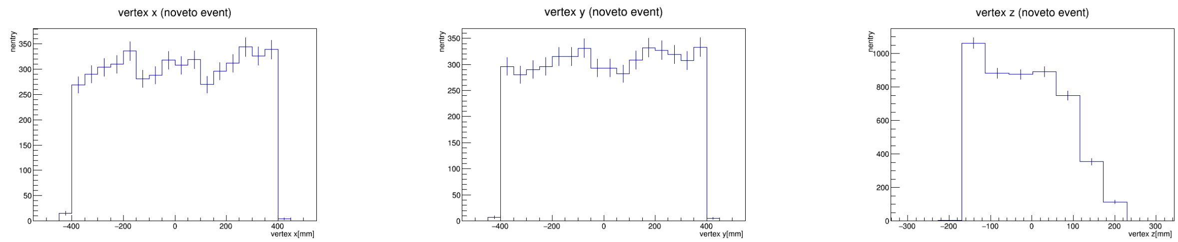

Figure 7.18: Reconstructed vertex distribution after applying veto cut in anti-neutrino mode.

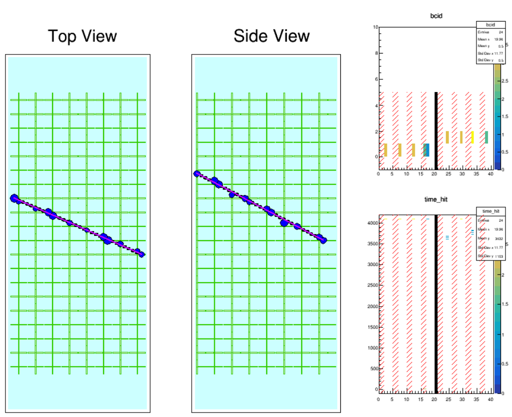

Figure 7.19: The incoming charge particle. It is rejected as sand muon event. It is expected as muon because energy deposit is not so large.

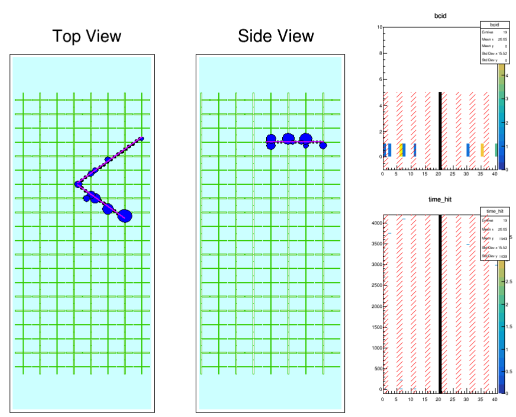

Figure 7.20: The candidates of neutrino interaction in ν mode. There are two tracks and a track which energy deposit is large is guessed as proton and the other is guessed as muon.

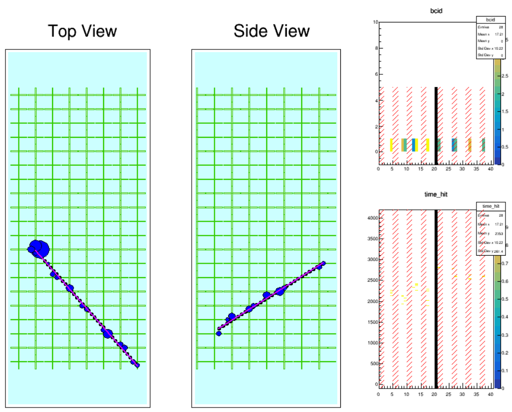

Figure 7.21: The candidates of neutrino interaction in ν mode. There is a track and it is guessed as muon or pion. The energy deposit around vertex is large so it is guessed that proton stops just after production.

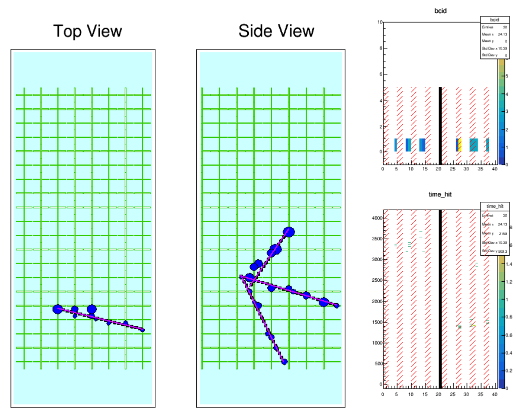

Figure 7.22: The candidates of neutrino interaction in ν mode. There are three tracks and a track which energy deposit is largest is guessed as proton and the others is guessed as muon and pion.

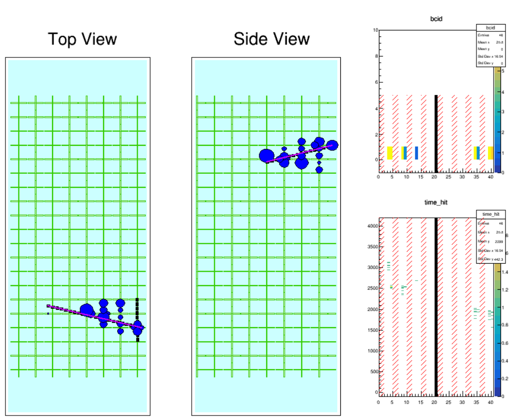

Figure 7.23: The candidates of neutrino interaction in ν mode. Many hits distributes at downstream of guessed vertex and fail to reconstruction.

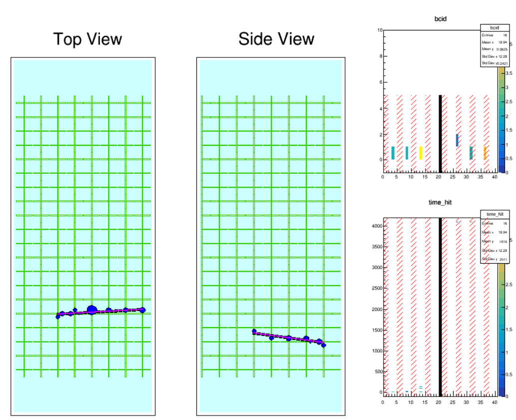

Figure 7.24: The candidates of neutrino interaction in $\bar{\nu}$ mode. A track is guessed as muon or pion.

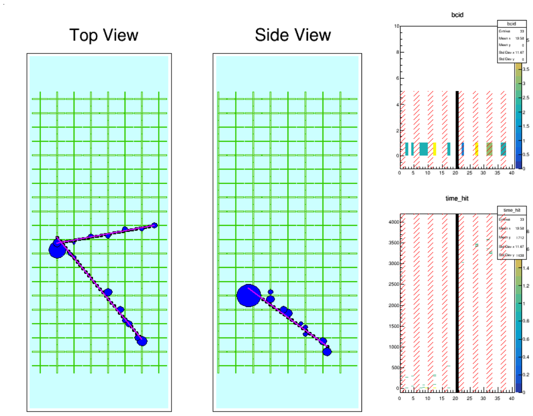

Figure 7.25: The candidates of neutrino interaction in $\bar{\nu}$ mode. There are two tracks. The energy deposit around vertex is large so it is guessed that proton stops just after production.

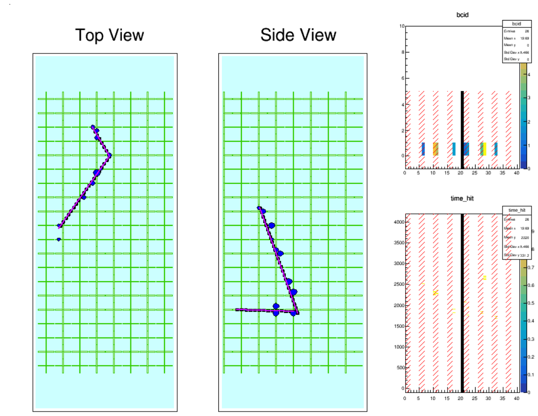

Figure 7.26: The candidates of neutrino interaction in $\bar{\nu}$ mode. There is two tracks and they are guessed as muon and pion, but momentum is not conserved. It is guessed that neutral particle is scattered forward and it is not observed.

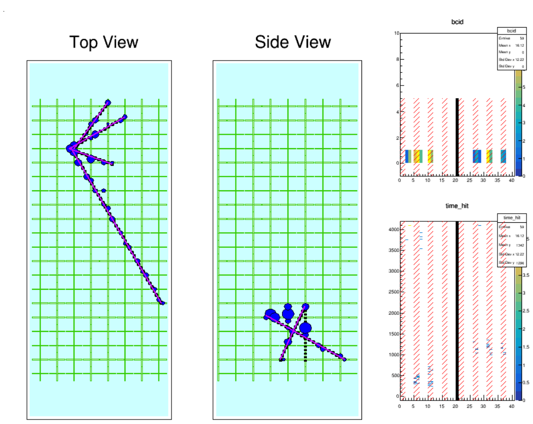

Figure 7.27: The candidates of neutrino interaction in $\bar{\nu}$ mode. Many tracks exist.

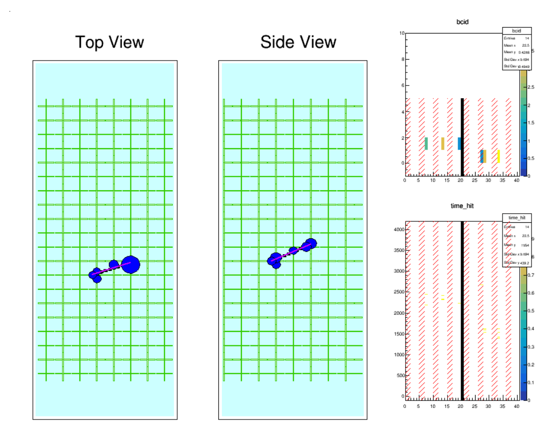

Figure 7.28: The candidates of neutrino interaction in $\bar{\nu}$ mode. There is a track which energy deposit is large and it is guessed as proton.

Chapter 8

Summary and future prospect

8.1 Summary

In order to reduce the systematic errors due to cross section in T2K neutrino oscillation measurement, we have been conducting WAGASCI experiment at J-PARC to measure cross-section ratio of water to hydro-carbon and cross section of water and hydrocarbon with a large acceptance.

The characteristics of 32-channel arrayed MPPCs and single MPPCs are measured. eighty four arrayed MPPCs corresponding to 2,688 channel and 1,400 single MPPCs are measured. It is confirmed 3,832 channels of them work fine and have sufficient performance for neutrino beam measurement and 1,280 channels are installed to the detector. The readout electronics based on SPIROC2D has been developed. This experiment is first application of SPIROC2D. SIROC2D has some known problems that the position of comparator is wrong. However, it is confirmed that SPIROC2D has sufficient performance for operation and readout of an arrayed MPPC. Also, operation with full setup is tested and we succeed to readout MPPC signal of 1,280 channels. 46 front-end boards are produced and 40 are installed to the detector.

We started the construction in October 2016. 1,500 scintillator bars are processed and it is confirmed by the test measurement with cosmic that sufficient light is obtained. Some problems delayed assembling schedule, but finally the construction finished in August 2017. The number of dead channels is three and the other 1,277 channels work stably. Because side MRDs and downstream MRD are under construction or transportation, we started pilot experiment with other existing modules, Proton Module and INGRID module. The installation of detectors finished in August 2017 and we started the detector operation with temporary setup in the beginning of September. The performance of the detector is tested with cosmic ray, and it is confirmed that electronics works stably and there is no new bad channel. The reconstruction algorithm has been developed and we succeed to observe cosmic ray. It is confirmed the detector has enough performance for observation of charged particle.

The neutrino beam measurement started on October 15th. The neutrino beam measurement has been done from October 15th to October 22nd and the anti-neutrino beam measurement has been done from October 22nd to December 22nd. The data acquisition has been going on stably and we succeed to accumulated 2.0×10^{19} POT in neutrino mode and 3.6×10^{20} POT in anti-neutrino mode. The event selection method is established and we succeed to observe neutrino candidates. The stability of wall background event rate is also checked and it is stable. The event rate of wall background for ν mode is 0.812 ± 0.006 events/10^{15}POT and that for $\bar{\nu}$ mode is 0.348 ± 0.001 events/10^{15}POT.

8.2 Future prospects

8.2.1 Confirmation and modification with current temporary setup

- **Electronics**
  Current electronics has a critical problem on the synchronization of bunch crossing clock to beam trigger. It makes the measurement of absolute hit timing impossible. This problem is on DIF firmware and improvement is planned in 2018. The improvement is essential for neutrino beam measurement and it is confirmed that update of DIF improves the performance of hit time measurement.

- **Reconstruction**
  Current reconstruction has a defect of reconstruction of multi tracks with small opening angle. The problem is due to reconstruction of short track and it is expected that more efficient reconstruction of short track improve the situation. One of the methods is to separate reconstruction into two steps. First is reconstruction for long track and second is for short track to specialize the reconstruction method according to track length. Another method is to optimize the ranking method. Currently, the candidates are ranked according to number of hits, length, sum of p.e. and sum of square errors, but it is not optimized. The optimization of ranking is expected to improve reconstruction.

  The TDC clustering is also one of the problems. The result of this thesis indicates TDC clustering makes sense. It is expected to reduce the pile up of neutrino events.

- **Particle identification**
  In this thesis, veto cut is used for the reduction of background event. However the contamination of background such as electrons and hadrons produced in interaction of incoming neutron and γ or in decay of muon is expected. Particle identification makes sense to identify the interaction mode and to reject background. The scattering particles can be identify by comparing track length with energy deposit. As shown in section 7.5, most of particles penetrate Water Module and track matching is needed to measure total path length.

8.2.2 Side MRDs and Baby MIND

Currently construction of side MRDs and production of front-end electronics is going on. The first module is planned to finish to be constructed in February 2018. The existence of side MRD improves the energy reconstruction at large acceptance. The shipment of BabyMIND, magnetized downstreamMRD, arrived at J-PARC in December 2017. Currently, the preparation of install and electronics has been going on. We plan to start neutrino beam measurement with full setup from 2018.

8.2.3 Neutrino measurement with full setup

WAGASCI experiment is planed to continue neutrino beam measurement. We plan neutrino beam measurement in both neutrino mode and anti-neutrino mode with full setup including Baby MIND and side MRDs from 2018. We plan one-year data taking($\sim 5 \times 10^{20}$ POT) in neutrino mode and another one-year data taking in anti-neutrino mode. The expected number of charged current interaction events in one-year data taking is $5,400$ in neutrino mode and $2,240$ in anti-neutrino mode. We will provide inclusive cross-section measurement and differential cross section measurement of charged current interaction with water and hydro-carbon with around 800MeV neutrino energy with large acceptance. The measurements would improve the comprehension of the neutrino-nucleus interaction in sub-GeV range and contribute to reducing systematic uncertainty due to cross section in T2K neutrino oscillation measurement.

Appendix A

Cellular automaton track reconstruction

The track reconstruction algorithm based on cellular automaton which has been developed for the analysis of the K2K SciBar detector. The cellar automaton is a dynamical systems that evolve in discrete steps. Space, time and the states of the system are discrete. Each cell has a finite number of states and the states of the cells evolve according to a local rule. The state of a cell at a given time depends on only on its state and the states of its nearby neighbors at the previous time step. All cells are updated synchronously.

In WAGASCI experiment, tracks of INGRID, Proton Module, Water Module and side MRDs are reconstructed based on Cellar automaton algorithm. Here, The reconstruction method based on cellar automaton for Water Module is described.

1. Define reconstruction plane and reconstruction channel
   The example of clustered hits is shown in Fig. A.1. Figure A.1 shows the definition of reconstruction plane and reconstruction channel of two axis. Left definition is define as along-z and right one is defined as along-xy. The reconstruction algorithm is done according to this definition two times independently. The difference between tracking of along-z and that of along-xy is only definition of reconstruction plane and channel. The reconstruction efficiency is different between tracking of along-z and that of along-xy. The tracking of along-z is efficient for the track whose angle with z-axis is small and that of along-xy is for the track whose angle is large. The following two-dimensional reconstruction method is described using figures for tracking of along-z.

2. Make cluster
   At first, two hits of neighboring reconstruction channel of the same reconstruction plane are organized as a cluster. The position of a cluster is calculated by the mean of position of each reconstruction channel weighted by light yield.

3. Make cells
   Two clusters are connected and defined as a cell as shown in FigA.3. Considering the inefficiency and geometrical acceptance due to the structure of scintillator bars, two clusters of which difference of reconstruction plane is less than 6 are connected. Each cell has a state value and at this step, the state value of all cells is defined as zero.

4. Make neighbor
   The pair of two cells which have common cluster is organized as a neighbor. A neighbor must satisfy the following limit : the opening angle of two clusters is more than 120 degrees. This

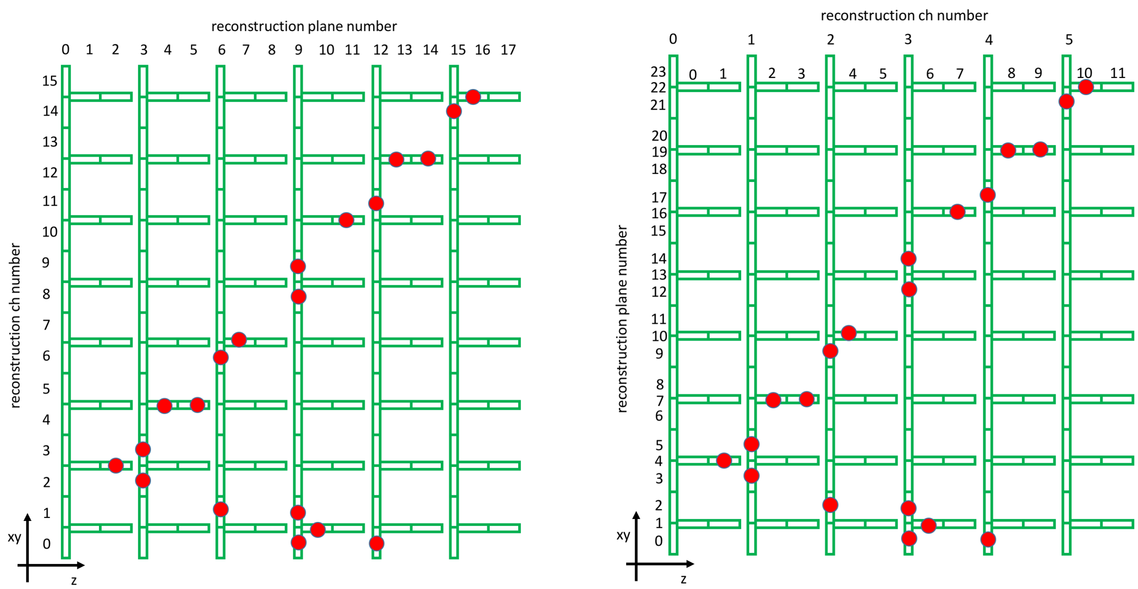

Figure A.1: Hit example for track reconstruction.

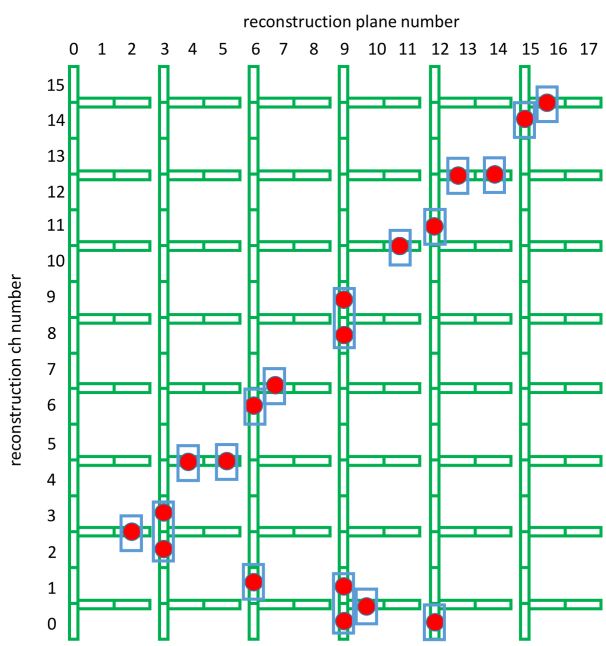

Figure A.2: Cluster made from hits.

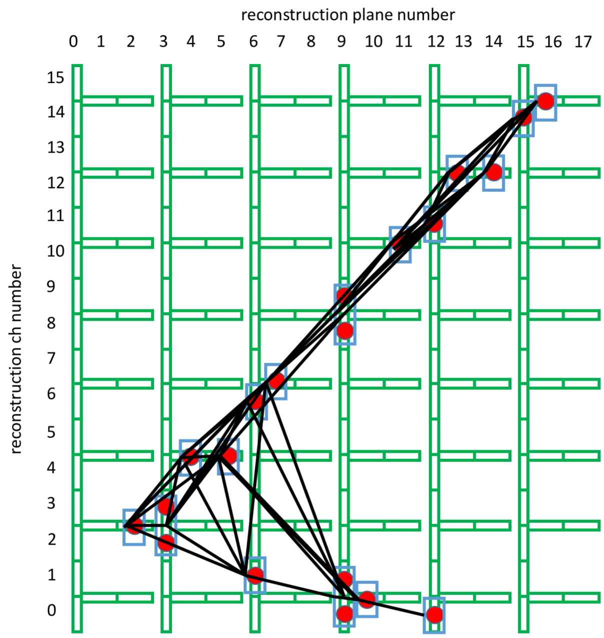

Figure A.3: Initial cells.

limit is defined considering the detector segmentation for linear track. If opening angle is less than 120 degrees, it is not considered as a neighbor.

5. Define cell state
   The state value of cells is defined step by step. At each step, the upstream neighbor is evaluated with downstream one. If there is a common cell in upstream neighbor and downstream neighbor and the state value of all cells in upstream neighbor and downstream neighbor is same, the two neighbor becomes pair and the state value of two cells in downstream neighbor increase by one. The cells state evolutes step by step and steps finish when there is no downstream neighbor.

6. Tracking
   The tracking starts from a downstream cells of neighbor which doesn't have the downstream pair. The algorithm tracks back the neighbor upstream cells. At each step, track validity is checked by upper limit on the sum of square error which is computed from a linear fitting. If the sum of square error is more than the certain value or the state value of the upstream cell is zero, the tracking is stopped and moves next start point. If there is more than one start points, tracking starts from the downstream cell whose state value is more. After tracking for each start point is finished, some candidates of track are reconstructed as shown in Fig. A.5. Because of the limit for opening angle in neighboring, a few hits sometimes failed to be reconstructed. So the hits of which distance from a near track is less than 25 mm are picked up and become part of candidates.

7. Select tracks from candidate
   After tracking is done for both of along-z and along-xy, the tracks are selected from candidates. Firstly, the candidates is selected according to the angle with z-axis. For the candidates reconstructed from along-z is restricted to less than 60 degrees and for the candidates reconstructed from along-xy is restricted to more than 60 degrees. The candidates is ranked according to the

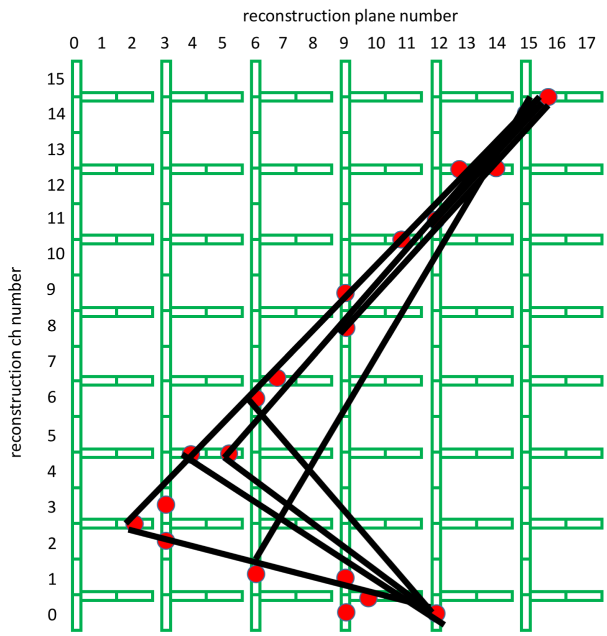

Figure A.4: The candidate of track.

number of hits in candidates, length, sum of p.e. and sum of square error. The lower ranked candidate is compared with higher candidates and if it includes more than half hits which is also included in higher candidates, it is rejected in candidates. And then some candidates are selected as reconstructed two-dimensional track as shown in Fig. A.6.

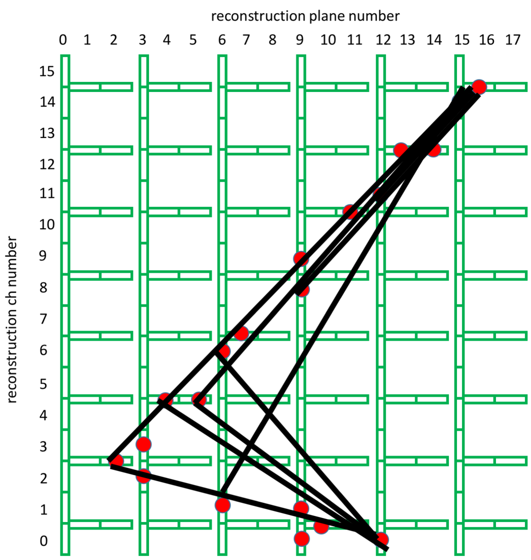

Figure A.5: The candidate of track.

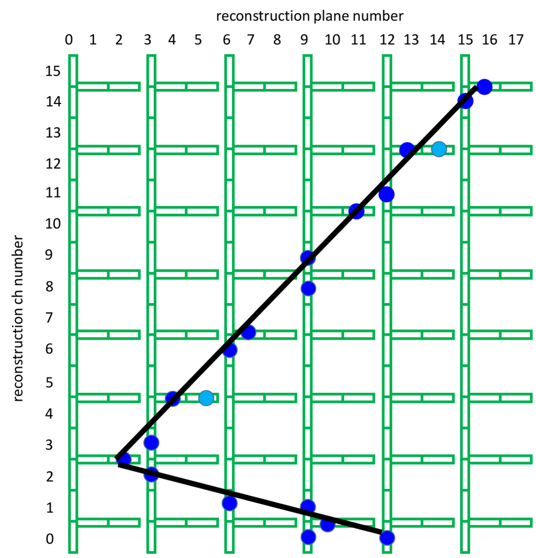

Figure A.6: Tracks after pick up near hits. Light blue circle is the hits picked up.

List of Tables

List of Figures

Bibliography

[1] Y. Fukuda et al. (Super-Kamiokande Collaboration), Phys. Rev. Lett. 81, 1562 (1998).

[2] Z. Maki, M. Nakagawa and S. Sakata, Prog. Theor. Phys. 28, 870 (1962) .

[3] K.A. Olive et al. (PDG), Chin. Phys. C38, 090001 (2014).

[4] Yoshinari Hayato, Seminar of neutrino interaction with nucleus and their simulation, http://www-he.scphys.kyoto-u.ac.jp/nufrontier/files/hayato- 20140111.pdf

[5] K.Abe *et al.* (T2K collaboration), Phys. Rev. D, 96, 092006 (2017).

[6] C. Patrignani et al. (Particle Data Group), Chin. Phys. C, 40, 100001 (2016) and 2017 update.

[7] I. Esteban et al., JHEP 1701, 087 (2017).

[8] K. Abe et al. (T2K Collaboration), Nucl. Instrum. Meth. A 659, 106 (2011).

[9] J-PARC TDR, KEK-Report 2002-13 and JAERI-Tech 2003-044, http://hadron.kek.jp/ accelerator/TDA/tdr2003/index2.html (2003).

[10] K. Abe et al. (T2K Collaboration), Phys. Rev. D 88, no. 3, 032002 (2013).

[11] Y. Fukuda et al. (Super-Kamiokande Collaboration), Nucl. Instrum. Meth. A 501, 418 (2003).

[12] S. Nakayama et al. (K2K Collaboration), Phys. Lett. B619, 255 (2005).

[13] K. Abe et al. (T2K Collaboration), Phys. Rev. D 95, 012010 (2017).

[14] K. Abe et al. (T2K Collaboration), Phys. Rev. D 97, 012001 (2018).

[15] Y. Hayato, Nucl. Phys. Proc. Supp. B112, 171 (2002).

[16] C. Andreopoulos et al., Nucl. Instrum. Methods A614, 87 (2010).

[17] K. Abe et al. (T2K Collaboration), Phys. Rev. D 93, 112012 (2016).

[18] K. Abe et al. (T2K Collaboration), Phys. Rev. D 87, 092003 (2013)

[19] WAGASCI Collaboration, Proposal to 25th J-PARC PAC(P69) (2017).

[20] K.Abe *et al.* (T2K collaboration), Phys. Rev. D, 90, 052010 (2014).

[21] K. Abe et al. (T2K Collaboration), Nucl. Instrum. Meth. A 567, 622 (2010).

[22] M. Yokoyama et al. , Nucl. Instrum. Meth. A 694, 211-223 (2012).

[23] Omega, SPIROC 2 User Guide (2009).

[24] F. Gastaldi, R. Cornat, F. Magniette, and V. Boudry, A scalable gigabit data acquisition system for calorimeters for linear collider, in proceedings of TIPP2014, PoS 193 (2014).

[25] M.Antonova *et al.*, Baby MIND Experiment Construction Status, arXiv:1704.08917, NUPHYS2016-PARSA, FERMILAB-CONF-17-205-APC (2016).

[26] F.Hosomi , Characterization of Multi-Pixel Photon Counters for a new neutrino detector, Mather's thesis, the University of Tokyo (2016).

[27] N.Ishizima and Y.Nakai, EASIROC MODULE User Guide, ver. 1.0 (2014).

[28] Texas Instruments, CDCLVC11xx data sheet, http://www.ti.com/lit/ds/symlink/cdclvc1104.pdf

[29] N.Chikuma, Research and development of magnetized muon range detector and readout electronics for a neutrino cross section experiment, Mather's thesis, the University of Tokyo (2016)

[30] N. S. Moreau (OMEGA microelectronics group), CMS GRPC meeting, ROC chips (2012)

[31] T.Koga, Research and development of a new neutrino detector for precise measurement of neutrino-nucleus cross sections, Mather's thesis, the University of Tokyo (2014)

[32] T. Suzuki and D.F. Measday, Phys. Rev. C 35, 6 (1987)